Extension of a PFEM compressible flow solver for droplet spreading phenomena

Auteur : Scheir, Tom
Promoteur(s) : Ponthot, Jean-Philippe
Faculté : Faculté des Sciences appliquées
Diplôme : Master en ingénieur civil physicien, à finalité approfondie
Année académique : 2023-2024
URI/URL : http://hdl.handle.net/2268.2/20890

University of Liège - School of Engineering and Computer Science

Extension of a PFEM compressible flow solver for droplet spreading phenomena

Master's thesis completed in order to obtain the degree of Master of Science in Civil Engineering Physics, by **Scheir Tom**

Supervisors
Pr. Jean-Philippe Ponthot
Pr. Tristan Gilet

Jury member
Simon Février

Jury president
Pr. Benoît Vanderheyden

Academic year 2023-2024

Abstract

THIS WORK FOCUSES ON THE EXTENSION of an already existing particle finite element method (PFEM) solver : `PFEM3D`. The goal is to extend its reach of applicability in order to model liquid-substrate phenomena, such as the capillary effect, the formation of a contact angle at the contact line, and dissipation due to friction at the liquid-substrate contact, which are predominant effects at small-scale fluid dynamics problems. For this purpose, the PFEM implementation of `PFEM3D` is compared with a state of the art model : the lacking contributions are identified and added to the computer model. A set of verification tests is then performed to verify if the obtained results are comparable to those provided by the reference source. After extensive validation of the numerical model, a simple implementation for contact angle hysteresis is suggested.

Remerciements

J'aimerais exprimer ma sincère gratitude envers toutes les personnes qui m'ont accompagné durant la réalisation de ce travail.

Dans un premier temps, j'aimerais remercier le Pr. Jean-Philippe Ponthot, ainsi que le Pr. Tristan Gilet, de m'avoir donné l'opportunité de pouvoir travailler sur un sujet qui m'a énormément intéressé du début jusque la fin. Leur soutien, ainsi que leur disponibilité, ont été des facteurs qui se sont avérés très importants dans la réalisation de ce travail, et je leur en suis extrêmement reconnaissant.

J'aimerais aussi remercier Simon Février et Martin Lacroix, qui se sont toujours mis à ma disponibilité pour répondre à mes questions et pour m'aiguiller dans la bonne direction quant à l'évolution de ce travail. Nos discussions sur le sujet ont été d'une aide inimaginable et je ne serais jamais parvenu à realiser ce travail sans leur implication.

Daarna wil ik mijn ouders uit de grond van mijn hart bedanken dat ze me de kans hebben gegeven om te studeren, ondanks mijn niet altijd gemakkelijke pad. Hun onvoorwaardelijke steun is essentieel geweest voor de voortgang van dit werk, maar ook meer in het algemeen tijdens mijn hele carrière als student. Zonder hen was ik nooit zover gekomen. Naast mijn ouders wil ik ook graag mijn broers en zus noemen : Maarten, Ruben en Anouk, die zonder het zelf te beseffen, een enorme zijn geweest.

J'aimerais finalement mentionner quelques autres personnes, parmi lesquelles Damien, Zakaria et William, avec qui un vrai esprit d'équipe s'est installé durant mes années de Master en particulier. D'autres personnes qui ont été un soutien inimaginable durant ce parcours universitaire sont Stéphane, William, Loïs, Niels, Dorian et Morgane.

Contents

I Introduction **8**

1 Structure of the work **10**

2 An overview of the PFEM **10**

II 2D oscillating water droplet in zero-gravity **14**

1 Introduction : problem description **14**

2 Governing equations and analytical solutions in the framework of linear theory **16**
2.1 Governing equations . . . 16
2.2 Analytical solutions in the framework of linear theory . . . 17
2.2.1 Drop shape description . . . 17
2.2.2 Inner flow modelling and energy balance . . . 18
2.2.3 Extension to energy dissipation due to viscous forces in the liquid bulk . . . 19

3 Initial deviation « not too far off » the equilibrium configuration : $\partial\Omega_0 \simeq \partial\Omega_{\mathbf{eq}}$ **20**
3.1 Implementation of the initial geometry . . . 20
3.2 Choice of the simulation parameters . . . 21
3.2.1 Characteristic mesh size h . . . 21
3.2.2 Other simulation parameters . . . 22
3.3 Results and comparison with theoretical predictions . . . 23
3.3.1 Theory applied to the framework of the current study . . . 23
3.3.2 Comparison with the numerical results . . . 24
3.4 Influence of the numerical parameters on the quality of the simulation results 26
3.4.1 Characteristic element size . . . 26
3.4.2 Time-step . . . 28
3.4.3 What if $h(d)$ is reduced further ? . . . 30
3.5 Results and comparison with theoretical predictions for « optimal » simulation parameters . . . 32
3.6 Conclusion on the case study $\partial\Omega_0 \simeq \partial\Omega_{\text{eq}}$ . . . 32

4 $\partial\Omega_0 \simeq \partial\Omega_{\mathbf{eq}}$ with an even smaller initial deformation **33**
4.1 Results and comparison with theoretical predictions . . . 34

5 Testing of the theoretical model on a large initial deviation from equilibrium **36**
5.1 Implementation of the initial geometry and numerical parameters . . . 36
5.2 Results and comparison with theoretical predictions . . . 37
5.2.1 Correction of the theoretical model to higher-order oscillation modes 38

6 Conclusion **40**

III Extension of PFEM3D : modelling of droplet oscillations on a substrate **41**

1 Introduction : problem description **41**

2 Governing equations and an overview of the FE implementation of PFEM3D **42**
2.1 Governing equations 42
2.2 An overview of the FE implementation of PFEM3D 44

3 The surface forces term **45**
3.1 Which contributions are lacking to the surface forces term $\mathbf{F}_{\text{ext}}^{\partial\Omega}$? 47

4 Adding the lacking forces to the FE formulation **48**
4.1 Horizontal free slip BC at Γ'_{FS} and the surface tension force at $\partial\Gamma$ 48
4.2 Dissipation due to friction at Γ'_{FS} 49
4.3 More forces at the contact line $\partial\Gamma$ 51
4.4 Summary 52

5 Validation of the numerical model **53**
5.1 Implementation of the initial geometry 53
5.2 Numerical parameters 54
5.3 Validation of the numerical model 55
5.3.1 Mesh study 56
5.3.2 Influence of the dissipative contribution at $\Gamma'_{\text{FS}} \equiv \Gamma_{\text{FS}} \cup \partial\Gamma$ 59
5.3.3 Influence of the capillary effect and the normal stress component at $\partial\Gamma$ 68

6 Conclusion **71**

IV Further extension of PFEM3D : modelling contact angle hysteresis **73**

1 The physics of contact angle hysteresis **74**

2 Implementation of contact angle hysteresis in the numerical model **76**

3 Initial test **78**
3.1 Problem suggestion 78
3.2 Choice of the initial geometry 79
3.3 Choice of the numerical parameters 79
3.4 Initial results 80
3.5 Discussion 80

4 Droplet on an inclined plane **82**

5 Conclusion **85**

V Conclusion and prospects for future work **88**

Appendices **90**

Bibliography **97**

Notations

- [s] : refers to the units of a physical quantity (in this case, seconds, which is the measure of time) ;
- $\sim$: expresses that some quantity is of the same order of magnitude as another quantity ;
- $\nabla \times \mathbf{v}$: denotes the rotational of a vector field (in this case, the rotational of the velocity profile) ;
- $\mathbf{v}$: denotes a vector quantity (in this case, the velocity profile) ;
- $\nabla \cdot \boldsymbol{\sigma}$: denotes the divergence of a second-order tensor (in this case, the divergence of the Cauchy stress tensor $\boldsymbol{\sigma}$) ;
- $\boldsymbol{\sigma}$: denotes a second-order tensor (in this case, the Cauchy stress tensor) ;
- $\nabla \mathbf{v}$: denotes the gradient of a vector field (in this case, the gradient of the velocity profile) ;
- $(\nabla \mathbf{v})^{\mathrm{T}}$: denotes the transpose of a vector field (in this case, the transpose of the gradient of the velocity profile) ;
- $\simeq$: denotes that a quantity can be approximated as another quantity ;
- $\dot{\varepsilon}_n$: denotes the time-derivative of a quantity (here, the time-derivative of the droplet free surface oscillations) ;
- $||\varphi||$: denotes the norm of a physical quantity (in this case, the norm of the velocity potential) ;
- $\nabla \varphi \cdot \mathbf{n}$: denotes the dot product between two vectors or between a vector field and a vector (in this case, the dot product of the gradient of the velocity potential and the outward normal vector to the droplet free surface) ;
- $\nabla^2 \varphi$: denotes the Laplacian of a quantity (here, the Laplacian of the velocity potential) ;
- $\ddot{\varepsilon}_n$: the second-order time-derivative of a quantity (in this case, the second-order time-derivative of the droplet free surface oscillations) ;
- $\boldsymbol{D} : \boldsymbol{D}$: denotes the double contraction product between two second-order tensor (in this case, between the strain-rate tensor and itself).

Part I
Introduction

A branch of the medical domain that has been submitted to drastic developments in recent years is the integration of so-called *lab-on-chips*. Lab-on-chips are diagnostic devices that allow for *e.g.* quick identification of the onset of diseases at early stages [1]. These devices incorporate so-called *microchannels*, through which fluids are allowed to flow, and the basic functioning principle is comparable to that of microprocessors (using the flow of charge carriers) [2]. A major advantage of these devices is their *point-of-need* diagnostics feature, which allows for testing (blood samples for example) out of reference labs. In other words, they provide a *personal* and *rapid* mean of delivering crucial information on the health of a patient.

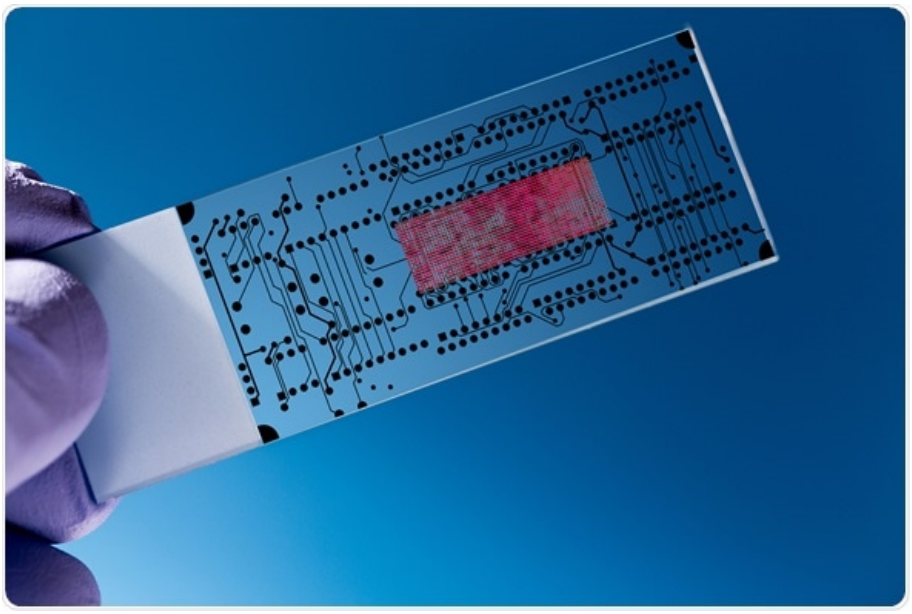

Figure I.1: Lab-on-a-chip (image source : `https://www.azolifesciences.com/article/What-is-Lab-on-a-Chip.aspx`).

A prominent example for the application of such devices is related to the *dosage* of a drug for a patient [2]. Indeed, conventional medication that can be purchased in pharmacies have pre-determined dosages of a drug for the treatment of a given medical condition. However, optimal dosages might vary from patient to patient, depending on their weight, their age, and other parameters that are submitted to constant variations such as oxygen saturation in the blood, red blood cell concentration, *et cætera*. In contrast, the capability of lab-on-chips to measure such influencing parameters regularly over time provide means for *personalized* dosage concentrations, improving the overall effectiveness of the prescribed drug.

For this reason, the global lab-on-chip market is evaluated to an over-7 billion United States Dollars (USD) value, and is expected to hit the 14 billion USD mark by the year 2032 [3].

The fabrication of these devices is, at the moment, mostly lab-focused, in the sense that each prototype is fabricated from scratch and tested for a specific purpose. This process consists in a series of complex steps that sometimes take quite some time to be completed [2]. In Fig. I.2 [2], these steps are summarized.

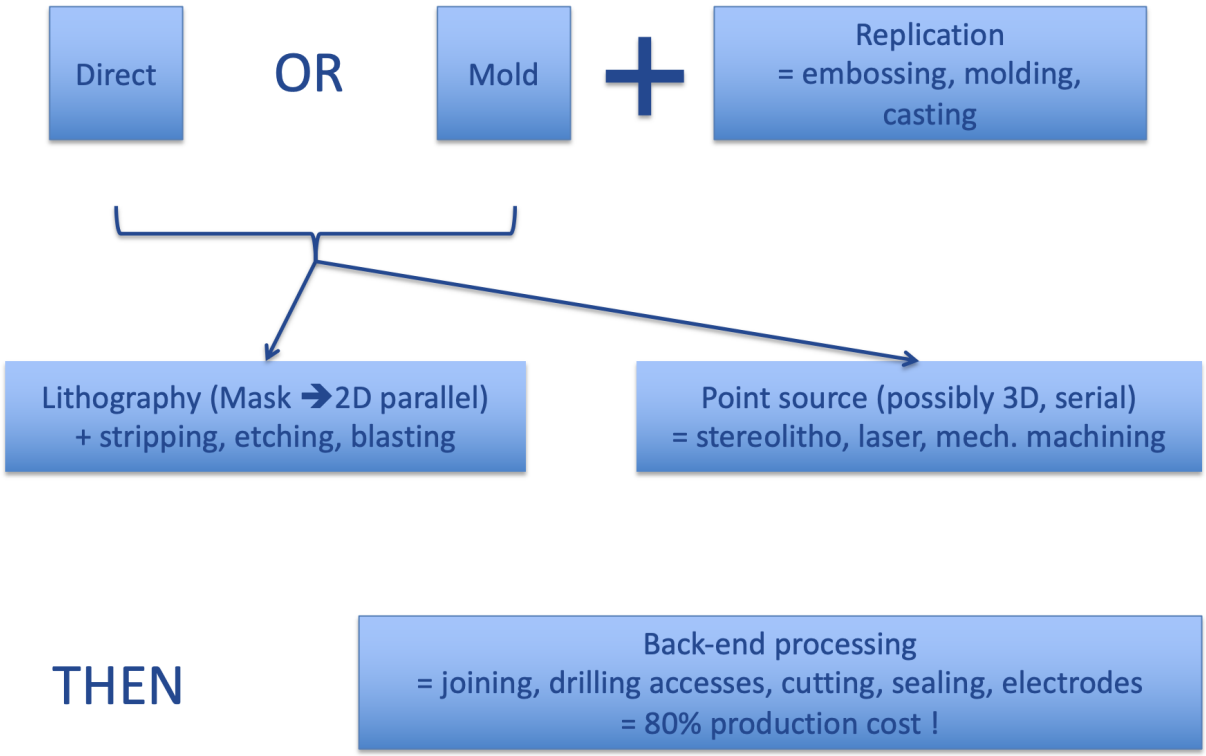

Figure I.2: Summary of the fabrication process of a lab-on-chip device (this figure is directly taken from [2]).

In the seek of the optimal microchannel configuration for a given application, significant amounts of lab-on-chips are produced and tested, which is time consuming and costly. For this reason, it might be interesting to involve *numerical models* in their development. Indeed, instead of fabricating a new chip for each slight modification that has to be applied to an initial lab-on-chip prototype, *e.g.* a change in the geometry of the microchannels, changing the geometry of the lab-on-chip configuration that is inputted in an *ad hoc* numerical model would lead to immediate results that cost no money in terms of fabrication.

A promising numerical model that is ideal for such applications, notably fluid flow and fluid free-surface tracking over time, is the *particle finite element method* (PFEM). This specific finite element method (FEM) is based on the Lagrangian description of the fluid particles and thus free surface tracking over time is inherent to the nature of the method. A PFEM computer code, called `PFEM3D` [4], is currently in development at the University of Liège in the research unit of Pr. J.-P. Ponthot, LTAS-A&M. However, this computer code does not account for important liquid-substrate contact phenomena which are predominant at millimeter and sub-millimeter-scales, such as the modelling of *contact angles*, the *surface tension force at the contact line*, and so forth. For this reason, the focus

of this work is to provide an *extension* for PFEM3D, taking account of these phenomena. The general framework of the work is centered around the study of *droplet spreading in 2D*, because the literature provides extensive research on this topic, as well as an ideal starting point for the more general problem discussed hereabove.

1 Structure of the work

In a first instance, an overview of the particle finite element method is given. The main concepts are presented and will allow for a sufficient understanding of the method in order to follow the work.

Then, the PFEM3D solver will be applied to a theoretical case study regarding the 2D oscillations in zero-gravity of a water droplet (Part II). For this study, the work of Aalilija *et al.* [6] on the 2D Rayleigh model is considered. First, the theoretical model is presented. Then, a case study is suggested for the validation of the numerical model, without the implementation of any additional forces (these will be implemented in later stages of this work, *cf.* Part III). The physical model is then simulated using PFEM3D and compared to the theoretical predictions from [6]. This study constitutes a first application of the PFEM3D computer code to millimeter-scale fluid dynamics.

In Part III, the lacking forces are implemented in the PFEM3D computer model, namely the surface tension force at the contact line, the dissipation at the liquid-substrate contact, the force resulting from the capillary effect as well as from the normal stress jump, both at the contact line. In a first instance, an overview of the implementation of this model is provided in order to efficiently identify the lacking forces taking account of liquid-substrate interaction phenomena, *e.g.* friction at the liquid-substrate contact. The method for identifying these contributions is by using the works of Jarauta *et al.* [10] and Mahrous *et al.* [9]. After identification of these lacking force terms, they are implemented in the PFEM3D solver and their effect is studied on the droplet spreading behaviour. The data obtained from PFEM3D is then compared to the work of Mahrous *et al.* [9] and the validity of the model is assessed.

In the final part of this work (Part IV), a simple model for *contact angle hysteresis* (yet another important phenomenon at the liquid-substrate contact for millimeter-scale fluid dynamics applications) is suggested. This model is based on theoretical observations that will be described Part IV as well as on the work of Jarauta *et al.* [10]. Some case studies are suggested and the behaviour modelled by PFEM3D is discussed qualitatively.

In Part V, the conclusions of this work are presented and prospect for future advancements on the topic are suggested.

2 An overview of the PFEM

For the purpose of this work, the particle finite element method (PFEM) is used. The reason for this choice is that the evolution of the fluid free surface is automatically tracked

over time due to the inherent Lagrangian nature of the model. The specific PFEM code that is considered is `PFEM3D` [4], initially developed by S. Février.

The key concept of the PFEM is to describe the motion of a physical volume Ω in a Lagrangian manner. For this purpose, the first step for the PFEM is to fill Ω with a set of so-called *particles*, which act as the *nodes* for the finite element mesh. This is represented in Fig. I.3.

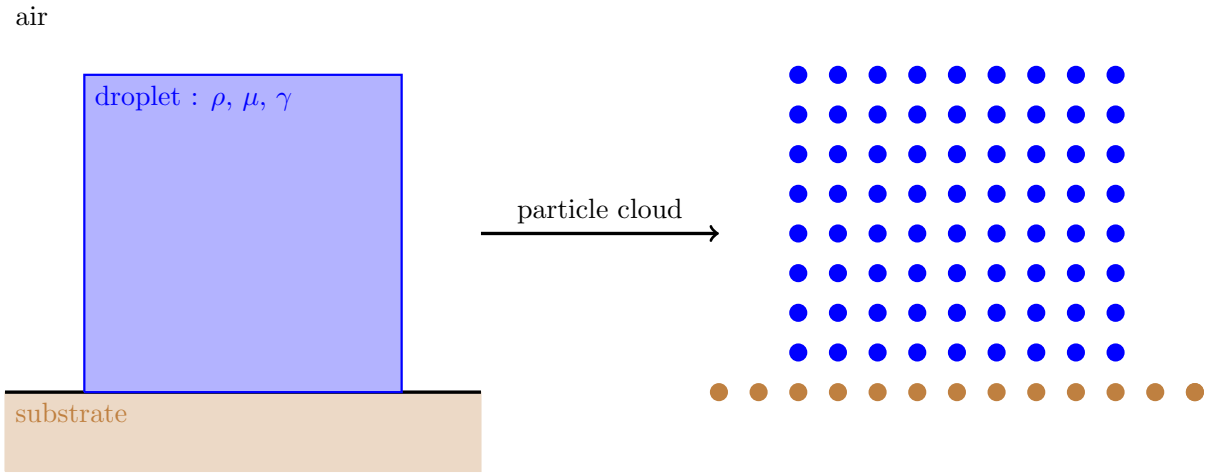

Figure I.3: First step of the PFEM : the physical domain is filled with a set of particles. The figure represents a water droplet that is initially square-shaped deposited on a substrate. The physical properties of this droplet are denotes ρ [kg/m^3] (density), μ [Pa $\cdot$ s] (viscosity) and γ [N/m] (surface tension).

A finite element mesh is then generated using a *Delaunay triangulation* [5], which ensures node connectivity. This is represented in Fig. I.4. As can be observed in this figure, there is no clear separation between the *actual* physical volume Ω and the generated finite element mesh at this stage. Indeed, nodes from the fluid volume are connected to nodes from the substrate that should in no way be associated to one another. From a physical point of view, this generates an *excess mass* as well as a misrepresentation of the physical volume Ω. To remedy this problem, the idea is to define a *geometrical* criterion that uses the fact that these non physical elements are usually the largest and the most distorted ones (these elements are represented by red triangles in Fig. I.4). A *characteristic element size* h_{mean} is defined as well as an *index of elemental distortion* α_e such that [5] :

$$\alpha_e = \frac{R_e}{h_{\text{mean}}}, \tag{I.1}$$

where R_e is the element circumcircle. Then the elements for which the following condition is satisfied :

$$\alpha_e \leq \bar{\alpha}, \tag{I.2}$$

where $\bar{\alpha}$ is the *threshold value of the distortion of the mesh*, are kept, while the others are removed from the mesh. This is referred to as the *α-shape method* and is represented in Fig. I.5. The literature suggests that $\bar{\alpha} = 1.2$ [-] is the optimal value.

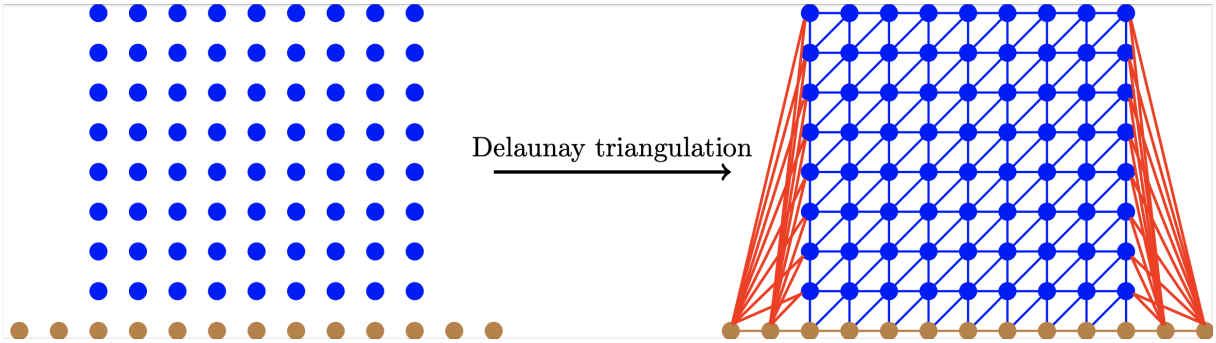

Figure I.4: Second step of the PFEM : guarantee node connectivity by performing a Delaunay triangulation (this generated elements). The blue elements represent the correctly defined elements, while the red lines represent the incorrectly defined elements.

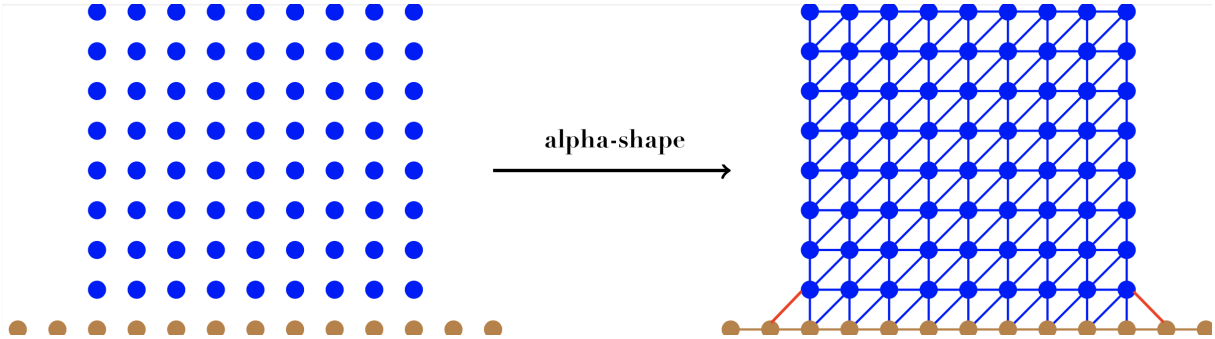

Figure I.5: Third step of the PFEM : remove the nodes from the mesh which do not satisfy the condition Eq. I.2.

The remaining parasite elements have the same characteristic element size as the ones from the *real* physical volume, and are thus kept in the finite element mesh. This still results in an error on the measurement of the physical volume mass over time, but can be minimized when h_{mean} is decreased. Once the physical volume and boundaries are recovered, the Lagrangian form of the governing equations (in the framework of this work, these are the *Navier-Stokes equations*) is solved using a standard finite element approach, for which a reminder is given in Part III. The position of the nodes are then updated in accordance with the obtained solution and then it's start from square one again. More specifically, if there is a need for re-meshing of the physical volume, *e.g.* if the elements are too distorted, the first step is performed again (filling the physical volume with a set of nodes, Delaunay triangulation...). If there is no need for re-meshing, the Lagrangian form of the governing equations is solved back again.

A key difference between the PFEM and other classical FEMs is that the physical unknowns of the problem (in the context of this work, velocity and pressure) are stored at the *nodes* rather than at the *Gauss points*. This constitutes the core of the Lagrangian nature of the method, because once the Lagrangian form of the governing equations are solved, the position of the *nodes*, also called *particles* in the PFEM, are directly updated. This interesting approach allows for the free surface of the fluid to be tracked naturally over time.

To conclude this introductory part of the work, the steps of the PFEM are summarized below :

- The computational domain is filled with a set of *particles* ;
- The finite element mesh is generated by a *Delaunay triangulation*, which assures mesh connectivity :
- The physical volume and boundaries are recovered by the α-shape method ;
- The Lagrangian form of the governing equations is solved using a classical FEM approach :
- The position of the nodes is updated ;
- If necessary, re-meshing is performed. If not, the Lagrangian form of the governing equations is solved for the next time-step.

Part II
2D oscillating water droplet in zero-gravity

In this part of the work, a study is performed on the capabilities of the `PFEM3D` computer code. The additional terms necessary for the modelling of the final problem described previously (*cf.* Part I) are not yet considered. The chosen problem for this study is the *2D oscillating water droplet in zero-gravity* and refers to the *2D Rayleigh theory* [6]. This theory provides a full set of equations allowing for precise tracking of the free surface of the oscillating water droplet in zero-gravity over time and is hence ideal for comparing numerical data to.

In a first instance, a description of the problem is performed and will allow for a basic understanding of the involved physics, namely the *Laplace law*. Afterwards, the full set of governing equations is presented and applied to the problem under study ; that is the evolution of the free surface (of the oscillating water droplet) over time will be derived from the Navier-Stokes equations. Then, the choice of the geometry of the water droplet is presented and its implementation in the computer code is fully described by a set of geometrical parameters. Next, the full set of numerical parameters is given (namely the characteristic mesh size, the time-step, the simulation time, and so forth) and the simulation results are displayed, compared with theoretical predictions and discussed. Other geometries are then implemented in order to study up to which point the 2D Rayleigh theory is valid and up to which point the simulation results are in agreement with the former. Finally, the main conclusions are presented.

1 Introduction : problem description

A representation of the studied problem is provided in Fig. II.1. Initially, at time $t = 0$ [s], the water droplet is described by its free surface $\partial\Omega_0 \equiv \partial\Omega(t = 0)$ and is such that it is deviated from its equilibrium configuration $\partial\Omega_{\text{eq}}$. In 2D, the equilibrium configuration of a water droplet that is not subjected to any body forces (in particular : gravity) and that is not deposited on some surface is a circle. This is due to the tendency of surface tension to minimize surface energy, and more precisely the *Gibbs free energy* of the system. This is expressed by the *Laplace law*, which is expressed as follows[1] in 2D :

$$\Delta p \sim \frac{\gamma}{\mathcal{R}}, \tag{II.1}$$

where Δp [Pa] is the pressure differential at the liquid/air interface, γ [N/m] is the surface tension coefficient and $\mathcal{R}$ [m] is the radius of curvature at the liquid/air interface. The aforementioned oscillations are the result of this initial deviation from its equilibrium

[1] Note that another valid expression would be, given the problem representation in Fig. II.1 : $\Delta p(\theta) \sim \gamma/\mathcal{R}(\theta)$, which is such that it states explicitly that the pressure differential is calculated at each point of the free surface as a function of the arbitrary angle θ [rad].

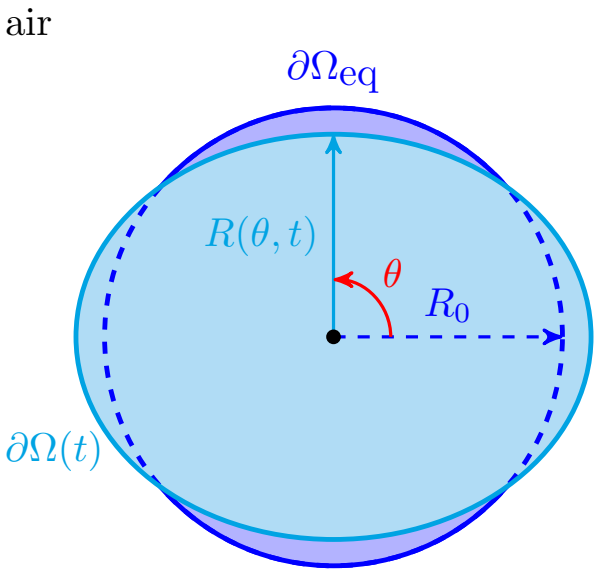

Figure II.1: Schematic of a water droplet in zero-gravity. The *perturbed configuration*, denoted $\partial\Omega(t)$, refers to the description of the free surface of the water droplet that oscillates over time, while the *equilibrium configuration*, denoted $\partial\Omega_{\text{eq}}$, describes the free surface of the water droplet once its free surface no longer oscillates.

configuration ; the motor of these oscillations is *surface tension*[2].

Initially, an irrotational flow was assumed by Rayleigh ($\nabla \times \mathbf{v} = \mathbf{0}$, where $\mathbf{v}$ [m/s] is the velocity profile at any point of the fluid body) to derive the frequency spectrum of *small amplitude* axi-symmetrical oscillations of *non-viscous* drops in a vacuum with zero-gravity. Afterwards, it was shown by Lamb [7] that for *weakly viscous* liquids immersed in an inviscid medium, the frequency spectrum is identical to that found by Rayleigh and the assumption of the irrotational flow can be used to determine the damping rate. Prosperetti [8] then later showed that the general solution for the limiting case of low velocities behaves as a damped harmonic oscillator.

In the next sections, the methodology for obtaining the evolution of the free surface oscillations $\partial\Omega(t)$ follows the work of Aalilija *et al.* [6]. In a first instance, the governing equations are presented, namely the Navier-Stokes equations. From there, a geometrical description of the free surface over time is established. Then, inner flow modelling and energy balance will yield ordinary differential equations (ODEs) , describing the evolution of the free surface over time.

[2]Indeed, surface tension can either be interpreted as a force per unit length, or as an energy per unit surface.

2 Governing equations and analytical solutions in the framework of linear theory

2.1 Governing equations

The governing equations of free-oscillating viscous droplets are established as follows. The motion of a Newtonian incompressible liquid of constant density ρ [kg/m^3] and viscosity μ [Pa $\cdot$ s] is considered. The time-dependent boundary of the oscillating droplet is denoted $\partial\Omega(t)$. An isothermal regime with no phase transformation is also assumed. Neglecting all body forces (and in particular gravity $\mathbf{g}$ [m/s^2]), the governing Navier-Stokes equations are, considering a Lagrangian framework[3] :

$$\begin{cases} \rho \dfrac{\mathrm{d}\mathbf{v}}{\mathrm{d}t} - \nabla \cdot \boldsymbol{\sigma} = \mathbf{0} \, ; \\ \nabla \cdot \mathbf{v} = 0, \end{cases} \tag{II.2}$$

where $\mathbf{v}$ is the liquid velocity vector and $\boldsymbol{\sigma}$ [Pa] is the liquid stress tensor given by the incompressible Newtonian constitutive law :

$$\boldsymbol{\sigma} = 2\mu \boldsymbol{D} - p\boldsymbol{I}, \tag{II.3}$$

$\boldsymbol{D}$ [s^{-1}] being the strain-rate tensor expressed as $\boldsymbol{D} = (1/2)(\nabla\mathbf{v} + (\nabla\mathbf{v})^{\mathrm{T}})$, p [Pa] the pressure field in the liquid and $\boldsymbol{I}$ [-] the identity tensor. At $t = 0$ [s], the initial shape of the liquid is assumed to be known, as well as its velocity field, such that :

$$\begin{cases} \partial\Omega(t=0) = \partial\Omega_0 \, ; \\ \mathbf{v}(\mathbf{x}, t=0) = \mathbf{v}_0(\mathbf{x}) \, ; \\ \nabla \cdot \mathbf{v} = 0, \end{cases} \tag{II.4}$$

where $\mathbf{v}_0(\mathbf{x})$ [m/s] is an initial velocity field and $\mathbf{x}$ [m] denotes the spatial coordinates. Given no mass exchange occurs through $\partial\Omega(t)$, the local mass flux leaving the liquid domain $\rho(\mathbf{v} \cdot \mathbf{n} - v_{\partial\Omega(t)})$ is zero, where $\mathbf{n}$ [-] is the unit outward normal to $\partial\Omega(t)$ and $v_{\partial\Omega(t)}$ [m/s] is its normal velocity (of the liquid free surface). These considerations lead to writing the so-called *kinematic interface condition* as :

$$\mathbf{v} \cdot \mathbf{n} = v_{\partial\Omega(t)}. \tag{II.5}$$

The second interface condition, referred to as the *dynamic condition*, arises from the normal component of the force balance at the interface $\partial\Omega(t)$:

$$\boldsymbol{\sigma} \cdot \mathbf{n} = -\gamma\kappa\mathbf{n} - p_{\mathrm{ext}}\mathbf{n}, \tag{II.6}$$

where κ [m^{-1}] is the curvature at $\partial\Omega(t)$ and p_{ext} is the pressure of the surrounding gas phase. For the tangential component, given no surface tension gradients are considered and in the context of inviscid fluids, the condition is automatically satisfied.

[3] The Navier-Stokes equations are written in a Lagrangian framework because of the inherent Lagrangian nature of the PFEM.

2.2 Analytical solutions in the framework of linear theory

2.2.1 Drop shape description

As mentioned beforehand, in order to obtain an analytical solution for the problem, a correct description of the droplet free surface $\partial\Omega(t)$ over time is required. The usage of the cylindrical coordinate system is considered. The radius of $\partial\Omega(t)$ at each section of an initially-shaped ellipse[4], not too far from its equilibrium configuration, can be expressed as the sum of a constant part (the equilibrium radius R_0 [m]) and a spatial-temporal variable part $f(\theta, t)$ [m] as follows :

$$R(\theta, t) = R_0 + f(\theta, t). \tag{II.7}$$

In the current framework, *small amplitude variations* are considered. It is assumed that $f(\theta, t)$ can be written as a linear combination of *decoupled* modes denoted by the integer n as follows (because the domain of θ is finite) :

$$f(\theta, t) = \sum_{n\geq 0} \alpha_n(t) \cos(n\theta), \tag{II.8}$$

where $\alpha_n(t)/R_0 \ll 1$ given small amplitude variations are studied. Mode $n = 0$ is related to the volume oscillation. Mode $n = 1$ describes the translational oscillations of the center of mass (which is considered to be fixed such that $\alpha_1(t) = 0$). Modes $n \geq 2$ describe the shape oscillations around equilibrium. Following these considerations, the geometrical description of the radius of the free surface at any point θ and any time t now reads :

$$R(\theta, t) = \underbrace{R_0 + \alpha_0(t)}_{\equiv b_0(t)} + \sum_{n\geq 2} \alpha_n(t) \cos(n\theta) \equiv b_0(t) + \sum_{n\geq 2} \alpha_n(t) \cos(n\theta). \tag{II.9}$$

Given incompressible flow is considered, the volume of the oscillating droplet is equal to that at equilibrium and it can be shown that :

$$b_0 = R_0 \sqrt{1 - \frac{1}{2} \sum_{n\geq 2} \left(\frac{\alpha_n}{R_0}\right)^2} \simeq R_0 \left[1 - \frac{1}{4} \sum_{n\geq 2} \left(\frac{\alpha_n}{R_0}\right)^2\right], \tag{II.10}$$

such that :

$$R(\theta, t) \simeq R_0 \left[1 - \frac{1}{4} \sum_{n\geq 2} \varepsilon_n^2 + \sum_{n\geq 2} \varepsilon_n \cos(n\theta)\right], \tag{II.11}$$

where ε_n is defined as $\varepsilon_n = \alpha_n/R_0$ and defines the quantity describing the droplet free surface oscillations (the amplitude of the oscillations of the free surface of the water droplet with respect to its equilibrium configuration). From there, the purpose is to find the governing equation for the evolution of ε_n.

[4]The initial shape of the droplet free surface is not required to be an ellipse per default. Any initial shape, as long as it is not too far from equilibrium, would work just fine. The fact that an ellipse-shaped droplet is considered is a choice from the author that relies on the ease of its implementation for later stages of this work.

2.2.2 Inner flow modelling and energy balance

As aforementioned, the goal is to obtain an expression for ε_n over time in order to describe the amplitude variations of the free surface $\partial\Omega(t)$ of the water droplet. It is considered that the fluid motion can be approximated by an irrotational flow[5], such that the velocity field derives from a scalar potential $\mathbf{v} = \nabla\varphi$. The velocity potential φ of the n-th mode can be formulated as :

$$\varphi(r, \theta, t) = \beta_n(t) r^n \cos(n\theta), \tag{II.12}$$

where β_n is obtained from the kinematic boundary condition Eq. II.5 at the free surface :

$$v_r(r = R) = \left.\frac{\partial\varphi}{\partial r}\right|_{r=R} = \frac{\partial R}{\partial t}, \tag{II.13}$$

which leads to the approximation $n\beta_n R_0^{n-2} \simeq \dot{\varepsilon}_n$ (Appendix 1). Hence, the velocity potential flow can be expressed as, for any mode n :

$$\varphi(r, \theta, t) = \frac{1}{n} R_0^2 \left(\frac{r}{R_0}\right)^n \cos(n\theta)\dot{\varepsilon}_n(t). \tag{II.14}$$

The kinetic energy of the droplet is computed as :

$$E_{\text{kin}} = \int_{\Omega(t)} \frac{1}{2}\rho ||\nabla\varphi||^2 \, \mathrm{d}\Omega(t) = \int_{\partial\Omega(t)} \frac{1}{2}\rho\varphi\nabla\varphi \cdot \mathbf{n} \, \mathrm{d}\partial\Omega(t) - \int_{\Omega(t)} \frac{1}{2}\rho\varphi\nabla^2\varphi \, \mathrm{d}\Omega(t), \tag{II.15}$$

where the second integral on the right-hand side (RHS) is equal to zero due to incompressibility (Appendix 2) such that the previous equality becomes :

$$E_{\text{kin}} = \frac{1}{2}\rho \, \delta z \int_0^{2\pi} \varphi \frac{\partial\varphi}{\partial r} R \, \mathrm{d}\theta \simeq \frac{1}{2n}\pi\rho R_0^4 \dot{\varepsilon}_n^2 \, \delta z, \tag{II.16}$$

and following the work of Rayleigh, the potential energy is expressed as :

$$E_{\text{pot}} = \gamma(S(t) - S_0), \tag{II.17}$$

i.e., the potential energy is surface energy that results from the difference in area of the free surface $S(t)$ out of equilibrium and the equilibrium surface S_0. Using some geometry, it can be shown that E_{pot} is expressed equivalently as :

$$E_{\text{pot}} \simeq \frac{1}{2}\pi(n^2 - 1)\gamma R_0 \varepsilon_n^2 \, \delta z, \tag{II.18}$$

such that the rate of total energy $E_{\text{tot}} = E_{\text{kin}} + E_{\text{pot}}$ can be written as :

$$\frac{\mathrm{d}E_{\text{tot}}}{\mathrm{d}t} = \pi \frac{1}{n}\rho R_0^4 \dot{\varepsilon}_n \left[\ddot{\varepsilon}_n + n(n^2 - 1)\frac{\gamma}{\rho R_0^3}\varepsilon_n\right] \delta z. \tag{II.19}$$

From there, considering an inviscid fluid ($\mu = 0$ [Pa · s]), the conservation of the total energy $\mathrm{d}_t E_{\text{tot}} = 0$ (Not2.15) leads to the solution of a perpetual oscillator of the form $\varepsilon_n(t) = A\cos(\omega_{n,0}t + B)$ where the angular frequency is :

[5] This result comes from the incompressibility condition.

$$\omega_{n,0} = \sqrt{n(n-1)(n+1)\frac{\gamma}{\rho R_0^3}}. \tag{II.20}$$

2.2.3 Extension to energy dissipation due to viscous forces in the liquid bulk

The rate of viscous energy dissipation is calculated along :

$$\dot{W}_{\text{vis}} = \int_{\Omega(t)} 2\mu(\boldsymbol{D} : \boldsymbol{D})\, \mathrm{d}\Omega(t) \text{ (Not2.16)}, \tag{II.21}$$

which, by following the work of Lamb [7] and using a Taylor expansion, can be approximated as :

$$\dot{W}_{\text{vis}} \simeq 4\pi\mu R_0^2(n-1)\dot{\varepsilon}_n^2\, \delta z, \tag{II.22}$$

such that the energy balance leads to the following linear second-order ODE :

$$\ddot{\varepsilon}_n + 2\lambda_n\dot{\varepsilon}_n + \omega_{n,0}^2\varepsilon_n = 0\,; \quad \lambda_n = 2n(n-1)\frac{\mu}{\rho R_0^2}. \tag{II.23}$$

If the reduced discriminant is denoted $\Delta'_n = \lambda_n^2 - \omega_{n,0}^2$, then the solution of the ODE depends on the sign Δ'_n :

- *Overdamped regime* $\Delta'_n > 0$:

$$\varepsilon_n(t) = \mathrm{e}^{-\lambda_n t}\left[\varepsilon_n(0)\cosh(\sqrt{\Delta'_n}t) + \frac{\dot{\varepsilon}_n(0) + \lambda_n\varepsilon_n(0)}{\sqrt{\Delta'_n}}\sinh(\sqrt{\Delta'_n}t)\right]\,; \tag{II.24}$$

- *Critically damped regime* $\Delta'_n = 0$:

$$\varepsilon_n(t) = \mathrm{e}^{-\lambda_n t}\left[(\dot{\varepsilon}_n(0) + \lambda_n\varepsilon_n(0))t + \varepsilon_n(0)\right]\,; \tag{II.25}$$

- *Underdamped regime* $\Delta'_n < 0$:

$$\varepsilon_n(t) = \mathrm{e}^{-\lambda_n t}\varepsilon_n^{\max}\cos(\omega_n t + \zeta_n); \quad \begin{cases} \omega_n = \sqrt{\omega_{n,0}^2 - \lambda_n^2}\,; \\ (\varepsilon_n^{\max})^2 = \varepsilon_n^2(0) + \left(\dfrac{\dot{\varepsilon}_n(0) + \lambda_n\varepsilon_n(0)}{\sqrt{-\Delta'_n}}\right)^2\,; \\ \tan\zeta_n = -\dfrac{\dot{\varepsilon}_n(0) + \lambda_n\varepsilon_n(0)}{\varepsilon_n(0)\sqrt{-\Delta'_n}}\,; \quad \cos(\zeta_n)\varepsilon_n(0) > 0. \end{cases} \tag{II.26}$$

The set of equations Eqs. II.20, II.23, II.24, II.25 and II.26 allows for a complete modelling of the evolution of the droplet free surface oscillations $\partial\Omega(t)$ in zero-gravity according to the 2D Rayleigh theory. In the following section, an initial deviation $\partial\Omega_0$ from equilibrium $\partial\Omega_{\text{eq}}$ will be suggested and implemented in `PFEM3D`. It is important to be underline that in a first instance, $\partial\Omega_0$ is *assumed* to be small enough, such that the 2D Rayleigh theory is assumed to hold. The numerical solution that will arise from this implementation will then be compared to the theoretical model described hereabove. On the hand of the obtained results, validity of the numerical model will be assessed. Depending on the answer to this question, further case studies will be presented to determine up to which point the numerical solution is correct with respect to the theoretical predictions.

3 Initial deviation « not too far off » the equilibrium configuration : $\partial\Omega_0 \simeq \partial\Omega_{\text{eq}}$

The first case study will consist of an initial droplet deformation that is « not too far » from the equilibrium configuration, by which is meant that the hypotheses for the 2D Rayleigh theory *should* apply. The goal is to show that in such a case, the `PFEM3D` computer code is able to model the droplet free surface oscillations accurately. In the following, the initial geometry of the droplet is described. Then, the choice of the physical parameters (*e.g.* the characteristic mesh size h [m], time-step Δt [s], and so forth) is presented. Afterwards, a comparison is be performed between theoretical and numerical results and it is determined if numerical convergence is reached by refining/coarsening the characteristic element size and the time-step. Finally, on the hand of these results, a study on the accuracy of the (now converged) numerical model with respect to the theoretical predictions is performed.

3.1 Implementation of the initial geometry

A schematic representation of the chosen initial geometry for the water droplet configuration is provided in Fig. II.2 in light blue, while the equilibrium configuration is represented in dark blue. The geometry parameters related to $\partial\Omega_0$ are the major ellipse axis a and the minor ellipse axis b, while only the equilibrium radius R_0 suffices to describe $\partial\Omega_{\text{eq}}$. In the following table, these parameters are provided.

Geometry parameters.

- Initial geometry/configuration : major axis $a = 1.9$ [mm], minor axis $b = 1.5$ [mm] ;
- Equilibrium geometry/configuration : equilibrium radius $R_0 = 1.688$ [mm] ;
- For both initial/equilibrium configurations : surface area $A = 8.9535$ [mm^2].

Note that only a and b are *imposed* (implemented *a priori*), while the others (R_0 and A) are a *result* from the former. For the sake of completeness, the following information is also provided in terms of deviation from equilibrium :

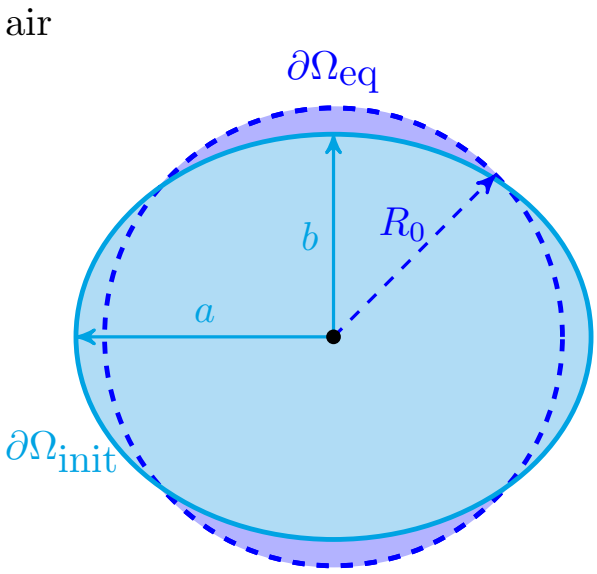

Figure II.2: Representation of the initial and equilibrium configurations of an oscillating water droplet in zero-gravity as well as the respective geometry parameters.

- The initial deviation from equilibrium along the a-axis (resp. the b-axis) is denoted Δ_a [%] (resp. Δ_b [%]) and defined as :

$$\Delta_a = \frac{|a - R_0|}{R_0} \times 100 \quad \left(\text{resp. } \Delta_b = \frac{|b - R_0|}{R_0} \times 100\right) ; \tag{II.27}$$

  and have values $\Delta_a \simeq 12.5$ [%] and $\Delta_b \simeq 11.1$ [%] ;

- From there, the *maximal deviation from equilibrium*, $\varepsilon^{\max}$, is such that $\varepsilon^{\max} = \Delta_a$, and has thus a value of $\simeq 12.5$ [%].

3.2 Choice of the simulation parameters

In a first instance, the choice of the simulation parameters is done « arbitrarily », in the sense that it is not yet known if *e.g.* the characteristic mesh size will be small enough to capture all of the physics correctly. In later stages of this work, further investigation on this matter will be performed : it is indeed essential to verify that numerical convergence is guaranteed before stating anything on the validity of the numerical model.

3.2.1 Characteristic mesh size h

Any finite element simulation requires the sectioning of the physical domain into elements formed by the finite element mesh. Hence, choosing an adequate value for the characteristic element size is capital to capturing the *entirety* of the physics of the problem under attack. As aforementioned, this choice will be initially rather arbitrary and based upon « intuition ». Given the characteristic length of the oscillating droplet is of the order of 10^{-3} [m], it is *assumed* that a characteristic element size of $h \sim 10^{-5}$ [m] is sufficiently small.

Another assumption that will be considered for the choice of the mesh is that most part of the physics (and more specifically, the oscillations of the droplet) happen at the free surface $\partial\Omega(t)$. In other words, it is assumed that the physics that appear in the bulk of the liquid have no need being captured as much as the physics that happen at $\partial\Omega(t)$ (Appendix 3). Subsequently, the characteristic element size in the bulk of the liquid may be set to a greater value than the characteristic element size near $\partial\Omega(t)$. For this reason, the following expression for the characteristic element h size as a function of the distance d [m] from the free surface is chosen :

$$h(d) = 10^{-5} + 0.2 \times d \text{ [m]}. \tag{II.28}$$

A visualization of this mesh for the initial configuration of the droplet is provided in Fig. II.3. For this mesh, the number of nodes is equal to 6,892 and the number of elements is equal to 13,783.

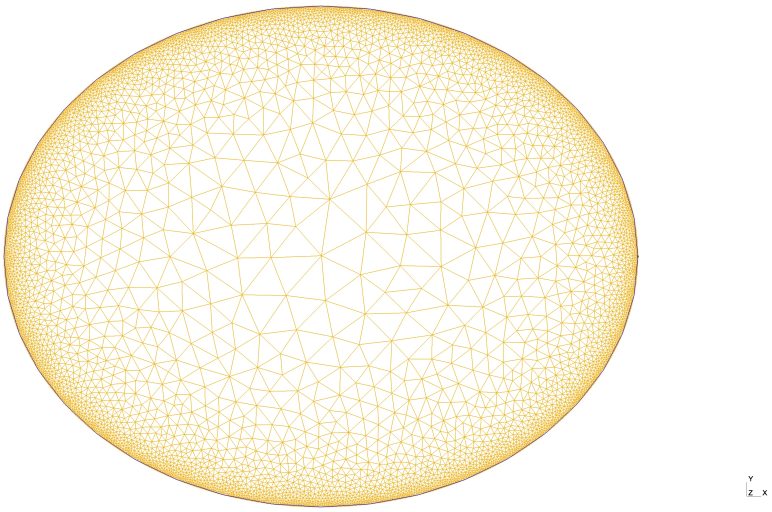

Figure II.3: Finite element mesh for the initial configuration of the water droplet (6,892 nodes, 13,783 elements).

3.2.2 Other simulation parameters

In addition to the characteristic element size, values must be assigned as well to the time-step Δt [s] and the simulation time $\mathcal{T}$ [s]. For the latter, a value of $\mathcal{T} = 0.1$ [s] is chosen. For Δt, let it be assumed that $\Delta t = 10^{-4}$ [s] is small enough. Similarly to the characteristic element size, these values are initial « guesses ». As mentioned previously, comparison between the theoretical and numerical models will reveal if this initial « guess » is sufficient.

Some remaining numerical parameters that need to be discussed are the α-parameter and the re-meshing algorithm. For the former, it has been described in Part I that the optimal value prescribed by the literature is $\alpha = 1.2$ [-]. In terms of the re-meshing algorithm, `CGALConstrainedChew` is chosen, given better element quality is guaranteed over the simulation. A discussion on performance in terms of mass conservation/element quality between `CGAL` re-meshing and `CGALConstrainedChew` re-meshing is provided in Appendix 4. For the remainder of this work, `GCALConstrainedChew` is used.

For the sake of clarity, the full set of numerical parameters is given in the table below.

Numerical parameters.

- Simulation time $\mathcal{T} = 0.1$ [s] ;
- Characteristic mesh size $h(d) = 10^{-5} + 0.2 \times d$ [m] ;
- Time-step $\Delta t = 10^{-4}$ [s] ;
- α-parameter $\alpha = 1.2$ [-].

3.3 Results and comparison with theoretical predictions

3.3.1 Theory applied to the framework of the current study

To obtain the theoretical model for the evolution of the free surface of the (water) droplet over time, it is required to determine to which damping regime the oscillations obey. To do so, the value of the reduced discriminant Δ'_n [rad/s]^2 needs to be computed using $\Delta'_n = \lambda_n^2 - \omega_{n,0}^2$, where λ_n [rad/s] is the damping rate and $\omega_{n,0}$ [rad/s] is the angular frequency of the oscillations happening at the (droplet) free surface $\partial\Omega(t)$. Using resp. Eq. II.23 and Eq. II.20 to get the value for resp. λ_n and $\omega_{n,0}$ at eigenmode $n = 2$ (the reason as to why this mode is chosen is given hereafter) :

$$\lambda_2 = 2n(n-1)\frac{\mu}{\rho R_0^2} = 1.403 \text{ [rad/s]} ; \quad \omega_{2,0} = \sqrt{n(n-1)(n+1)\frac{\gamma}{\rho R_0^3}} = 301.37 \text{ [rad/s]}, \tag{II.29}$$

it can be determined that :

$$\Delta'_2 = \lambda_2^2 - \omega_{2,0}^2 = -90,821.9 \text{ [rad/s]}^2, \tag{II.30}$$

which means that the regime in which the droplet oscillates is underdamped. Note that to obtain the results above, the following values were used for the physical quantities that appear in these equations :

- Viscosity $\mu = 10^{-3}$ [Pa $\cdot$ s] ;
- Density $\rho = 10^3$ [kg/m^3] ;
- Surface tension coefficient $\gamma = 72.8 \times 10^{-3}$ [N/m],

and correspond to those for water under normal conditions of temperature and pressure. Note also that the eigenmode $n = 2$ was chosen because it models the shape oscillations of the droplet around its equilibrium configuration. Subsequently, the governing equation of the oscillation of the free surface $\partial\Omega(t)$ of the water droplet follows Eq. II.26. From this set of equations, the following quantities are obtained :

$$\omega_2 = 301.35 \text{ [rad/s]} ; \quad \varepsilon_2^{\max} = \pm 1.88 \times 10^{-4} \text{ [m]} ; \quad \zeta_2 = \pm 4.655 \times 10^{-3} \text{ [rad]}. \tag{II.31}$$

For the two latter quantities, *i.e.* the maximal deviation from equilibrium and the phase shift, both positive and negative signs are kept for the time being. The reason for this is that their sign depends on how $\partial\Omega_0$ is implemented in the computer code. More on this will be explained in the following section.

3.3.2 Comparison with the numerical results

To determine which sign to use for $\varepsilon_2^{\max}$ and ζ_2 in Eq. II.31, some time must be spent on correctly describing the implementation of the problem in the computer model. As represented in Fig. II.2 and described in Section 3.1, $\partial\Omega_0$ consists of an ellipse with dimensions such that its characteristic size is of the order of the capillary length for water. If the $\hat{x}$-axis horizontal, pointing from left to right, and the $\hat{y}$-axis is vertical, pointing from below to above, then the droplet as drawn in Fig. II.2 is initially in compression along the $\hat{y}$-axis and in tension along the $\hat{x}$-axis. The `PFEM3D` computer code has a function which allows to track the position of one or more nodes at the free surface given a reference point (x, y). For the purpose of this study, the reference point is placed at the center of the droplet (at its center of gravity) such that the two nodes whose positions are tracked over time are placed as represented in Fig. II.4. Hence, at $t = 0$ [s], the droplet is in compression along the axis tracking the position of the nodes and thus the sign of the maximal deviation from equilibrium, $\varepsilon_2^{\max}$, is negative, and the sign of the phase shift is positive, which means :

$$\varepsilon_2^{\max} = -1.88 \times 10^{-4} \text{ [m]} ; \quad \zeta_2 = 4.655 \times 10^{-3} \text{ [rad]}. \tag{II.32}$$

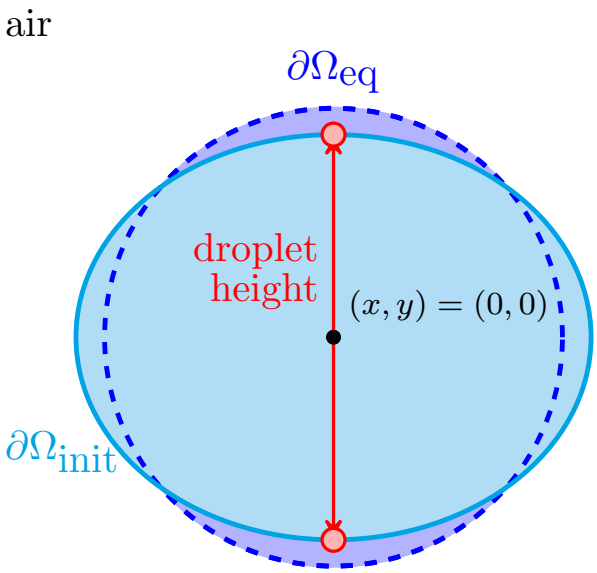

Figure II.4: Schematic of how the oscillations of the free surface are tracked over time.

Therefore, the final expression for the theoretical model of the droplet oscillations is :

$$\varepsilon_2(t) = -1.88 \times 10^{-4} \mathrm{e}^{-1.403t} \cos(301.35t + 4.655 \times 10^{-3}). \tag{II.33}$$

In the Fig. II.5, a comparison between the theoretical and numerical models is provided. The curve for the theoretical model appears in blue, the one for the numerical model in red.

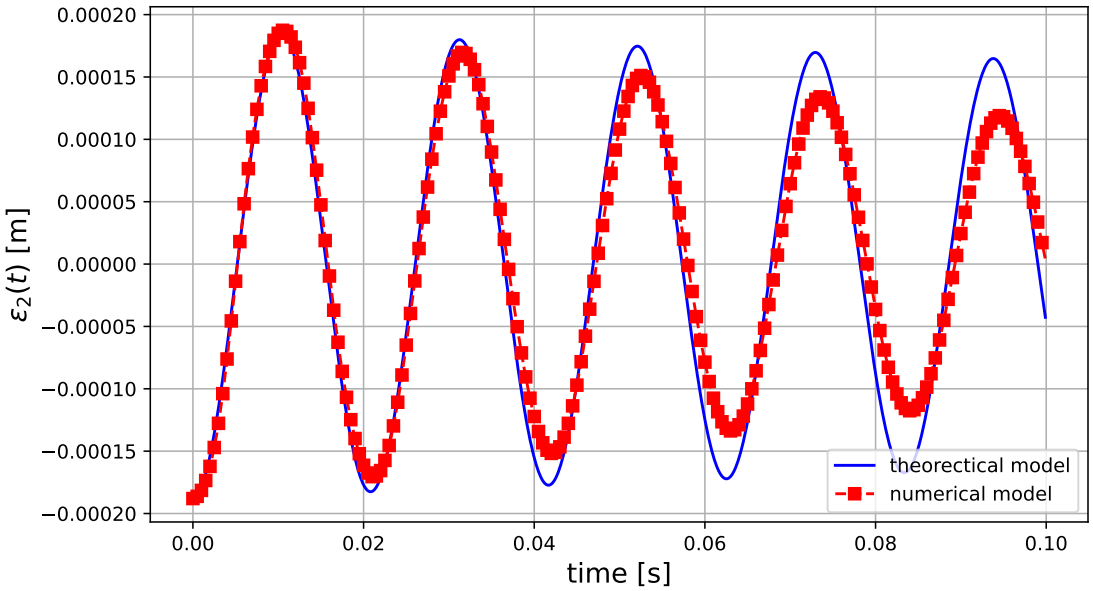

Figure II.5: Comparison between theoretical Eq. II.33 and numerical models for the droplet free surface oscillations. The used numerical parameters are $h(d) = 10^{-5} + 0.2 \times d$ [m], $\mathcal{T} = 0.1$ [s], $\Delta t = 10^{-4}$ [s] and $\alpha = 1.2$ [-].

In terms of the angular frequency, the behavior of the oscillating droplet seems to be represented correctly in the sense that $\omega_{2,0}^{\text{numerical}} \simeq \omega_{2,0}^{\text{theoretical}}$. In terms of the damping rate, on the other hand, the numerical model shows a higher one than is theoretically predicted. To quantify the error on both the angular frequency and the damping rate, respectively δ_ω [%] and δ_λ [%], the following definitions are suggested :

$$\delta_\omega = \frac{|\omega_2 - \tilde{\omega}_2|}{\omega_2} \times 100\,; \quad \delta_\lambda = \frac{|\lambda_2 - \tilde{\lambda}_2|}{\lambda_2} \times 100, \tag{II.34}$$

where ω_2 [rad/s] denotes the theoretical angular frequency and $\tilde{\omega}_2$ [rad/s] denotes the numerical angular frequency ; the same notations are used for the damping rate. From the simulation data, it can be retrieved that $\tilde{\omega}_2 = 296.37$ [rad/s] such that the associated error δ_ω evaluates to $\delta_\omega = 1.65$ [%] ; the numerical model is in excellent agreement with the predicted theoretical model *in terms of the angular frequency*. To retrieve the damping rate from the numerical data, use the logarithmic increment χ as well as the decay ratio ξ for two adjacent peaks :

$$\chi = \ln\left(\frac{x_1}{x_2}\right)\,; \quad \xi = \frac{\chi}{\sqrt{\chi^2 + (2\pi)^2}}\,; \quad \tilde{\lambda}_2 = \sqrt{\frac{\xi^2 \tilde{\omega}_2^2}{1 - \xi^2}}, \tag{II.35}$$

where x_1 and x_2 are the amplitudes of any two successive peaks. This leads to $\tilde{\lambda}_2 = 4.449$ [rad/s], which is substantially different from $\lambda_2 = 1.403$ [rad/s]. Indeed, the related error

evaluates to $\delta_\lambda = 217.1$ [%].

The nature of this significant error on the damping most probably originates from the choice of the values of the characteristic element size as well as that of the time-step. In the following sections, these options will be considered and studied in a case-per-case approach.

3.4 Influence of the numerical parameters on the quality of the simulation results

3.4.1 Characteristic element size

In the previous section, the characteristic element size had been set to a value of $h(d) = 10^{-5} + 0.2 \times d$ [m] as a function of the distance d from the (droplet) free surface $\partial\Omega(t)$. Here, to study how $h(d)$ influences the result quality, this previously set value will be increased and decreased, and the consensus should be that the result quality improves when $h(d)$ decreases and that it degrades when $h(d)$ increases.To perform this study, the following values for $h(d)$ are chosen in a first instance :

- $h(d) = 10^{-4} + 0.2 \times d$ [m] (482 nodes, 963 elements) ;
- $h(d) = 5 \times 10^{-5} + 0.2 \times d$ [m] (1,145 nodes, 2,289 elements) ;
- $h(d) = 10^{-5} + 0.2 \times d$ [m] (initial) ;
- $h(d) = 5 \times 10^{-6} + 0.2 \times d$ [m] (14,025 nodes, 28,049 elements).

Apart from $h(d)$, no other numerical parameters are changed with respect to the previous section, which means that the full set of numerical parameters is :

- Simulation time $\mathcal{T} = 0.1$ [s] ;
- Characteristic mesh size variable (see hereabove) ;
- Time-step $\Delta t = 10^{-4}$ [s] ;
- α-parameter $\alpha = 1.2$ [-].

A comparison between the theoretical predictions and the simulation data for varying characteristic element sizes is provided in Figs II.6a, II.6b.

Apparently, the behavior of the numerical response doesn't change in the slightest for decreasing element sizes. This means that convergence of the numerical response in terms of $h(d)$ is attained before descending up to 10^{-4} [m]-element scales. This information is important in the sense that the CPU-time can be minimized quite drastically while maintaining result quality, as larger elements means less elements in the mesh, meaning there are less computations to be performed by the computer code. To give some orders of magnitude, the table below displays the CPU-times for the simulation using various characteristic element sizes.

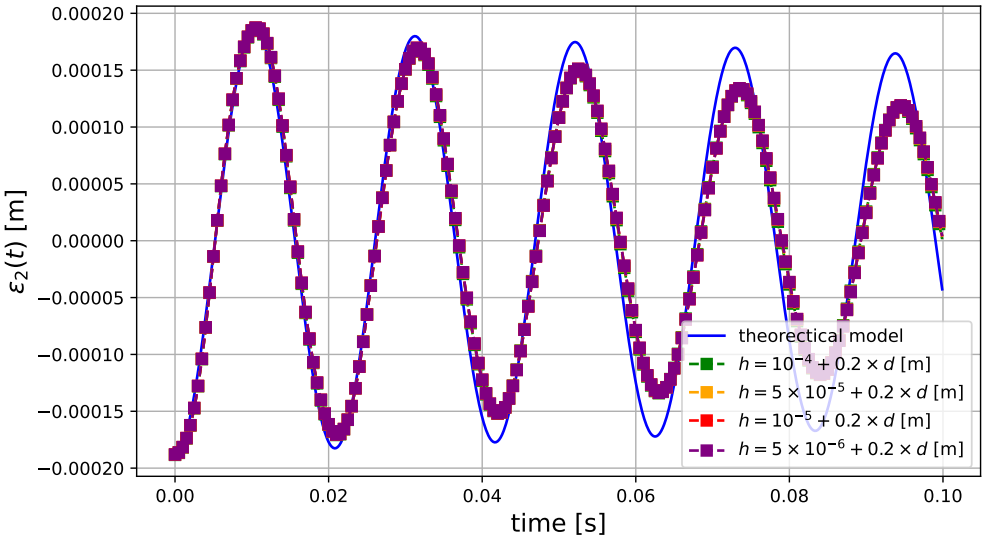

(a) Comparison between the theoretical model Eq. II.33 and the numerical solution for varying values of $h(d)$.

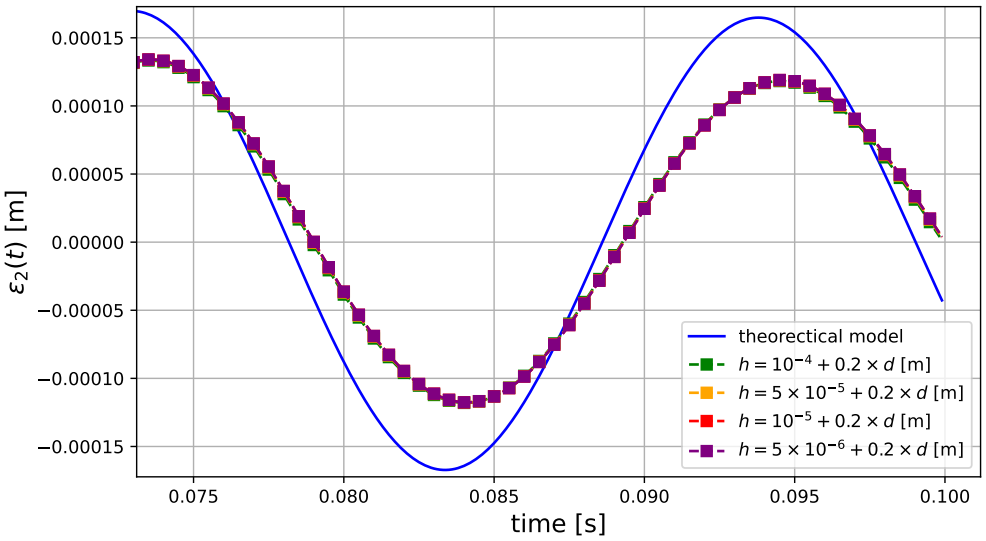

(b) Zoom on Fig. II.6a.

Figure II.6: Study of the numerical convergence as a function of $h(d)$.

CPU-time as a function of $h(d)$ (4 threads, using `OpenMP` parallel computing).

- $h = 10^{-4} + 0.2 \times d$ [m] : CPU-time = 138 [s] ;
- $h = 5 \times 10^{-5} + 0.2 \times d$ [m] : CPU-time = 218 [s] ;
- $h = 10^{-5} + 0.2 \times d$ [m] : CPU-time = 918 [s] ;
- $h = 5 \times 10^{-6} + 0.2 \times d$ [m] : CPU-time = 1,876 [s].

For future simulations (in this part of the work), the value of the characteristic element size can thus be set to the lowest value appearing in the table hereabove, given result quality is maintained and CPU-time is minimized. Until mention of the contrary : $h(d) = 10^{-4} + 0.2 \times d$ [m].

3.4.2 Time-step

While numerical convergence of the solution for relatively coarse meshes is positive in terms of the CPU-time as well as for reducing the complexity of the mesh, it doesn't advance the search for the question as to why it is incapable of following correctly the theoretical predictions in terms of the damping rate. Another simulation parameter that is generally known to impact significantly the quality of the (numerical) results is the time-step Δt. In order to study the effect of this parameter on the simulation results, different values for Δt are set and compared to one another, exactly as has been done in the previous section when the influence of $h(d)$ was investigated. To perform this study, the following values for Δt were chosen[6] :

- $\Delta t = 10^{-3}$ [s] ;
- $\Delta t = 10^{-4}$ [s] ;
- $\Delta t = 10^{-5}$ [s] ;
- $\Delta t = 10^{-6}$ [s],

such that from one refinement to another, the time-step is divided by one order of magnitude. Once more, the varying numerical parameter is the only one that changes from one simulation from another, which means that the other simulation parameters are set to the following values :

- Simulation time $\mathcal{T} = 0.1$ [s] ;
- Characteristic mesh size $h(d) = 10^{-4} + 0.2 \times d$ [m] (previously determined to be « optimal ») ;
- Time-step variable (see hereabove) ;
- α-parameter $\alpha = 1.2$ [-].

A comparison between the numerical results for varying values for Δt and the theoretical predictions is provided in the set of figures Figs. II.7a, II.7b.

In contrast with varying the value of the characteristic element size $h(d)$, changing the value of the time-step from one simulation to another influences drastically the quality of the simulation results. It can indeed be observed that it improves as Δt decreases. The reason for this observation is that the integration scheme that is implemented in `PFEM3D` is a backward-Euler one, well-known for its prominent numerical damping. As displayed in the set of figures Figs. II.7a, II.7b, minimizing this phenomenon means that the value of Δt must be set as low as possible. However, as was the case for decreasing

[6] Remind that previously (*cf.* Section 3.2.2), the value of the time-step had been set to $\Delta t = 10^{-4}$ [s].

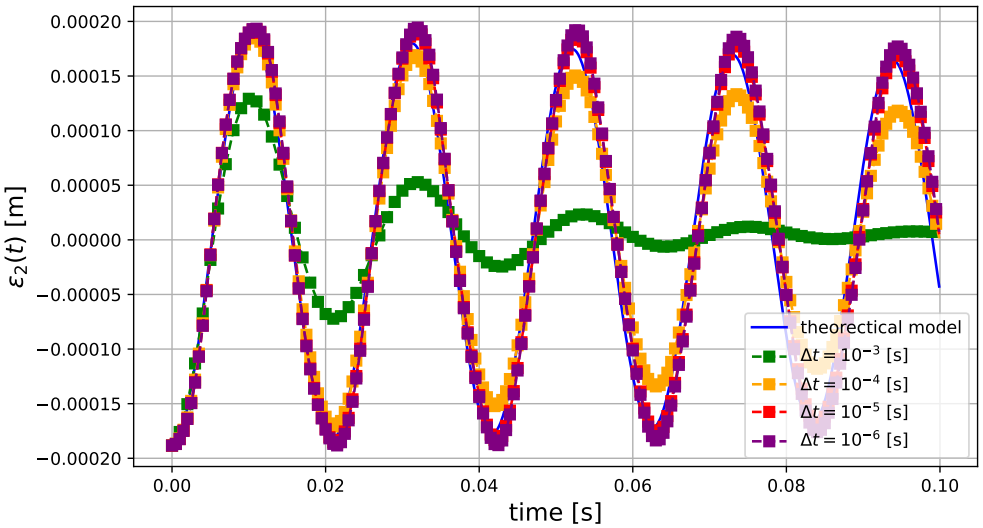

(a) Comparison between the theoretical model Eq. II.33 and the numerical solution for varying Δt.

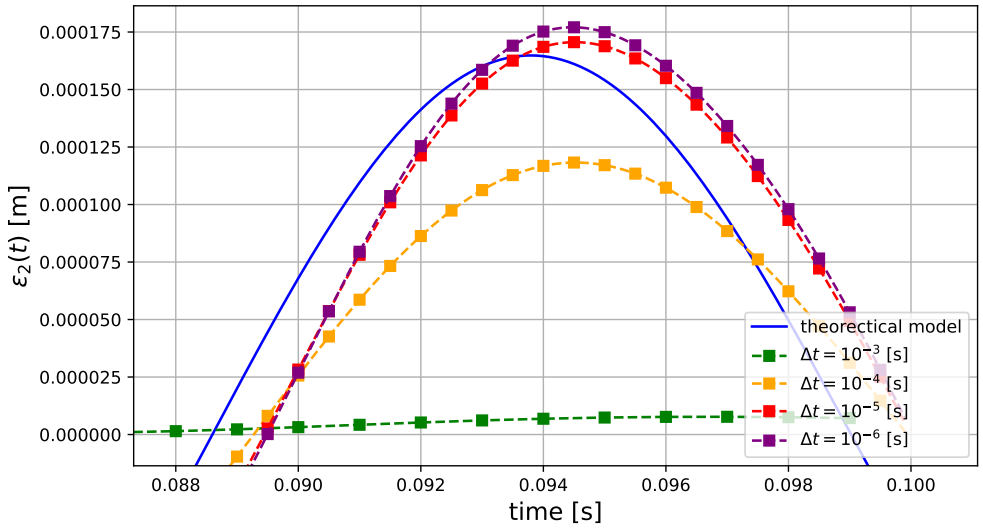

(b) Zoom on Fig. II.7a.

Figure II.7: Study of the numerical convergence as a function of Δt.

the characteristic element size, decreasing Δt means increasing the CPU-time. To give some orders of magnitude, the table below displays the CPU-times for the different values of the time-step, chosen previously.

CPU-time as a function of Δt (4 threads, `OpenMP` parallel programming.

- $\Delta t = 10^{-3}$ [s] : CPU-time = 13.7 [s] ;
- $\Delta t = 10^{-4}$ [s] : CPU-time = 138 [s] ;
- $\Delta t = 10^{-5}$ [s] : CPU-time = 590 [s] ;
- $\Delta t = 10^{-6}$ [s] : CPU-time = 3,767 [s].

While the CPU-time for values of Δt set between 10^{-3} [s] and 10^{-5} [s] is reasonable, this is not the case when $\Delta t = 10^{-6}$ [s]. To explain the usage of the word « reasonable » here, recall that the value for the characteristic element size $h(d)$ here is set to $10^{-4}+0.2\times d$ [m], which is only one order of magnitude lower than the droplet characteristic size. Hence, if a situation would present itself in which $h(d)$ needs to be two or even three orders of magnitude lower than the characteristic droplet size, the CPU-time using $\Delta t = 10^{-6}$ [s] would sky-rocket. Until mention of the contrary, the value of the time-step Δt is hence set to $\Delta t = 10^{-5}$ [s], given it yields optimal simulation result quality for lower CPU-times.

3.4.3 What if $h(d)$ is reduced further ?

As discussed in the two previous sections, numerical parameters such as the characteristic element size and the time-step Δt influence significantly the CPU-time in the sense that the smaller their value is set, the higher the CPU-time gets. Tt has been pointed out that the minimal time-step should be set at a value of 10^{-5} [s] in order to minimize the effect of numerical diffusion due to the implementation of the backward-Euler time-integration scheme. In contrast, no such value for the characteristic element size has been found yet. Therefore, in the current section, even larger values for $h(d)$ will be set to uncover up to which characteristic element size the quality of the numerical solution is preserved, and if this allows for an even further decrease of the CPU-time to complete the computation.

To perform this analysis, the following values for the characteristic element size $h(d)$ are set (note that the values for other numerical parameters, such as the time-step Δt, remain as prescribed previously, namely $\Delta t = 10^{-5}$ [s], $\mathcal{T} = 0.1$ [s] and $\alpha = 1.2$) :

- $h(d) = 10^{-4} + 0.2 \times d$ [m] (initial) ;
- $h(d) = 5 \times 10^{-4} + 0.2 \times d$ [m] (53 nodes, 105 elements) ;
- $h(d) = 10^{-3} + 0.2 \times d$ [m] (18 nodes, 35 elements),

where the last choice is such that the (characteristic) element size is of the order of that of the droplet itself. These meshes are displayed in Figs II.8a, II.8b and II.8c. For these values, the comparison between the theoretical and simulation results are displayed in Fig. II.9.

It can be observed that for values of the characteristic element size that get closer to the droplet size, the representation of the oscillation behaviour gets worse. Indeed, the larger $h(d)$ gets, the more the oscillations shift downwards in the sense the the average value of $\varepsilon_2(t)$ is no longer zero, but negative. A computation of this average value is given below as a function of the value of $h(d)$:

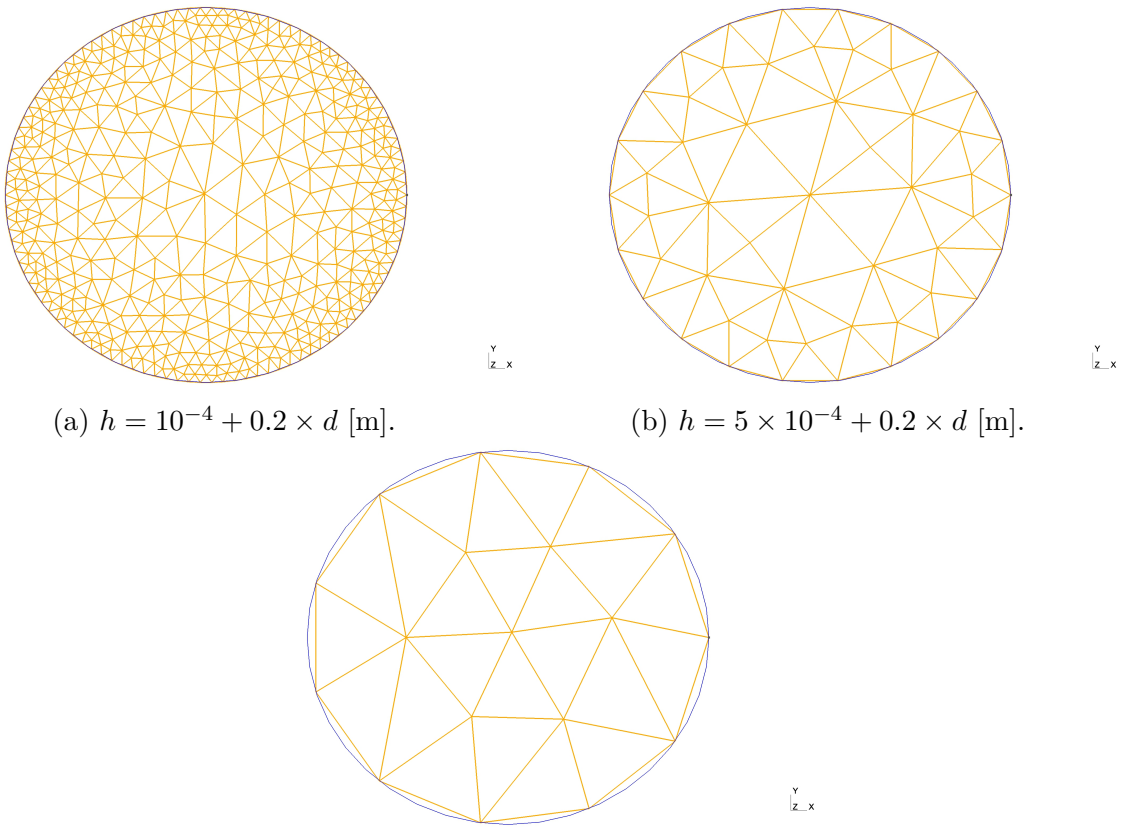

(a) $h = 10^{-4} + 0.2 \times d$ [m].

(b) $h = 5 \times 10^{-4} + 0.2 \times d$ [m].

(c) $h = 10^{-3} + 0.2 \times d$ [m].

Figure II.8: Representation of the FE meshes mentioned above.

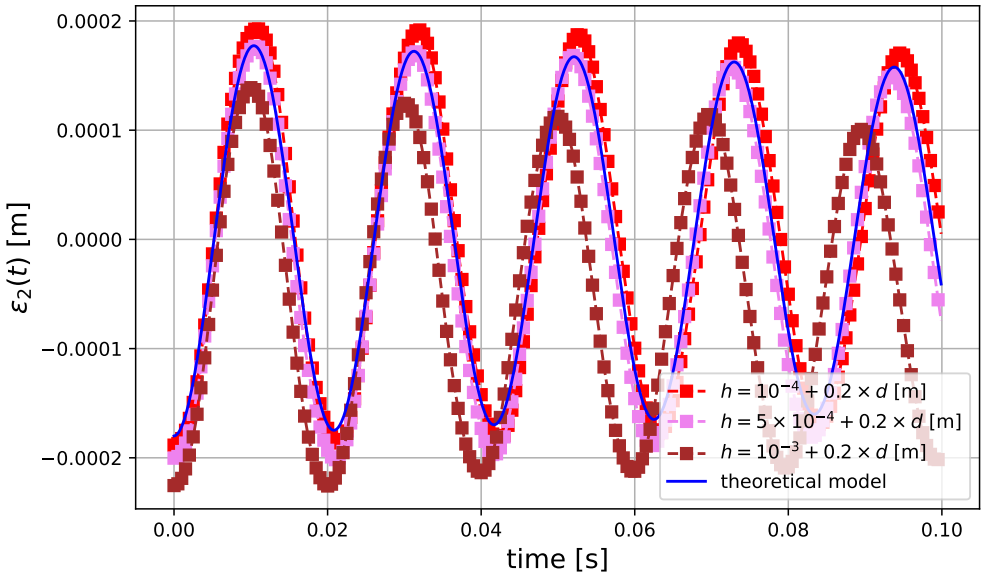

Figure II.9: Comparison of the evolution of $\varepsilon_2(t)$ for different characteristic mesh sizes $h(d)$.

- $h(d) = 10^{-4} + 0.2 \times d$ [m] : $\bar{\varepsilon}_2(t) \simeq 8 \times 10^{-6}$ [m] ;
- $h(d) = 5 \times 10^{-4} + 0.2 \times d$ [m] : $\bar{\varepsilon}_2(t) \simeq -10^{-5}$ [m] ;
- $h(d) = 10^{-3} + 0.2 \times d$ [m] : $\bar{\varepsilon}_2(t) \simeq -5 \times 10^{-5}$ [m],

where $\bar{\varepsilon}_2(t)$ denotes the average value of $\varepsilon_2(t)$. Another observation that directly arises from Fig. II.9 is that the angular frequency increases with $h(d)$ as well, such that for $h(d) = 10^{-3} + 0.2 \times d$ [m], the value of $\tilde{\omega}_2$ is higher than the theoretically predicted one. In terms of the CPU-time, its value for $h(d) = 10^{-4} + 0.2 \times d$ [m] is 519 [s] while it is 120 [s] for $h(d) = 10^{-3} + 0.2 \times d$ [m], which is significantly less (there is indeed a factor ~ 4 between these values), but comes with important result degradation.

3.5 Results and comparison with theoretical predictions for « optimal » simulation parameters

To finish this section regarding the problem $\partial\Omega_0 \simeq \partial\Omega_{\text{eq}}$, a comparison between the theoretical model and the obtained numerical results using the « optimal » parameters determined previously will be performed, given numerical convergence is reached for this set of values :

- $h(d) = 10^{-4} + 0.2 \times d$ [m] ;
- $\Delta t = 10^{-5}$ [s] ;
- $\mathcal{T} = 0.1$ [s] ;
- $\alpha = 1.2$ [-].

The graph displaying this comparison is represented Fig. II.10.
Using the data provided by this graph, the following values for the angular frequency $\tilde{\omega}_2$ and damping rate $\tilde{\lambda}_2$ can be determined :

$$\tilde{\omega}_2 = 293.6 \text{ [rad/s]} ; \quad \tilde{\lambda}_2 = 1.518 \text{ [rad/s]}, \tag{II.36}$$

Which leads to the following associated errors :

$$\delta_\omega = 2.57 \text{ [\%]} ; \quad \delta_\lambda = 12.68 \text{ [\%]}. \tag{II.37}$$

While the error on the angular frequency is slightly increased with respect to the numerical model used in Section 3.3, it has drastically decreased on the damping rate.

3.6 Conclusion on the case study $\partial\Omega_0 \simeq \partial\Omega_{\text{eq}}$

In this section, it has been shown that the `PFEM3D` computer code is able to model « quite correctly » the behaviour of an oscillating water droplet in zero-gravity. The term « quite correctly » is used here because the « total » error on the simulation results (with respect to the theoretical model) remains of the order of 10 [%], which is not low enough yet. Given the computer code does not lack any physical phenomenology with respect to the 2D Rayleigh model, the only possible reason as to why there is still some lack in accuracy is

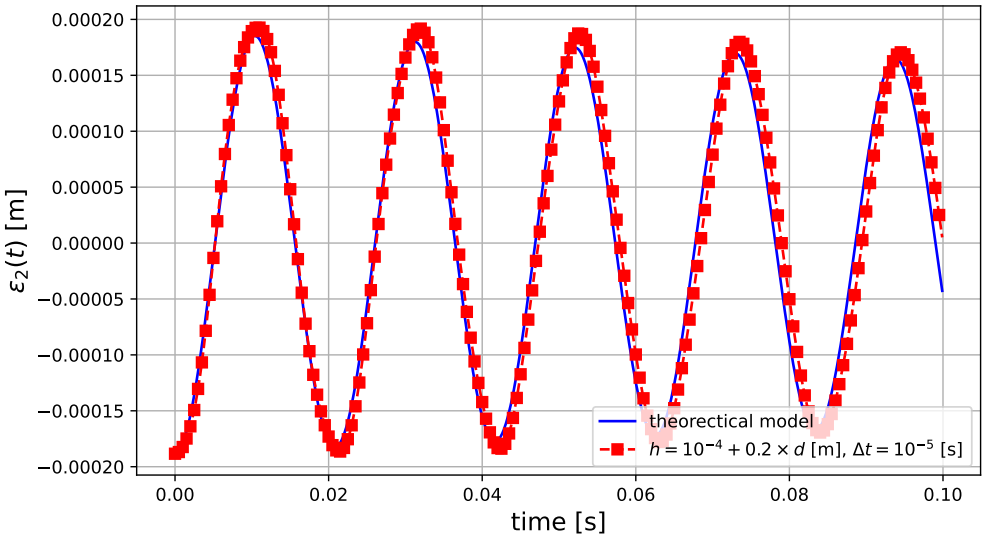

Figure II.10: Comparison of the evolution of $\varepsilon_2(t)$ using « optimal » simulation parameters.

that the initial deformation of the droplet is not small « enough ». To examine this claim, a smaller initial deviation from equilibrium is suggested and the subsequent numerical results are investigated in the following section. Let it be underlined, however, that so far, the results are encouraging : indeed, once an optimal set of simulation parameters is obtained, the representation of the angular frequency is extremely close to the predicted value (with only an error of ~ 3 [%]), and that of the damping rate gets closer to its expected result.

4 $\partial\Omega_0 \simeq \partial\Omega_{\mathbf{eq}}$ with an even smaller initial deformation

To see up to which point the numerical model is able to correctly represent the 2D Rayleigh theory, a case must be presented in which the initial deviation from equilibrium of the droplet should be as small as possible from its equilibrium configuration. For this study, the initial droplet shape of an ellipse is used yet again (*cf.* Fig. II.2), but with major/minor axes that have almost identical values.

Geometry parameters.

- Initial geometry/configuration : major axis $a = 1.75$ [mm], minor axis $b = 1.629$ [mm] ;
- Equilibrium geometry/configuration : equilibrium radius $R_0 = 1.688$ [mm] ;
- For both initial/equilibrium configurations : surface area $A = 8.9535$ [mm]^2.

Note that the values for the couple $\{a, b\}$ are chosen such that the surface area A of the droplet is the same as in the case studied in Section 3. In terms of the deviation from

equilibrium, the following results are easily computed :

$$\Delta_a = 3.67\ [\%]\ ; \quad \Delta_b = 3.49\ [\%]. \tag{II.38}$$

Hence, the error for this study is ~ 4 times lower than the one in Section 3. On the choice of the numerical parameters, the set of « optimal » numerical parameters determined in Section 3.4 will also be used for this case study ; these are reminded below :

- $h(d) = 10^{-4} + 0.2 \times d$ [m] ;
- $\Delta t = 10^{-5}$ [s],

as well as $\mathcal{T} = 0.1$ [s] and $\alpha = 1.2$ [-].

4.1 Results and comparison with theoretical predictions

To obtain the theoretical model describing the oscillations $\varepsilon_2(t)$ of the droplet free surface $\partial\Omega(t)$ over time, the values of $\omega_{2,0}$ and λ_2 must be determined in a first instance. From Eqs. II.20 and II.23, neither the angular frequency nor the damping rate depend on the initial droplet configuration $\partial\Omega_0$. Their value doesn't change with respect to the previous case study, hence :

$$\omega_{2,0} = 301.37\ [\text{rad/s}]\ ; \quad \lambda_2 = 1.403\ [\text{rad/s}], \tag{II.39}$$

and also, using Eq. II.26 :

$$\omega_2 = 301.35\ [\text{rad/s}]. \tag{II.40}$$

On the contrary, the values of $\varepsilon_2^{\max}$ as well as that of ζ_2 depend on $\partial\Omega_0$ (*cf.* Eq. II.26) ; their values become :

$$\varepsilon_2^{\max} = 6.2 \times 10^{-5}\ [\text{m}]\ ; \quad \zeta_2 = 4.655 \times 10^{-3}\ [\text{rad}], \tag{II.41}$$

where ζ_2 remains practically unchanged with respect to the previous case study. Therefore, the expression of $\varepsilon_2(t)$ takes the following form :

$$\varepsilon_2(t) = -6.2 \times 10^{-5} \mathrm{e}^{-1.403t} \cos(301.35t + 4.655 \times 10^{-3}), \tag{II.42}$$

where the sign before $\varepsilon_2^{\max}$ is negative once again due to the implementation of the initial geometry.

Using the parameters described previously (*cf.* introduction Section 4), the following graph is obtained for the comparison between the theoretical model Eq. II.42 and the numerical results (Fig. II.11).

From sight alone, the theoretical and numerical models seem to be almost identical, except for a damping rate that looks slightly overestimated by the latter. To evaluate this error quantitatively, get the values for $\tilde{\omega}_2$ and $\tilde{\lambda}_2$ from Fig. II.11 :

$$\tilde{\omega}_2 = 300.99\ [\text{rad/s}]\ ; \quad \tilde{\lambda}_2 = 1.432\ [\text{rad/s}], \tag{II.43}$$

and then use Eq. II.34 to retrieve :

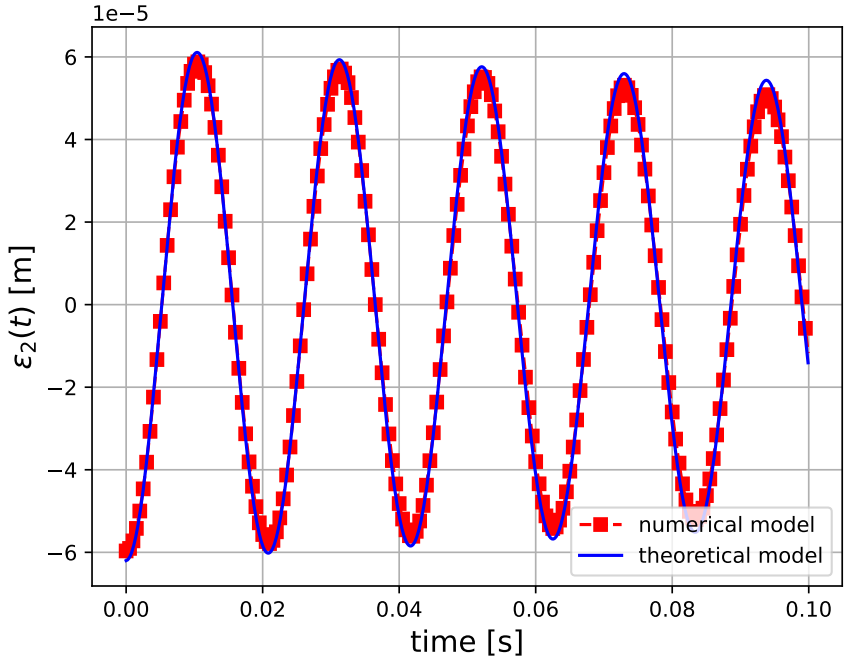

Figure II.11: Comparison between the theoretical model Eq. II.42 and the simulation results using the parameters described hereabove : the used characteristic element size is $h(d) = 10^{-4} + 0.2 \times d$ [m] and the value for the time-step $\Delta t = 10^{-5}$ [s]. The maximal deviation from equilibrium is $\Delta_a = 3.67$ [%].

$$\delta_\omega = 0.119 \text{ [\%]} ; \quad \delta_\lambda = 2.087 \text{ [\%]}. \tag{II.44}$$

It is clear that the numerical results are in almost perfect agreement with the theoretical predictions.

To recapitulate the difference between this study and the one in the previous section (Section 3), the current one uses an initial deviation that is four times lower than the previous one, hence satisfying the small oscillation approximation better. Subsequently, it has been found that the accuracy of the numerical result with respect to the theoretical model has improved by ~ 10 [%] (from 12.93 [%] to 2.09 [%]). Not only does this show that the `PFEM3D` computer code is able to model correctly the 2D Rayleigh model if its underlying assumptions are satisfied, but also that the quality of the provided results is such that there is virtually almost no difference between the two models. It is therefore correct to conclude that if the hypotheses for the 2D Rayleigh model are satisfied, *i.e.* if the model *can* be applied to a case study, the numerical model is in excellent agreement with the former and models correctly the oscillations of the droplet free surface.

A final case that will be considered in the framework of the current study is that in which the initial deviation from equilibrium is large, such that $\partial\Omega_0$ is « far away » from $\partial\Omega_{\text{eq}}$ (Section 5). The reason for this case to be presented in this work is simply to show that, as predicted by the 2D Rayleigh model for droplet oscillations in zero-gravity, the free surface oscillations can no longer be described by a linear combination of uncoupled

oscillation modes[7].

5 Testing of the theoretical model on a large initial deviation from equilibrium

In the two previous sections, it has been demonstrated that the `PFEM3D` computer code is able to represent correctly the 2D Rayleigh model for oscillating droplets in zero-gravity when the initial deviation from equilibrium is « small enough ». More specifically, it has been proven that the smaller this initial deviation from equilibrium is (recall that the maximal deviation from equilibrium was set to a value of 3.67 [%]), the greater the correspondence between the theoretical predictions and the simulation data becomes. Even when $\partial\Omega_0$ is « not so close to » $\partial\Omega_{\text{eq}}$ (*cf.* Section 3, in which the maximal deviation from equilibrium was set to 12.5 [%]), `PFEM3D` is able to track the droplet free surface oscillations with acceptable accuracy. As a final case study, the opposite is considered : an example in which the initial deviation from equilibrium is way too large for the 2D Rayleigh model to be applied.

5.1 Implementation of the initial geometry and numerical parameters

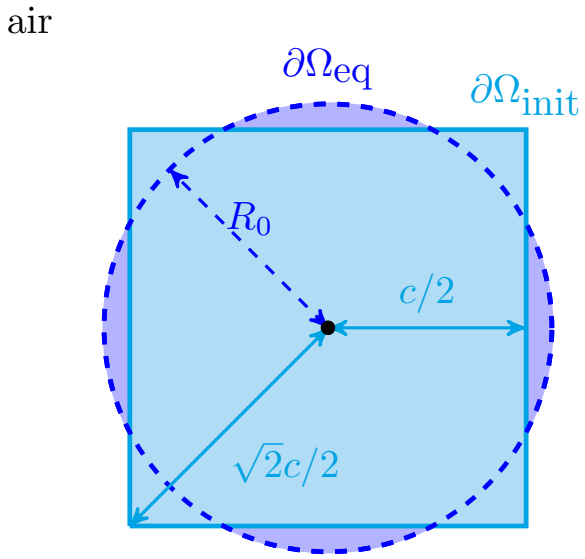

Figure II.12: Representation of the initial and equilibrium configurations of an oscillating water droplet in zero-gravity as well as the respective geometry parameters.

To perform this study, consider the geometry suggested in *cf.* Fig. II.12, which sets $\partial\Omega_0$ to be a square-shaped droplet. The geometry parameters that are represented in this figure are given below.

[7]Indeed, for initial configurations that are significantly different from the equilibrium configuration, the resulting free surface oscillations are prescribed by a linear combination of *coupled* oscillation modes.

Geometry parameters.

- Initial geometry/configuration : side length $c = 2.992$ [mm] ;
- Equilibrium geometry/configuration : equilibrium radius $R_0 = 1.688$ [mm] ;
- For both initial/equilibrium configuration : surface area $A = 8.9535$ [mm]^2.

Once more, the choice of these parameters is such that the surface area is preserved with respect to the two previous cases (Sections 3 and 4). In terms of the numerical parameters, these remain :

- Characteristic element size $h(d) = 10^{-4} + 0.2 \times d$ [m] ;
- Time-step $\Delta t = 10^{-5}$ [s] ;
- Simulation time $\mathcal{T} = 0.1$ [s] ;
- Alpha-parameter $\alpha = 1.2$ [-].

5.2 Results and comparison with theoretical predictions

The theoretical model for the droplet free surface oscillations considering $\partial\Omega_0$ as modeled in Fig. II.12 is deduced from Eq. II.26, where $\omega_{2,0}$, λ_2 and hence ω_2 are unchanged with respect to the previous cases given these quantities do not depend on the initial configuration. The values that do require re-evaluation are $\varepsilon_2^{\max}$ and ζ_2 and are also computed along Eq. II.26, which yields :

$$\varepsilon_2^{\max} = 1.92 \times 10^{-4} \text{ [m]} ; \quad \zeta_2 = 4.655 \times 10^{-3} \text{ [rad]}, \tag{II.45}$$

meaning that the governing equation for the droplet free surface oscillations reads :

$$\varepsilon_2(t) = -1.92 \times 10^{-4} \mathrm{e}^{-1.403t} \cos(301.35t + 4.655 \times 10^{-3}). \tag{II.46}$$

The comparison between the theoretical model and the obtained numerical results is given in Fig. II.13. As expected, the correspondence between the two curves is nonexistent, because the required hypotheses for the 2D Rayleigh model on droplet oscillations in zero-gravity are not satisfied, namely the initial deviation from equilibrium is not small enough in order to fall under the umbrella of « small oscillations ». Indeed, from Fig. II.12, it can be deduced that the maximal deviation from equilibrium is of the order of 25 [%]. Furthermore, given the shape of the initial configuration, there is a pressure singularity that is generated at each corner of the square-shaped droplet according to Laplace's law (expressed in two dimensions given the framework of the current study) :

$$\Delta p \sim \frac{\gamma}{\mathcal{R}}, \tag{II.47}$$

where $\mathcal{R}$ [m] is the radius of curvature and tends to zero at the corners of the square-shaped droplet. This « infinite » pressure differential generates a shock wave that emphasizes the amplitude of the droplet oscillations, which is why the red curve near $t = 0$ [s] exceeds the blue one in terms of amplitude.

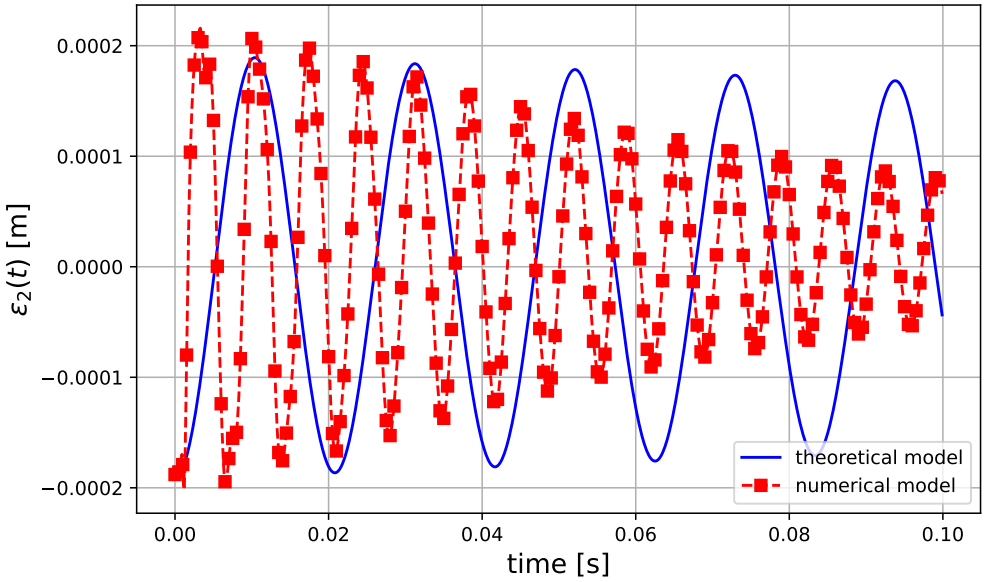

Figure II.13: Comparison between the theoretical model Eq. II.46 and the simulation results using the parameters described hereabove : the characteristic element size is $h(d) = 10^{-4} + 0.2 \times d$ [m] and the value for the time-step $\Delta t = 10^{-5}$ [s]. The maximal deviation from equilibrium is of the order of 25 [%].

In Section 2.2, it has been explained that one of the hypotheses for the 2D Rayleigh model to work is that the droplet free surface oscillations should be *small*. Indeed, when this hypothesis is satisfied, the free surface oscillations can mathematically be described as the linear combination of elementary oscillation modes that are *independent*, or rather *uncoupled*, from one another. While for large oscillations the fact that any oscillation pattern can be described as a linear combination of elementary oscillation modes remains true, the statement that they are uncoupled is totally false, which is what will be demonstrated in the following section.

5.2.1 Correction of the theoretical model to higher-order oscillation modes

From Eq. II.11, the radius R of the droplet at any point θ of time t can be expressed as :

$$R(\theta, t) = R_0 + f(\theta, t) \simeq R_0 \left[1 - \frac{1}{4} \sum_{n \geq 2} \varepsilon_n^2 + \sum_{n \geq 2} \varepsilon_n \cos(n\theta) \right], \tag{II.48}$$

where the second equality relies on the fact that the elementary oscillation modes are uncoupled. Setting θ to an arbitrarily fixed value, consider $\theta = 0$ [rad] for the sake of simplicity such that $\cos(n\theta) = 1 \ \forall n \in \mathbb{N}, n \geq 2$, the expression above can be re-written as follows, $\forall n \in \mathbb{N}, n \geq 2$:

$$R(\theta = 0, t) \simeq R_0 \left[1 - \frac{1}{4} \sum_{n \geq 2} \varepsilon_n^2 + \sum_{n \geq 2} \varepsilon_n \right]. \tag{II.49}$$

To work further on this expression Eq. II.49, suggest calculating the order of magnitude of the dominant oscillation mode, which is $n = 4$ in this case, according to Eq. II.26 :

$$\varepsilon_4^{\max} = \sqrt{\varepsilon_4^2(0) + \left(\frac{\dot{\varepsilon}_4(0) + \lambda_4 \varepsilon_4(0)}{\sqrt{-\Delta_4'}}\right)^2}. \tag{II.50}$$

The values for $\varepsilon_4(0)$, $\dot{\varepsilon}_4(0)$, λ_4 and Δ_4' are, respectively[8] :

$$\varepsilon_4(0) = 7.33{\times}10^{-4}\ [\text{m}]; \quad \dot{\varepsilon}_4(0) = 0\ [\text{m/s}]; \quad \lambda_4 = 8.422\ [\text{rad/s}]; \quad \Delta_4' = -908,095\ [\text{rad/s}], \tag{II.51}$$

such that :

$$\varepsilon_4^{\max} = 7.33 \times 10^{-4}\ [\text{m}]. \tag{II.52}$$

Note that $\varepsilon_4^{\max} > \varepsilon_2^{\max}$, which underlines that the elementary oscillation mode $n = 4$ is dominant over $n = 2$. Hence, the order of magnitude of $\varepsilon_4(t)$ is 10^{-4} [m], implying $\varepsilon_4^2 \ll \varepsilon_4$ such that Eq. II.49 can be re-written as follows :

$$R(\theta = 0, t) \simeq R_0 \left[1 - \frac{1}{4}\sum_{n\geq 2} \varepsilon_n^2 + \sum_{n\geq 2} \varepsilon_n\right] \simeq R_0 \left[1 + \sum_{n\geq 2} \varepsilon_n\right]. \tag{II.53}$$

Therefore, the corrected expression of the theoretical model includes the elementary oscillation mode $n = 4$, leading ultimately to (denote $\varepsilon(t)$ the amplitude of the free surface oscillations taking into account the elementary modes $n = 2$ and $n = 4$ to alleviate notations) :

$$\varepsilon(t) = \overbrace{-1.92 \times 10^{-4} \mathrm{e}^{-1.403t} \cos(301.35t + 4.655 \times 10^{-3})}^{\text{mode } n=2} \underbrace{-7.33 \times 10^{-4} \mathrm{e}^{-8.422t} \cos(952.94t + 5.313 \times 10^{-4})}_{\text{mode } n=4}, \tag{II.54}$$

which is the corrected expression of the theoretical model, taking into consideration that $n = 4$ is the dominant mode rather than $n = 2$ given the small oscillation approximation no longer holds, as well as considering that these oscillation modes operate independently from one another. The graph for this comparison is provided in Fig. II.14.

Without any surprise, the theoretical and numerical curves do, once more, not match at all. As expressed numerous times already, this is due to the fact that the hypotheses for the 2D Rayleigh model are not satisfied, namely the initial deviation from equilibrium is too significant. This means that the assumption that the droplet free surface oscillations can be described as a linear combination of uncoupled elementary oscillation modes no longer holds.

In Appendix 5, some simulation snapshots are provided, as well as some supplementary remarks regarding the resulting oscillation pattern. For previous studies, such figures

[8] The value of $\varepsilon_4(0)$ is retrieved after performing a Fourier decomposition on the initial geometry $\partial\Omega_0$ from Fig. II.12.

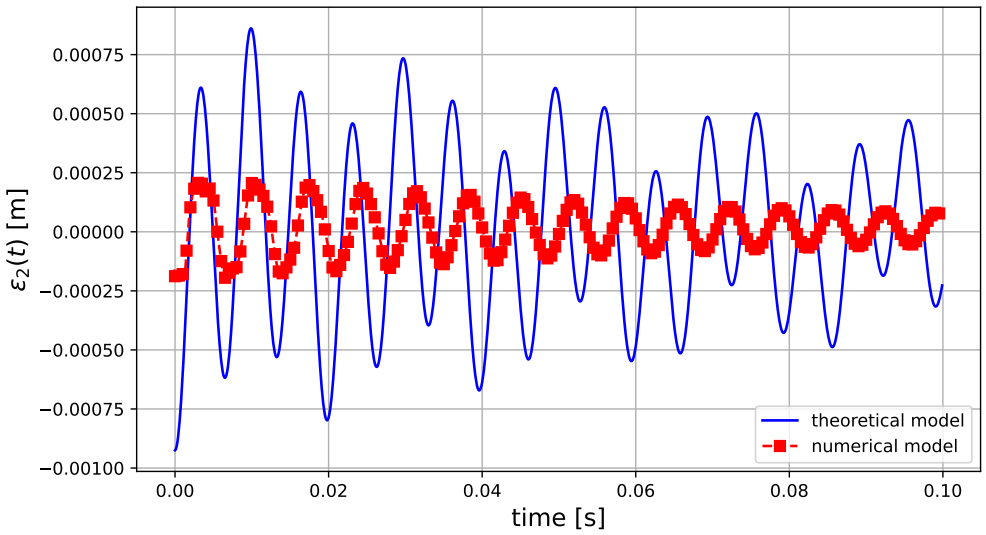

Figure II.14: Comparison between the now corrected theoretical model Eq. II.54 and the simulation results using the parameters described hereabove.

have not been displayed, simply because nothing interesting was to be observed. More specifically, the droplet oscillation pattern for small initial deviations from equilibrium are such that the ellipse shifts its maxima/minima from the $\hat{x}$-axis onto the $\hat{y}$-axis, and so forth. Furthermore, given it has only been proven at the end of Section 4 that the numerical model is correct (once more, at the moment, this has just been proven for small enough deviations from equilibrium, given this is the limit for the 2D Rayleigh theory), it wouldn't have made any sense to present such snapshots, given they could very well have been completely false.

6 Conclusion

In this part of the work, the main focus was to show that `PFEM3D` is able to model simple fluid dynamics problems at millimetre-scales, and more specifically the effects of surface tension, for reasons that have been explained in Part I. To perform this study, the 2D Rayleigh model has been chosen because it is related to the nature of the problem studied in the following part of this work. Three case studies were presented, on a scale from « ideal conditions of applicability » to « worst conditions of applicability ». For the former, Sections 3 and 4 have proven that the better the hypotheses for the 2D Rayleigh theory were satisfied (*i.e.* the closer the initial deformation of the droplet free surface is to its equilibrium configuration), the greater the accuracy of the numerical results turned out to be. Indeed, even for an initial deviation from equilibrium that didn't turn out to be so small after all (Section 3), `PFEM3D` provided a numerical solution with reasonable error (of the order of 10 [%]). This error then reduced to $\simeq 2$ [%] when an even smaller deviation from equilibrium was considered.

Part III
Extension of PFEM3D : modelling of droplet oscillations on a substrate

The previous part of this work consisted of a verification of the PFEM3D computer model applicability for basic fluid dynamics problems at millimeter scales. The current part of this work will focus on the extension of the PFEM3D computer code to take into account contact phenomena such as *contact angle hysteresis* (*cf.* Part IV). Previously, the context of the study was that of an oscillating droplet in zero-gravity where no contact with any substrate was considered. As described in Part I, the modelling of contact phenomena (*e.g.* contact angle hysteresis) requires the implementation of a set of additional contributions, such as the *surface tension force* and *liquid/substrate dissipation*.

In Part II, it has been demonstrated that PFEM3D is able to model droplet oscillations in zero-gravity with remarkable precision using [6] when the *small oscillation hypothesis* was satisfied (note that this hypothesis was necessary for the 2D Rayleigh model and is in no means a limitation of PFEM3D). Indeed, it has been proven that both the angular frequency and the damping ratio retrieved from the numerical data were in excellent agreement with their values predicted by [6], hence providing a good representation of the droplet oscillation behaviour, dictated by both the effects of viscosity and surface tension. Given the nature of the problem studied in this part of the work, *i.e.*, *droplet oscillations on a substrate*, these previous results yield encouraging prospects for the model that remains to be completed.

The following structure for this part is suggested. In a first instance, the problem under attack is described and the involved forces are presented. Then, the set of governing equations is reminded (namely, the Navier-Stokes equations) and an overview of the finite element (FE) implementation is provided. From there, the lacking terms in the FE formulation PFEM3D are identified. Afterwards, a section is dedicated to the description as well as the implementation of each one of these terms. From there, a verification of the completed numerical model using the work of Mahrous [9] is performed and the comparison between both models is discussed. Finally, on the hand of the obtained results, a conclusion is presented.

1 Introduction : problem description

Consider the following problem : a water droplet ($\rho = 10^3$ [kg/m^3], $\mu = 10^{-3}$ [Pa $\cdot$ s], $\gamma = 72.8 \times 10^{-3}$ [N/m]) of characteristic length ℓ [m], surrounded by a gas phase (air in this case) and described by the volume Ω is deposited on a substrate of arbitrary nature and submitted to gravity ($g \equiv ||\mathbf{g}|| = -9.81$ [m/s^2]). Initially, its shape, described by its boundary $\partial\Omega_0$, differs from its equilibrium shape, described by $\partial\Omega_{\text{eq}}$. To evolve from $\partial\Omega_0$ to $\partial\Omega_{\text{eq}}$, the droplet oscillates on the substrate due to the effects of gravity and surface tension. A visual representation of this problem is provided in Fig. III.1.

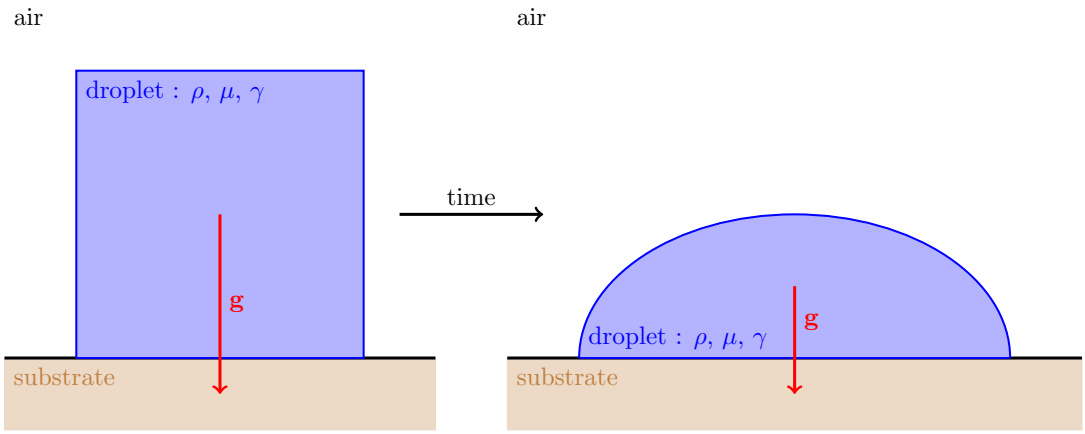

Figure III.1: A water droplet, deviated arbitrarily from its equilibrium configuration (left), deposited on a substrate will oscillate towards its equilibrium configuration over time (right).

The motors of these oscillations are both *surface tension* and *gravity*, and more precisely the *competition* between their associated forces. Indeed, while the effect of surface tension on the droplet is to minimize its free (surface) energy as reported in Part II, the effect of gravity is to pull the droplet mass downwards (*i.e.*, to flatten the droplet shape). This pulling down results, due to volume conservation, in an increased droplet free surface, which is counteracted by the effects of surface tension. In this sense, the droplet equilibrium configuration is dictated by an *equilibrium* between the forces resulting from surface tension and from gravitational pull.

2 Governing equations and an overview of the FE implementation of `PFEM3D`

2.1 Governing equations

The equations governing fluid dynamics behaviour are the Navier-Stokes equations. Consider a fluid volume Ω (a water droplet in the context of the current framework) that is Newtonian and incompressible. Consider also an isothermal regime with no phase transformation. In the Lagrangian formulation, these equations are written as Eq. II.2, where the RHS is no longer equal to zero, but rather to a net body force denoted $\mathbf{b}$ [N/kg] :

$$\begin{cases} \rho \dfrac{\mathrm{d}\mathbf{v}}{\mathrm{d}t} - \nabla \cdot \boldsymbol{\sigma} = \rho \mathbf{b} \,; \\ \nabla \cdot \mathbf{v} = 0, \end{cases} \tag{III.1}$$

given the framework of the current problem. The expression of the Cauchy stress tensor $\boldsymbol{\sigma}$ is written as :

$$\boldsymbol{\sigma} = 2\mu \boldsymbol{D} - p\boldsymbol{I}, \tag{III.2}$$

and the strain rate tensor $\boldsymbol{D}$ as :

$$\boldsymbol{D} = \frac{1}{2}\left(\nabla \mathbf{v} + (\nabla \mathbf{v})^{\mathrm{T}}\right). \tag{III.3}$$

The well-posedness of the Navier-Stokes equations is guaranteed if an *ad hoc* initial condition (IC) is considered. In this case :

$$\mathbf{v}(\mathbf{X}, t = 0) = \mathbf{v}_0. \tag{III.4}$$

The following set of boundary conditions (BCs) is also considered (these boundaries are represented in Fig. III.2) :

$$\begin{cases} \boldsymbol{\sigma} \cdot \mathbf{n} = \mathbf{h}(\mathbf{x}, t) \text{ on } \Gamma_{\mathrm{L}} \, ; \\ \\ \mathbf{v} \cdot \mathbf{n} = 0 \text{ on } \Gamma_{\mathrm{FS}'} \, ; \end{cases} \qquad \partial\Omega = \Gamma_{\mathrm{L}} \cup \Gamma'_{\mathrm{FS}}. \tag{III.5}$$

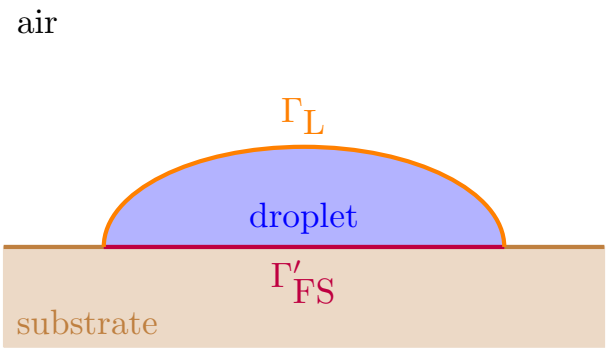

Figure III.2: Representation of the droplet boundaries. The droplet free surface is denoted Γ_{L} and the liquid-substrate interface is denoted Γ'_{FS}.

In Eqs. III.4 and III.5, the following quantities are defined :

- $\mathbf{X}$ [m] denotes the position-vector of any point in $\Omega(t = 0) \equiv \Omega_0$: $\mathbf{X}$ is the position-vector in the *reference configuration* Ω_0 ;
- $\mathbf{v}_0$ [m/s] denotes the initial velocity vector assigned to any point $\mathbf{X}$ in Ω_0, this value is *imposed* ;
- $\mathbf{n}$ [-] denotes the outward normal vector relative to the droplet boundary $\partial\Omega$ at any instant t in time ;
- $\mathbf{h}(\mathbf{x}, t)$ [Pa] denotes the set of surface forces to which any point of the droplet free surface Γ_{L} are subjected at any time t ;
- $\mathbf{x}$ [m] denotes the position-vector of any point in Ω : $\mathbf{x}$ is the position-vector in the *current configuration* ;
- Γ_{L} denotes the boundary defined by the droplet free surface ;
- Γ'_{FS} denotes the boundary defined by the liquid-substrate interface.

2.2 An overview of the FE implementation of PFEM3D

Consider the set of equations Eqs. III.1 → III.5 described in the previous section. To obtain a FE formulation for this model, a *standard Galerkin approach* is used : let $\mathbf{w}$ be an arbitrary kinematically admissible (KA) test function, meaning $\mathbf{w}$ is continuous and satisfies the BCs Eq. III.5. Then, satisfying the differential governing equation is equivalent to satisfying the following integral equation[9] :

$$\int_\Omega \left(\rho\frac{\mathrm{d}\mathbf{v}}{\mathrm{d}t} - \nabla\cdot\boldsymbol{\sigma} - \rho\mathbf{b}\right)\cdot\mathbf{w}\,\mathrm{d}\Omega + \int_{\partial\Omega}(\boldsymbol{\sigma}\cdot\mathbf{n} - \mathbf{h})\cdot\mathbf{w}\,\mathrm{d}\partial\Omega = 0, \tag{III.6}$$

which is obtained by multiplying both the momentum equation and the boundary conditions by $\mathbf{w}$ and integrating over the fluid volume Ω for the momentum equation, and over the fluid surface $\partial\Omega$ for the BCs. To develop this equation Eq. III.6 further, only the term which integrates $-(\nabla\cdot\boldsymbol{\sigma})\cdot\mathbf{w}$ over the fluid volume is considered in a first instance :

$$-\int_\Omega(\nabla\cdot\boldsymbol{\sigma})\cdot\mathbf{w}\,\mathrm{d}\Omega. \tag{III.7}$$

The Cauchy stress tensor σ is substituted by its expression Eq. III.2 and the divergence theorem is used to obtain :

$$\begin{aligned}-\int_\Omega(\nabla\cdot\boldsymbol{\sigma})\cdot\mathbf{w}\,\mathrm{d}\Omega &= \int_\Omega p\nabla\cdot\mathbf{w}\,\mathrm{d}\Omega \\ &\quad - \int_\Omega 2\mu\nabla\mathbf{w} : \boldsymbol{D}\,\mathrm{d}\Omega - \int_{\partial\Omega}(\boldsymbol{\sigma}\cdot\mathbf{n})\cdot\mathbf{w}\,\mathrm{d}\partial\Omega.\end{aligned} \tag{III.8}$$

This expression is then substituted back into Eq. III.6 and the third term in the RHS of Eq. III.8 cancels with the second term in the left-hand side (LHS) of Eq. III.6 :

$$\begin{aligned}&\int_{\Omega(t)}\rho\frac{\partial\mathbf{v}}{\partial t}\cdot\mathbf{w}\,\mathrm{d}\Omega(t) + \int_{\Omega(t)}p\nabla\cdot\mathbf{w}\,\mathrm{d}\Omega(t) - \int_{\Omega(t)}2\mu\nabla\mathbf{w} : \boldsymbol{D}\,\mathrm{d}\Omega(t) \\ &- \int_{\Omega(t)}\rho\mathbf{b}\cdot\mathbf{w}\,\mathrm{d}\Omega(t) - \int_{\partial\Omega(t)}\mathbf{h}\cdot\mathbf{w}\,\mathrm{d}\partial\Omega(t) = 0.\end{aligned} \tag{III.9}$$

The Galerkin formulation being completed, from there, a FE formulation is obtained by introducing a *space discretization*. The PFEM3D computer code uses, as most PFEM computer codes, *linear isoparametric elements*, which means that the velocity and pressure unknowns, resp. $\mathbf{v}$ and p, are re-written in their *discretized* form as follows :

$$\begin{cases}\mathbf{v} = \boldsymbol{N}_v^{\mathrm{T}}\bar{\mathbf{v}}\,; \\ \\ p = \boldsymbol{N}_p^{\mathrm{T}}\bar{p},\end{cases} \tag{III.10}$$

where $\boldsymbol{N}_v$ denotes the matrix of shape functions for the velocity $\mathbf{v}$, $\bar{\mathbf{v}}$ denotes the *nodal* values of the velocity unknown[10], $\boldsymbol{N}_p$ denotes the matrix of shape functions for the pressure

[9] This result is supported by the fundamental lemma of the calculus of variations.

[10] Recall that in the PFEM, the unknowns are stored at the mesh *nodes*, in contrast with *e.g.* a classical FEM code, in which case the unknowns are stored at the *Gauss points*.

p and $\bar{p}$ denotes the *nodal* values for the pressure unknown. The arbitrary test function is also discretized in this manner, *i.e.*, $\mathbf{w} = \boldsymbol{N}_v^{\mathrm{T}}\bar{\mathbf{w}}$. After substitution of these expressions in Eq. III.9, the following semi-discrete (because no time discretization is introduced yet) FE matrix formulation is obtained [11] :

$$\boldsymbol{M}\frac{\mathrm{d}\bar{\mathbf{v}}}{\mathrm{d}t} = -\boldsymbol{K}\bar{\mathbf{v}} + \boldsymbol{G}^{\mathrm{T}}\bar{p} + \mathbf{F}_{\mathrm{ext}}, \tag{III.11}$$

where $\boldsymbol{M}$ is the *mass matrix*, $\boldsymbol{K}$ is the *viscous matrix*, $\boldsymbol{G}$ is the *discrete gradient operator* and $\mathbf{F}_{\mathrm{ext}}$ is the *vector of applied forces*, expressed as :

$$\mathbf{F}_{\mathrm{ext}} = \int_{\Omega} \rho \boldsymbol{N}_v^{\mathrm{T}}\mathbf{b}\,\mathrm{d}\Omega + \int_{\partial\Omega} \boldsymbol{N}_v^{\mathrm{T}}\mathbf{h}\,\mathrm{d}\partial\Omega. \tag{III.12}$$

In Eq. III.12, the first term in the RHS represents the set of applied body forces and the second term in the RHS represents the *surface forces*. When linear isoparametric elements are introduced in Eq. III.9, $\mathbf{w}$ decomposes in $\mathbf{w} = \boldsymbol{N}_v^{\mathrm{T}}\bar{\mathbf{w}}$ such that $\bar{\mathbf{w}}$ can exit the integral, given it is an arbitrary function per definition. Since $\mathbf{w}$ appears in each integral, $\bar{\mathbf{w}}$ can exit each integral and be cancelled out because the RSH of the integral equation Eq. III.9 is equal to zero, which is why it does not appear in Eq. III.12.

The extension of the `PFEM3D` computer code (to be able to model liquid/substrate interaction phenomena such as described hereabove) relies on adding a set of terms to the surface forces integral. In the following section, this term will be developed further and will reveal which force contributions are already taken into account by `PFEM3D` per default. Then, the methodology from [9] will be presented and applied for the extension of `PFEM3D`. More precisely, the set of lacking contributions is obtained.

3 The surface forces term

The term of interest in Eq. III.12 is :

$$\int_{\partial\Omega} \boldsymbol{N}_v^{\mathrm{T}}\mathbf{h}\,\mathrm{d}\partial\Omega \equiv \mathbf{F}_{\mathrm{ext}}^{\partial\Omega}, \tag{III.13}$$

where the superscript $\partial\Omega$ is used to clarify that the set of external forces that act on the fluid boundary are considered. The explicit expression of $\mathbf{h}(\mathbf{x}, t)$ is :

$$\mathbf{h}(\mathbf{x}, t) = -\gamma\kappa\mathbf{n} \text{ at } \Gamma_{\mathrm{L}}, \tag{III.14}$$

in accordance with the BC Eq. III.4, where κ [m^{-1}] is the droplet curvature at any point of Γ_{L}. Therefore, an equivalent way of writing Eq. III.13 is (the linear isoparametric space discretization Eq. III.10 is dropped) :

$$\int_{\partial\Omega} \mathbf{h}\cdot\mathbf{w}\,\mathrm{d}\partial\Omega = -\int_{\Gamma_{\mathrm{L}}} \gamma\kappa\mathbf{n}\cdot\mathbf{w}\,\mathrm{d}\Gamma_{\mathrm{L}}. \tag{III.15}$$

To further develop this expression, the approach from Jarauta [10] is considered. The identity map $\boldsymbol{P}(\mathbf{x}) = \mathbf{x}$, $\forall\mathbf{x} \in \Gamma_{\mathrm{L}}$ on an arbitrary surface Γ_{L} (the droplet free surface in this case) is defined and has the following properties :

$$\begin{cases} \nabla_s \boldsymbol{P} = \boldsymbol{I} - \mathbf{n} \otimes \mathbf{n} \, ; \\ \Delta_s \boldsymbol{P} = \nabla_s \cdot (\nabla_s \boldsymbol{P}) = -\nabla_s \cdot (\mathbf{n} \otimes \mathbf{n}) = \kappa \mathbf{n}, \end{cases} \tag{III.16}$$

∇_s being the *surface gradient operator* and Δ_s being the *Laplace-Beltrami* operator. The last property from Eq. III.16 is then substituted into Eq. III.15 and the following expression is obtained :

$$-\int_{\Gamma_\mathrm{L}} \gamma \kappa \mathbf{n} \cdot \mathbf{w} \, \mathrm{d}\Gamma_\mathrm{L} = -\int_{\Gamma_\mathrm{L}} \gamma (\Delta_s \boldsymbol{P}) \cdot \mathbf{w} \, \mathrm{d}\Gamma_L. \tag{III.17}$$

After integration by parts as well as applying the surface divergence theorem, the following result can be retrieved :

$$-\int_{\Gamma_\mathrm{L}} \gamma (\Delta_s \boldsymbol{P}) \cdot \mathbf{w} \, \mathrm{d}\Gamma_\mathrm{L} = \int_{\Gamma_\mathrm{L}} \gamma (\nabla_s \boldsymbol{P}) \cdot \nabla \mathbf{w} \, \mathrm{d}\Gamma_L - \int_{\partial\Gamma_\mathrm{L} \equiv \partial\Gamma} \gamma \mathbf{m} \cdot \mathbf{w} \, \mathrm{d}\partial\Gamma. \tag{III.18}$$

In the second term of the RHS, the vector $\mathbf{m}$ is defined as follows :

$$\mathbf{m} = \mathbf{n} \times \mathrm{d}\mathbf{s}, \tag{III.19}$$

where $\mathrm{d}\mathbf{s}$ is the vector tangent to $\partial\Gamma_\mathrm{L} \equiv \partial\Gamma$ as presented in Fig. III.3, and $\partial\Gamma$ is the *contact line*, defined as $\partial\Gamma = \Gamma'_\mathrm{FS} \cap \Gamma_\mathrm{L}$ (red dots in Fig. III.3).

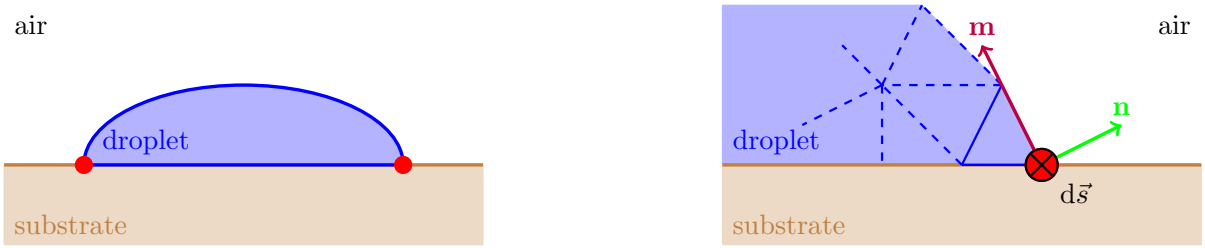

Figure III.3: Representation of the boundary $\partial\Gamma_\mathrm{L} \equiv \partial\Gamma$ (red dots) and its tangent vector $\mathrm{d}\mathbf{s}$ (noted $\mathrm{d}\vec{s}$ in the figure) as well as the vector $\mathbf{m}$. The figure on the right is a zoom on the right side of the droplet.

Following Eq. III.19, the vector $\mathbf{m}$ is defined as the vector tangent to the droplet free surface Γ_L at $\partial\Gamma$, as visualized in Fig. III.3.

In the `PFEM3D` computer code, the second term of the RHS in Eq. III.18 is previously neglected, which means that :

$$\mathbf{F}_\mathrm{ext}^{\partial\Omega} = \int_{\partial\Omega} \mathbf{h} \cdot \mathbf{w} \, \mathrm{d}\partial\Omega = \int_{\Gamma_\mathrm{L}} \gamma (\nabla_\mathrm{s} \boldsymbol{P}) \cdot \nabla \mathbf{w} \, \mathrm{d}\Gamma_\mathrm{L}. \tag{III.20}$$

For the applications in this work that are considered down the road, this term cannot be neglected, given the vector $\mathbf{m}$ in particular holds crucial information on the value of the *contact angle* θ [deg]. This value is measured as shown in Fig. III.4.

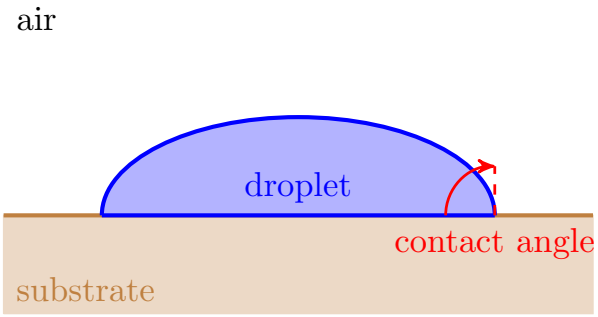

Figure III.4: Representation of how the contact angle is measured at the liquid/substrate interface.

3.1 Which contributions are lacking to the surface forces term $\mathbf{F}_{\mathbf{ext}}^{\partial\Omega}$?

It is revealed in the previous section that the second term in the RHS of Eq. III.18 is lacking in the FE formulation of `PFEM3D`. In further stages of this work, this term will be called the *surface tension force*. In addition to this surface tension force, as suggested by Mahrous [9], another set of forces needs to be considered as well in the FE formulation because they take account of important liquid-substrate contact phenomena such as *friction* as well as the *capillary effect*. Concretely, the following approach is used to complete the `PFEM3D` computer code, which uses both the work of Jarauta [10] and the work of Mahrous [9] :

1. In a first instance, an additional BC is implemented in `PFEM3D`, which suggests *free-slip* at the liquid-substrate contact Γ'_{FS} ;
2. Then, the surface tension force is added to the computer code. This effect takes account of the force that is generated by the contact angle at the contact line $\partial\Gamma$. For the implementation of this contribution in the FE model, the *implicit* approach suggested by the work of Jarauta [10] will be followed ;
3. Next, due to the non-physical nature of the free-slip boundary condition at Γ'_{FS}, the work of Mahrous [9] will be followed to implement the force that takes into account the friction that occurs in this region ;
4. Finally, it is also suggested by Mahrous [9] to add forces to the FE model that result from the *capillary effect at the contact line* as well as from the *normal stress jump at the contact line*.

Once the implementation of the full set of these additional forces is finished, the results provided in the work of Mahrous [9] will be used to compare the numerical data obtained by `PFEM3D` from. The `PFEM3D` computer model is then said to be complete if the obtained results are in agreement with the ones obtained in [9].

4 Adding the lacking forces to the FE formulation

4.1 Horizontal free slip BC at Γ'_{FS} and the surface tension force at $\partial\Gamma$

The surface tension force at the contact line $\partial\Gamma$ appears in Eq. III.18 as the second term of the RHS and is written :

$$-\int_{\partial\Gamma_L \equiv \partial\Gamma} \gamma \mathbf{m} \cdot \mathbf{w} \, \mathrm{d}\partial\Gamma. \tag{III.21}$$

Before developing this term to determine what expression needs to be implemented exactly in the FE formulation, it is suggested to define an additional boundary condition. The nature of this BC being *horizontal free slip*, it is considered that the velocity of the fluid particles at Γ'_{FS} is imposed to be equal to zero along the vertical coordinate, but to evolve *freely* (*i.e.*, without any restrictions *a priori*) along the horizontal coordinate. This condition can be expressed as follows :

$$\mathbf{v} \cdot \mathbf{n} = 0 \text{ on } \Gamma'_{FS}, \tag{III.22}$$

and states that no fluid can flow through the boundary Γ'_{FS}. The implementation of this BC constitutes the first contribution to the extension of `PFEM3D`.

With the HFS BC being added to the set of already pre-existing ones, the spotlight can be turned again onto the development of the surface tension force displayed in Eq. III.21. Before moving on, it is reminded in a first instance that the context of this work is two-dimensional, as mentioned numerous times beforehand. It is implied by this context that (a) the droplet volume is in fact a surface ; (b) the droplet surface is in fact a curve. Subsequently, the integral figuring in Eq. III.21 is zero-dimensional, meaning its value is equal to that of the integrand :

$$-\int_{\partial\Gamma} \gamma \mathbf{m} \cdot \mathbf{w} \, \mathrm{d}\partial\Gamma = -\gamma \mathbf{m} \cdot \mathbf{w}. \tag{III.23}$$

More specifically, this means that this equation needs to be evaluated at 2 points of the droplet surface $\partial\Omega$, « $\partial\Gamma^{\text{left}}$ » and « $\partial\Gamma^{\text{right}}$ », represented in Fig. III.5.

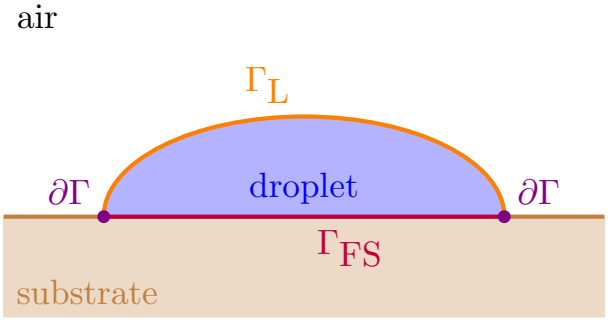

Figure III.5: Representation of the two points $\partial\Gamma$ at which the surface tension force needs to be evaluated. What has been denoted $\partial\Gamma^{\text{left}}$ hereabove is simply the node $\partial\Gamma$ on the left side of the droplet (equivalently, $\partial\Gamma^{\text{right}}$ is the node $\partial\Gamma$ on the right side of the droplet). In this figure, Γ_{FS} is defined as $\Gamma_{FS} = \Gamma'_{FS} \backslash \partial\Gamma$.

This expression can further be simplified by introducing a linear isoparametric space discretization (Eq. III.10) such that Eq. III.23 can be re-written as :

$$-\gamma \mathbf{m} \cdot \mathbf{w} = -\gamma \mathbf{m} \cdot (\boldsymbol{N}_v^{\mathrm{T}} \bar{\mathbf{w}}), \tag{III.24}$$

where $\boldsymbol{N}_v^{\mathrm{T}}$ is the shape function matrix for the velocity unknown. The value of $\boldsymbol{N}_v^{\mathrm{T}}$ being equal to 1 at $\partial\Gamma$ given the nature of the problem, Eq. III.24 can be re-written as :

$$-\gamma \mathbf{m} \cdot (\boldsymbol{N}_v^{\mathrm{T}} \bar{\mathbf{w}}) = -\gamma \mathbf{m} \cdot \bar{\mathbf{w}}. \tag{III.25}$$

Remembering that the test function $\mathbf{w}$ appears in front of each term of the integral equation Eq. III.9 and that the RHS equals to zero, $\bar{\mathbf{w}}$ can be simplified with the ones from the other terms in the formulation such that :

$$-\gamma \mathbf{m} \cdot \bar{\mathbf{w}} = -\gamma \mathbf{m}. \tag{III.26}$$

It is underlined that the simplicity of the solution is due to the two-dimensional nature of the problem. If the problem was three-dimensional instead, reducing the solution of the integral to the value of the integrand would not be possible.

4.2 Dissipation due to friction at Γ'_{FS}

The current state of the FE formulation in `PFEM3D` is given by Eq. III.11 :

$$\boldsymbol{M} \frac{\mathrm{d}\bar{\mathbf{v}}}{\mathrm{d}t} = -\boldsymbol{K}\bar{\mathbf{v}} + \boldsymbol{G}^{\mathrm{T}}\bar{p} + \mathbf{F}_{\mathrm{ext}}, \tag{III.27}$$

where $\mathbf{F}_{\mathrm{ext}}$ is the vector of external forces, previously defined as :

$$\mathbf{F}_{\mathrm{ext}} = \int_{\Omega} \rho \mathbf{b} \cdot \mathbf{w} \, \mathrm{d}\Omega + \int_{\partial\Omega} \mathbf{h} \cdot \mathbf{w} \, \mathrm{d}\partial\Omega, \tag{III.28}$$

and the second integral in the RHS of Eq. III.28 now includes the surface tension force at $\partial\Gamma$, such that it can be re-written as :

$$\int_{\partial\Omega} \mathbf{h} \cdot \mathbf{w} \, \mathrm{d}\partial\Omega = \int_{\Gamma_{\mathrm{L}}} \gamma(\nabla_{\mathrm{s}} \boldsymbol{P}) \cdot \nabla \mathbf{w} \, \mathrm{d}\Gamma_{\mathrm{L}} - \int_{\partial\Gamma} \gamma \mathbf{m} \cdot \mathbf{w} \, \mathrm{d}\partial\Gamma. \tag{III.29}$$

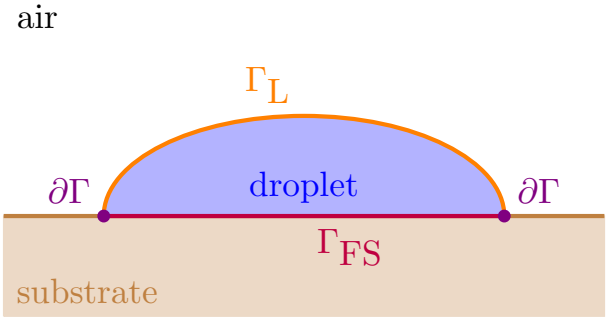

Figure III.6: Visualisation of the different droplet boundaries. The additional force that is tackled in this section, the dissipative force at the liquid-substrate contact, is added at Γ_{FS} and $\partial\Gamma$.

From there, the following step to complete the FE formulation is to include the *dissipative force* at the liquid-substrate interface Γ_{FS} as well as at $\partial\Gamma$ (*cf.* Fig. III.16), meaning that Eq. III.29 needs to be re-written as :

$$\int_{\partial\Omega} \mathbf{h}\cdot\mathbf{w}\,\mathrm{d}\partial\Omega = \int_{\Gamma_{\text{L}}} \gamma(\nabla_{\text{s}}\boldsymbol{P})\cdot\nabla\mathbf{w}\,\mathrm{d}\Gamma_{\text{L}} - \int_{\partial\Gamma}\gamma\mathbf{m}\cdot\mathbf{w}\,\mathrm{d}\partial\Gamma + \int_{\Gamma'_{\text{FS}}} (\text{dissip. force})\cdot\mathbf{w}\,\mathrm{d}\Gamma'_{\text{FS}}. \tag{III.30}$$

Following the work of Mahrous [9], the expression of this dissipative force is given by :

$$-\beta_s\mathbf{v}, \tag{III.31}$$

such that Eq. III.30 reads :

$$\int_{\partial\Omega} \mathbf{h}\cdot\mathbf{w}\,\mathrm{d}\partial\Omega = \int_{\Gamma_{\text{L}}} \gamma(\nabla_{\text{s}}\boldsymbol{P})\cdot\nabla\mathbf{w}\,\mathrm{d}\Gamma_{\text{L}} - \int_{\partial\Gamma}\gamma\mathbf{m}\cdot\mathbf{w}\,\mathrm{d}\partial\Gamma - \int_{\Gamma'_{\text{FS}}} \beta_s\mathbf{v}\cdot\mathbf{w}\,\mathrm{d}\Gamma'_{\text{FS}}. \tag{III.32}$$

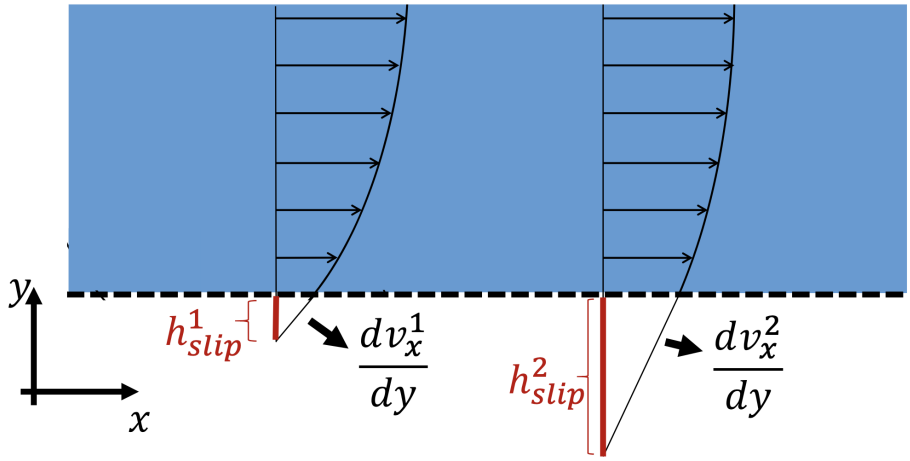

Figure III.7: Interpretation of the slip length h_{slip}. This figure is directly taken from the work of Meduri [11].

In Eqs. III.31 and III.32, β_s is expressed in [Pa · s/m] and referred to as the *Navier slip coefficient*. An interpretation of this coefficient is given in the work of Meduri [11] : let h_{slip} [m] be the *slip length*, defined as the distance from Γ'_{FS} to the point with zero tangential velocity, obtained with a linear extrapolation of the tangential velocity profile as shown in Fig. III.17. Then the Navier slip coefficient β_s is defined as :

$$\beta_s = \frac{\mu}{h_{\text{slip}}}. \tag{III.33}$$

When $h_{\text{slip}} \to \infty$, $\beta_s = 0$ and the previously implemented HFS BC is recovered. In contrast, when $h_{\text{slip}} = 0$, $\beta_s \to \infty$ and a no-slip BC is recovered.

In theory, the value of the slip length h_{slip} is of the order of 10 atomic lengths, *i.e.*, $h_{\text{slip}} \sim 10^{-9}$ [m]. In practice, however, setting h_{slip} to this theoretical value would mean that the scale of the characteristic element size near Γ'_{FS} should be set to this same value in order to capture the physics correctly. As previously discussed in this work, decreasing

the value of $h(d)$ is very expensive in terms of the CPU-time, such that setting $h(d) \sim 10^{-9}$ [m] is not a reasonable option.

A multitude of models exist in the literature on the computation of the slip length h_{slip} for numerical purposes. For instance, Cremonesi [12] suggests that the value of h_{slip} should depend on the characteristic mesh size $h(d)$, while Venkatesan [13] proposes a model for h_{slip} that depends on both the Reynolds number and the Weber number. In this work, the approach of Cremonesi [12] is followed.

Introducing linear isoparametric elements and using the expression of the velocity and pressure unknowns Eq. III.10, the of the dissipative force to be added in `PFEM3D` can be re-written as :

$$-\int_{\Gamma'_{\text{FS}}} \beta_s \mathbf{v} \cdot \mathbf{w} \, \mathrm{d}\Gamma'_{\text{FS}} = -\int_{\Gamma'_{\text{FS}}} \beta_s \boldsymbol{N}_v^{\mathrm{T}} \boldsymbol{N}_v \bar{\mathbf{v}} \, \mathrm{d}\Gamma'_{\text{FS}}, \tag{III.34}$$

where $\bar{\mathbf{w}}$ cancels out.

4.3 More forces at the contact line $\partial\Gamma$

In addition to the surface tension force at $\partial\Gamma$ as well as the dissipative force at Γ'_{FS}, Mahrous [9] suggests in his work to finally add two other forces at $\partial\Gamma$: (a) a force related to the *capillary effect* and (b) a force related to the *normal stress jump at* $\partial\Gamma$ (this effect becomes larger when the velocity at the contact line increases) :

$$\text{additional forces at contact line } \partial\Gamma = -\zeta \mathbf{v} - \beta_n \mathbf{v}, \tag{III.35}$$

where ζ [Pa · s/m] is the coefficient related to the capillary effect and β_n [Pa · s/m] is the coefficient related to the normal stress jump. The expression of ζ is given as follows :

$$\zeta = \frac{\gamma}{u} R(\text{Ca}), \tag{III.36}$$

and that of β_n as :

$$\beta_n = \frac{1}{u} \mu \nabla(\mathbf{v} \cdot \mathbf{t}) \cdot \mathbf{t}. \tag{III.37}$$

In both equations, u [m/s] denotes the horizontal velocity component at $\partial\Gamma$, *i.e.*, $u = \mathbf{v} \cdot \mathbf{t}$, where $\mathbf{t}$ [-] denotes the vector that is tangent to Γ_{FS} at $\partial\Gamma$. The notation $R(\text{Ca})$ in Eq. III.37 suggests that the coefficient related to the capillary force can be expressed as a function of the *capillary number* Ca [-], defined as :

$$\text{Ca} = \frac{u\mu}{\gamma}, \tag{III.38}$$

In the work of Mahrous [9], the model that is suggested for the expression of $R(\text{Ca})$ is Jiang's expression [14], which considers that the velocity at the contact line for capillary-driven droplet spreading is of the order of the impact velocity for a droplet :

$$R(\text{Ca}) = (\cos\theta_s + 1) \tanh\left(4.96 \text{Ca}^{0.702}\right), \tag{III.39}$$

such that Eq. III.37 is re-written as :

$$\zeta = \frac{\gamma}{u}(\cos\theta_s + 1)\tanh\left(4.96\mathrm{Ca}^{0.702}\right). \tag{III.40}$$

In Eqs. III.39 and III.40, θ_s [deg] denotes the *static contact angle*, *i.e.* the contact angle at $\partial\Gamma$ once the droplet has attained its equilibrium configuration $\partial\Omega_{\text{eq}}$. The expression of the surface force Eq. III.30 now reads, with the addition of these forces :

$$\int_{\partial\Omega} \mathbf{h}\cdot\mathbf{w}\,\mathrm{d}\partial\Omega = \int_{\Gamma_{\mathrm{L}}} \gamma(\nabla_s \boldsymbol{P})\cdot\nabla\mathbf{w}\,\mathrm{d}\Gamma_{\mathrm{L}} - \int_{\partial\Gamma}\gamma\mathbf{m}\cdot\mathbf{w}\,\mathrm{d}\partial\Gamma - \int_{\Gamma'_{\mathrm{FS}}}\beta_s\mathbf{v}\cdot\mathbf{w}\,\mathrm{d}\Gamma'_{\mathrm{FS}}$$
$$- \int_{\partial\Gamma}\zeta\mathbf{v}\cdot\mathbf{w}\,\mathrm{d}\partial\Gamma - \int_{\partial\Gamma}\beta_n\mathbf{v}\cdot\mathbf{w}\,\mathrm{d}\partial\Gamma. \tag{III.41}$$

Introducing linear isoparametric elements, noting that the integral on $\partial\Gamma$ is zero-dimensional and that the test function $\mathbf{w}$ simplifies with the other ones, the expression of the terms to add to the FE formulation is given by :

$$-\zeta\bar{\mathbf{v}} - \beta_n\bar{\mathbf{v}}. \tag{III.42}$$

4.4 Summary

Below, a summary of the steps suggested by [9] and [10] is given.

Summary on the completion of the FE formulation.

1. An additional BC needs to be implemented : the horizontal free slip (HFS) BC. Then, the contribution of the surface tension force at $\partial\Gamma$ to the Galerkin formulation Eq. III.20 reads [10] :

$$\int_{\partial\Omega} \mathbf{h}\cdot\mathbf{w}\,\mathrm{d}\partial\Omega = \int_{\Gamma_{\mathrm{L}}} \gamma(\nabla_s \boldsymbol{P})\cdot\nabla\mathbf{w}\,\mathrm{d}\Gamma_{\mathrm{L}} - \int_{\partial\Gamma}\gamma\mathbf{m}\cdot\mathbf{w}\,\mathrm{d}\partial\Gamma\,; \tag{III.43}$$

2. The second contribution is related to the viscous dissipation at the liquid-substrate interface Γ_{FS} as well as at the contact line $\partial\Gamma$. The expression of Eq. III.20 then becomes [9] (denote $\Gamma'_{\mathrm{FS}} \equiv \Gamma_{\mathrm{FS}} \cup \partial\Gamma$ to alleviate notations) :

$$\int_{\partial\Omega} \mathbf{h}\cdot\mathbf{w}\,\mathrm{d}\partial\Omega = \int_{\Gamma_{\mathrm{L}}} \gamma(\nabla_s \boldsymbol{P})\cdot\nabla\mathbf{w}\,\mathrm{d}\Gamma_{\mathrm{L}} - \int_{\partial\Gamma}\gamma\mathbf{m}\cdot\mathbf{w}\,\mathrm{d}\partial\Gamma - \int_{\Gamma'_{\mathrm{FS}}}\beta_s\mathbf{v}\cdot\mathbf{w}\,\mathrm{d}\Gamma'_{\mathrm{FS}}\,; \tag{III.44}$$

3. Finally, a force related to the capillary effect at $\partial\Gamma$ as well as another force, related to the normal stress jump at $\partial\Gamma$, also need to be added to Eq. III.20 :

$$\int_{\partial\Omega} \mathbf{h}\cdot\mathbf{w}\,\mathrm{d}\partial\Omega = \int_{\Gamma_{\mathrm{L}}} \gamma(\nabla_s \boldsymbol{P})\cdot\nabla\mathbf{w}\,\mathrm{d}\Gamma_{\mathrm{L}} - \int_{\partial\Gamma}\gamma\mathbf{m}\cdot\mathbf{w}\,\mathrm{d}\partial\Gamma - \int_{\Gamma'_{\mathrm{FS}}}\beta_s\mathbf{v}\cdot\mathbf{w}\,\mathrm{d}\Gamma'_{\mathrm{FS}}$$
$$- \int_{\partial\Gamma}\zeta\mathbf{v}\cdot\mathbf{w}\,\mathrm{d}\partial\Gamma - \int_{\partial\Gamma}\beta_n\mathbf{v}\cdot\mathbf{w}\,\mathrm{d}\partial\Gamma. \tag{III.45}$$

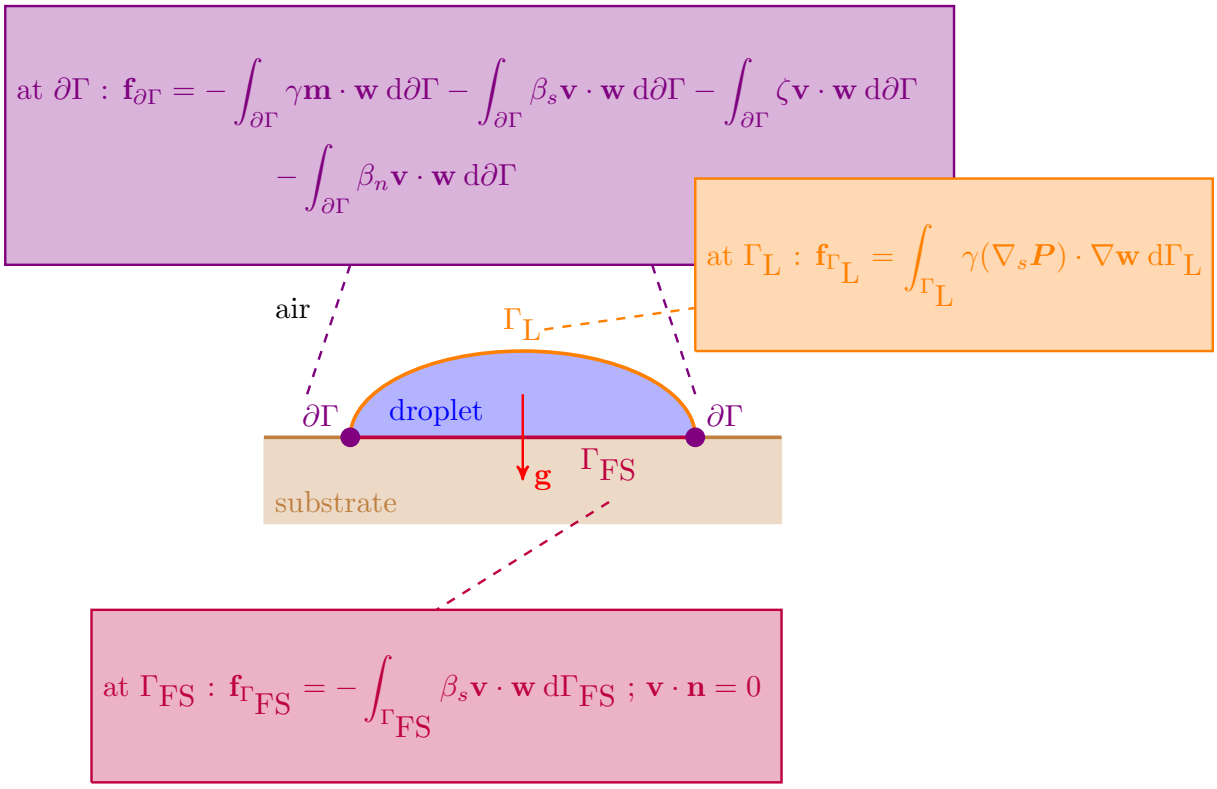

Figure III.8: Representation of where the supplementary forces described above act on the droplet boundaries.

5 Validation of the numerical model

5.1 Implementation of the initial geometry

For the validation of the numerical model, the simulation results obtained by `PFEM3D` will be compared to the ones presented in [9]. The following problem is considered : a water droplet ($\rho = 10^3$ [kg/m^3], $\mu = 8.9 \times 10^{-4}$ [Pa $\cdot$ s], $\gamma = 72 \times 10^{-3}$ [N/m]) is initially semi-circle-shaped, deposited on a substrate of arbitrary nature and submitted to gravity (Fig. III.9). The radius is denoted R and is set to a value of 1.25×10^{-4} [m].

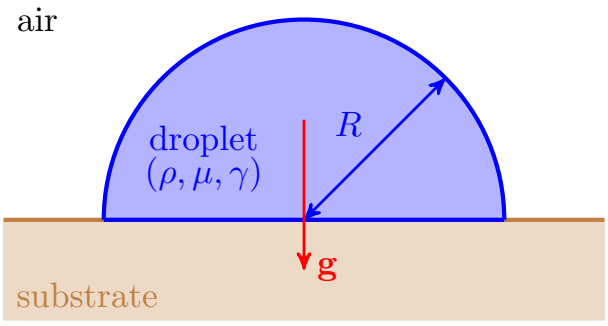

Figure III.9: Initial configuration of the water droplet on a substrate. In [9], the value of the radius is set to 1.25×10^{-4} [m].

Initially, the contact angle θ is 90 [deg] and its equilibrium value θ_s is set to 45 [deg].

5.2 Numerical parameters

The list of numerical parameters suggested by Mahrous [9] is given below :

- characteristic element size (uniform mesh, Fig. III.10) :
  - $h = 1.25 \times 10^{-5}$ [m] (340 elements in [9], 446 elements using `Gmsh`) ;
  - $h = 9.6 \times 10^{-6}$ [m] (598 elements in [9], 736 elements using `Gmsh`) ;
  - $h = 6.8 \times 10^{-6}$ [m] (1,205 elements in [9], 1,368 elements using `Gmsh`) ;
  - $h = 5 \times 10^{-6}$ [m] (2,206 elements in [9], 2,472 elements using `Gmsh`) ;
- Time-step $\Delta t = 2 \times 10^{-7}$ [s] ;
- Simulation time $\mathcal{T} = 4 \times 10^{-3}$ [s] ;
- Equilibrium contact angle : $\theta_s = 45$ [deg].

Only the value for the characteristic element size h varies for the study of the numerical convergence, while Δt is set to be constant for the entirety of the simulation cases that will follow.

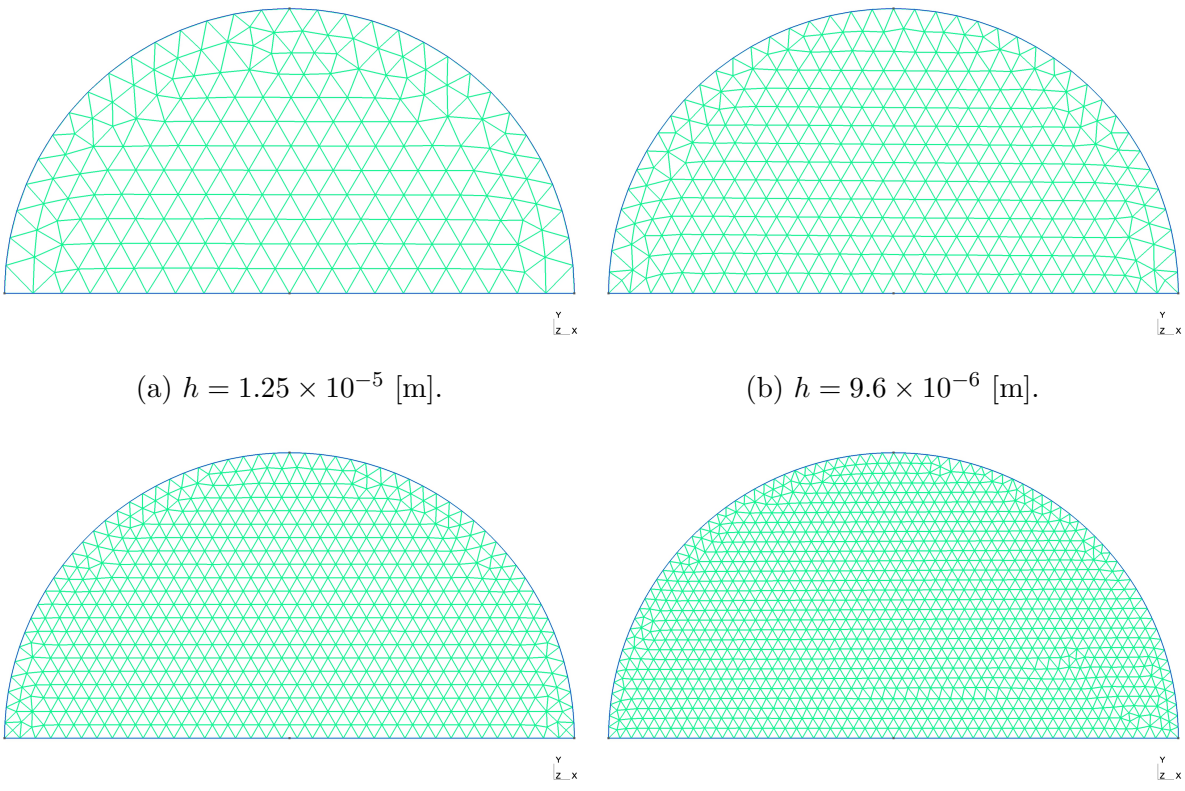

(a) $h = 1.25 \times 10^{-5}$ [m].

(b) $h = 9.6 \times 10^{-6}$ [m].

(c) $h = 6.8 \times 10^{-6}$ [m].

(d) $h = 5 \times 10^{-6}$ [m].

Figure III.10: Representation of the different meshes.

5.3 Validation of the numerical model

To validate the numerical model, the following structure for this section is suggested (following the structure of [9]) :

1. The convergence of the numerical solution as a function of the characteristic element size d (among the values given hereabove) is studied, without implementing any additional force described except for the surface tension force Eq. III.21 ;
2. The behaviour of the numerical solution by including progressively the entire set of additional forces (Eqs. III.26, III.29 and III.41) is examined ;
3. The change in behaviour of the numerical solution between the finest and the coarsest meshes (resp. $h = 5 \times 10^{-6}$ [m] and $h = 1.25 \times 10^{-5}$ [m]), with and without taking into account the entire set of additional forces, is finally studied.

The quantity that is used to study the behaviour of the numerical solution is the *spreading displacement*, noted r in [9] and defined as shown in Fig. III.11.

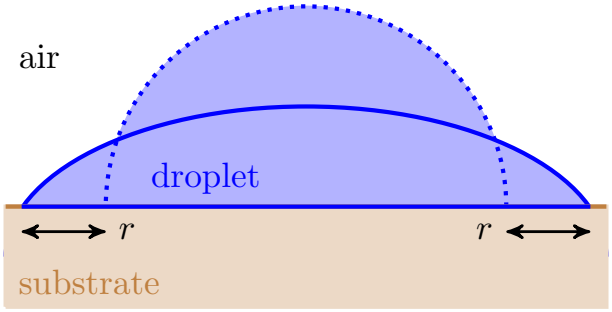

Figure III.11: Representation of how the spreading displacement is measured. The dotted configuration represents the shape of the droplet at the instant $t = 0$ [s], while the configuration drawn with a whole line represents its equilibrium shape.

Before moving on to the validation step : an important remark on the contact angle. For the purpose of this work, the implementation of the surface tension force at the contact line follows the work of Jarauta [10]. He suggests an *implicit treatment* of this force, which does not necessitate the value of the curvature of Γ_L at $\partial\Gamma$. Indeed, `PFEM3D` is unable to compute curvatures, which means that the « traditional » expression of this force, *i.e.*, $-\gamma\kappa\mathbf{n}$, where the curvature appears as κ, is not an option for implementation. Furthermore, `PFEM3D` does not use an energy minimization principle, which means that the well-known Young equation $\gamma_{lv}\cos\theta_s = \gamma_{sv} - \gamma_{sl}$ (γ_{lv} denotes the liquid-gas interface energy, γ_{sv} the solid-gas interface energy and γ_{sl} the liquid-substrate interface energy) can also not be implemented. Therefore, the expression for implicitly handling the surface tension force at $\partial\Gamma$ suggested by Jarauta [10] is ideal, in the sense that it only needs the vector $\mathrm{d}\mathbf{s}$ tangent to the contact line as well as the normal $\mathbf{n}$ to Γ_L at $\partial\Gamma$ as described by Eq. III.21 :

$$-\int_{\partial\Gamma} \gamma\mathbf{m}\cdot\mathbf{w}\,\mathrm{d}\partial\Gamma, \tag{III.46}$$

where $\mathbf{m} = \mathbf{n} \times \mathrm{d}\mathbf{s}$. However, in combination with the HFS BC, the equilibrium value of the contact angle is limited to 90 [deg] only (at least, without any additional forces). In other words, independently of the initial configuration of the droplet, its equilibrium shape will always have a contact angle of 90 [deg].

There is, however, a way of setting the contact angle to a value that differs from 90 [deg]. Indeed, if the value of θ must be set to *e.g.* 45 [deg], as described by the experimental setup detailed in [9], then by setting $\mathbf{m}$ to :

$$\mathbf{m} \equiv \begin{pmatrix} m_1 \\ m_2 \end{pmatrix} = \begin{pmatrix} \cos(45) \\ \sin(45) \end{pmatrix}, \tag{III.47}$$

as shown in Fig. III.12, the value of the contact angle is set to $\theta = 45$ [deg] for the entirety of the simulation, and the contribution of the surface tension force is constant over time.

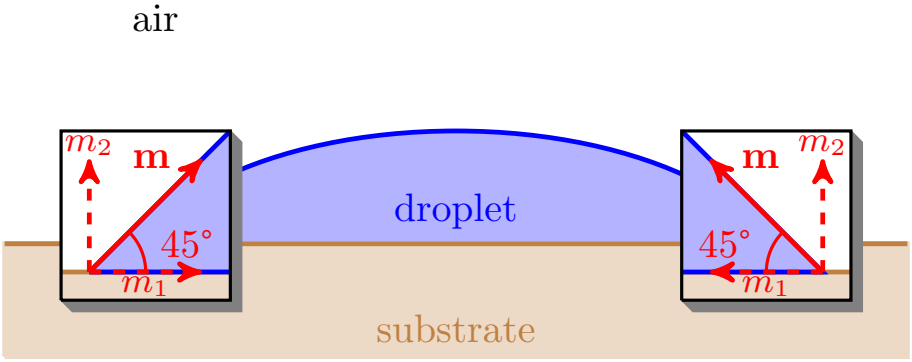

Figure III.12: Imposition of the value of the contact angle through the components of the vector $\mathbf{m}$.

While this is still not exactly the same study as described in [9], the results obtained by the two approaches should be very similar for as long as the contact angle modeled by [9] remains close to 45 [deg] over the simulation.

5.3.1 Mesh study

The first study that is performed is on the influence of the characteristic element size h on the numerical solution. No additional forces, except the surface tension force at the contact line in `PFEM3D`, are considered. Concretely, this means that neither friction at Γ'_{FS}, not the force resulting from the capillary effect at the contact line, nor the one resulting from the normal stress jump (also at the contact line) are taken into account. The different values for h to perform this study are recalled below :

- $h = 1.25 \times 10^{-5}$ [m] (223 nodes, 446 elements) ;
- $h = 9.6 \times 10^{-6}$ [m] (368 nodes, 736 elements) ;
- $h = 6.8 \times 10^{-6}$ [m] (684 nodes, 1,368 elements) ;
- $h = 5 \times 10^{-6}$ [m] (1,236 nodes, 2,472 elements).

It is also reminded that the value of the time-step Δt is set to 2×10^{-7} [s], that of the simulation time $\mathcal{T}$ to $\mathcal{T} = 4 \times 10^{-3}$ [s] and that of the equilibrium contact angle to $\theta_s = 45$ [deg]. In Fig. III.13, the simulation results using `PFEM3D` are presented. This graph is compared with the one from [9], displayed in Fig. III.14.

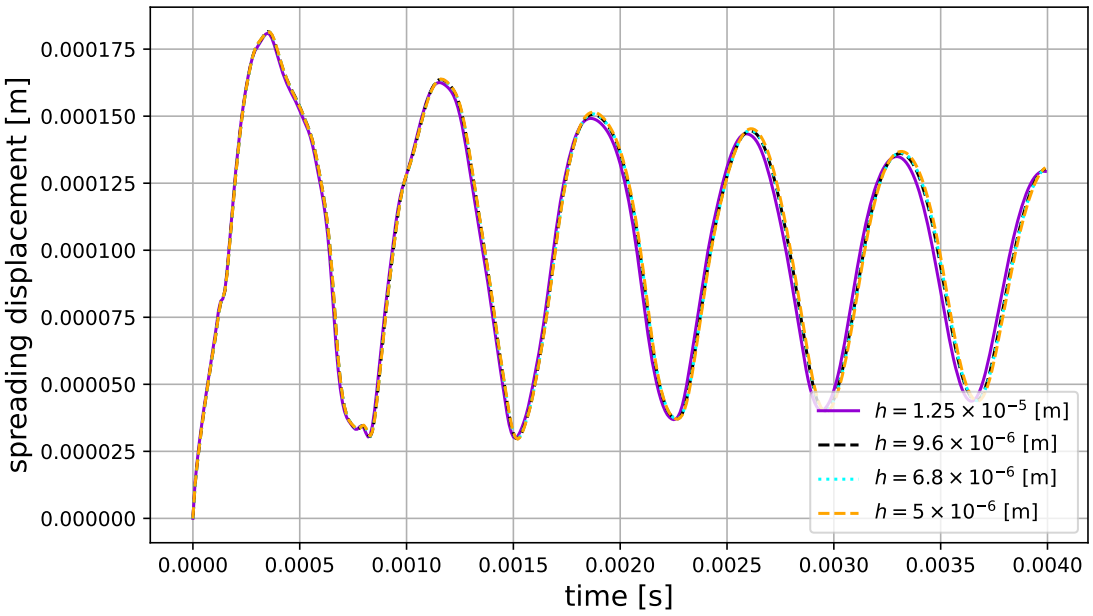

Figure III.13: Mesh dependence study of the numerical solution modeled by `PFEM3D`.

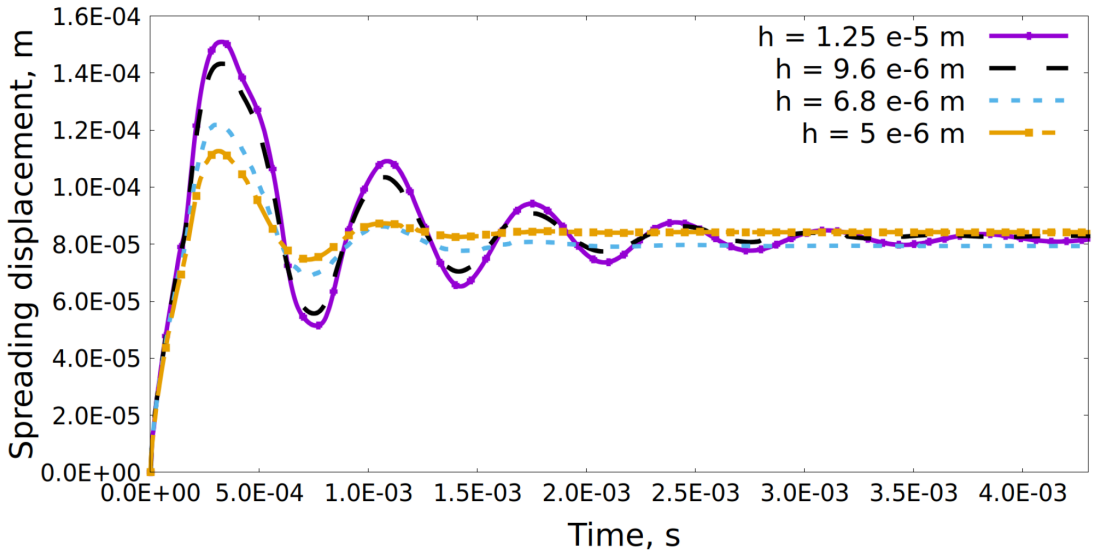

Figure III.14: Mesh dependence study of the numerical model [9].

In means to facilitate the comparison between the two models, the same colour code is used in their respective graphs. In contrast to [9] (Fig. III.14), the PFEM solution provided by `PFEM3D` (Fig. III.13) is almost mesh-independent, which means that numerical convergence of the solution is reached even for the coarse mesh $h = 1.25 \times 10^{-5}$ [m].

It is however noted that for the solution provided by [9], the behaviour of the spreading displacement stabilizes a lot faster for finer meshes, which is not observed in Fig. III.13. Furthermore, the damping rate modelled by [9] is very different from that modelled by `PFEM3D`. The reason for these differences could be that [9] does not use the implicit treatment for the surface tension force at the contact line $\partial\Gamma$, or even that the contact angle is allowed to take only this *precise* 45 [deg]-value for the *entire* simulation in this work.

Except for the increasing damping rate with mesh refinement reported in the results of [9], the overall shapes of the curves modelled by `PFEM3D` look very similar to the former. To support this statement, the measurements of the following quantities for the `PFEM3D` curve $h = 1.25 \times 10^{-5}$ [m] are considered :

- Oscillation frequency $f = 1,373$ [Hz] ;
- Overshoot $O = 1.8 \times 10^{-4}$ [m] ;
- Spreading displacement at equilibrium (the simulation time $\mathcal{T}$ is increased to 20×10^{-3} [s] such that spreading displacement equilibrium is almost reached, then the average of the spreading displacement is calculated) $= 8.23 \times 10^{-5}$ [m],

and compared to the ones *estimated* from the graphical data $h = 1.25 \times 10^{-5}$ [m] provided in [9] (estimated, because no exact numerical values for these quantities are given in the work of Mahrous [9]) :

- Oscillation frequency $f \simeq 1,470$ [Hz] ;
- Overshoot $O \simeq 1.5 \times 10^{-4}$ [m] ;
- Spreading displacement at equilibrium $= 8.16 \times 10^{-5}$ [m].

From there, the differences between the `PFEM3D` model and the model implemented in [9] in terms f, O and the spreading displacement at equilibrium are :

- $\Delta_f \simeq 6.59$ [%] ;
- $\Delta_O \simeq 20$ [%] ;
- $\Delta_{\text{spreading displacement at equilibrium}} \simeq 0.85$ [%].

While the results of the *dynamic* behaviour are quite different, the result on the behaviour at *equilibrium* is in excellent agreement with [9]. It is once more noted that the values of the spreading displacement provided by [9] are *estimated* from the graphical data Fig. III.14 (using the online software *PlotDigitizer* [15]), meaning this probably adds to the overall error that is observed. The obtained difference on the dynamic behaviour is majorly caused by the incorrectly modelled damping rate by `PFEM3D`.

Some simulation snapshots are presented in Fig. III.15 for the coarse mesh $h = 1.25 \times 10^{-5}$ [m]. On the CPU-times for the different mesh sizes, this varies from 12 minutes to almost 1.5 hours. The exact CPU-time values as a function of h are given in the table below.

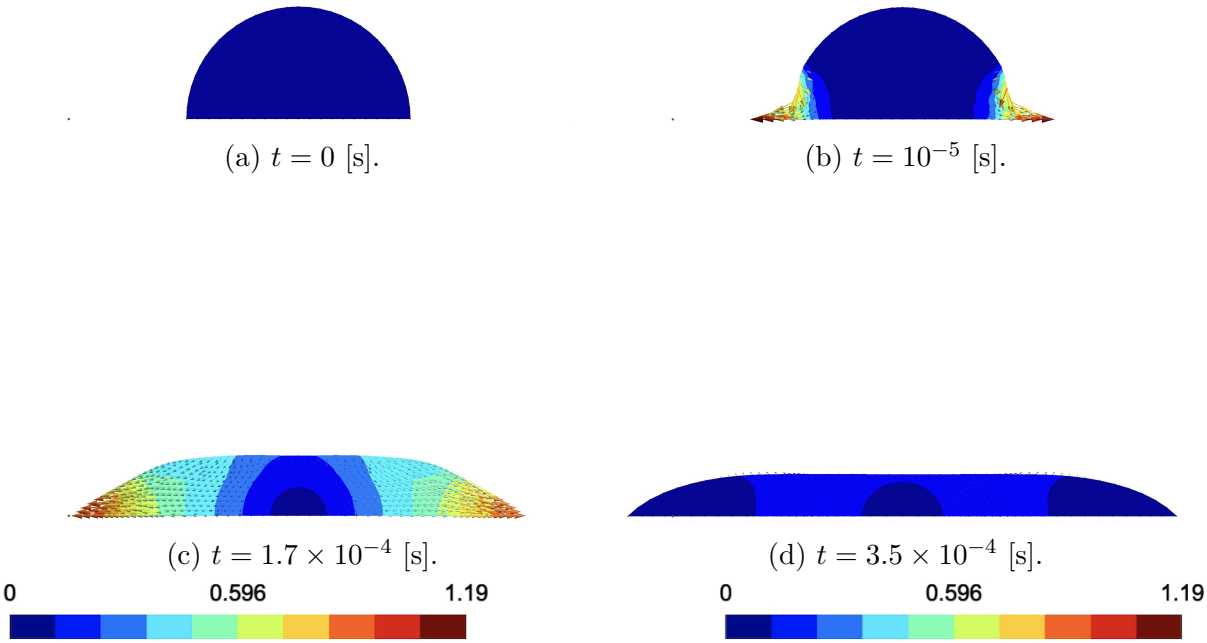

(a) $t = 0$ [s]. (b) $t = 10^{-5}$ [s].

(c) $t = 1.7 \times 10^{-4}$ [s]. (d) $t = 3.5 \times 10^{-4}$ [s].

Figure III.15: Snapshots of the droplet spreading problem without considering any additional forces at the contact line, nor at the liquid-substrate interface. The value of h is set to $h = 1.25 \times 10^{-5}$ [m] and that of the time-step to $\Delta t = 2 \times 10^{-7}$ [s]. The colour profile represents the magnitude of the velocity $||\mathbf{v}||$ and is measured in [m/s].

CPU-time as a function of h (4 threads, using `OpenMP` parallel computing).

- $h = 1.25 \times 10^{-5}$ [m] (223 nodes, 446 elements) : CPU-time $\simeq 780$ [s] ;
- $h = 9.6 \times 10^{-6}$ [m] (368 nodes, 736 elements) : CPU-time $\simeq 1,200$ [s] ;
- $h = 6.8 \times 10^{-6}$ [m] (684 nodes, 1,368 elements) : CPU-time $\simeq 2,350$ [s] ;
- $h = 5 \times 10^{-6}$ [m] (1,236 nodes, 2,472 elements) : CPU-time $\simeq 4,350$ [s].

5.3.2 Influence of the dissipative contribution at $\Gamma'_{\mathbf{FS}} \equiv \Gamma_{\mathbf{FS}} \cup \partial\Gamma$

The next case study suggested by [9] is that of the impact of the dissipation at the liquid-substrate interface as well as at the contact line $\partial\Gamma$ for various values of the Navier-slip coefficient β_s. Only the coarse mesh ($h = 1.25 \times 10^{-5}$ [m]) and the fine mesh ($h = 5 \times 10^{-6}$ [m]) are considered for this study. It is reminded that in this work, the Navier-slip coefficient is computed as a function of the slip-length h_{slip} :

$$\beta_s = \frac{\mu}{h_{\text{slip}}}, \tag{III.48}$$

where h_{slip} is computed itself as a function of the characteristic element size h, in accordance with the approach followed by Cremonesi [12]. Furthermore, in the PFEM formulation `PFEM3D`, the dissipation force is implemented at both the liquid-substrate interface and the contact line (this « combined » boundary has previously been denoted as $\Gamma'_{\text{FS}} \equiv \Gamma_{\text{FS}} \cup \partial\Gamma$) simultaneously, instead of [9] in which it is implemented at Γ_{FS} and at $\partial\Gamma$ separately. The reason for implementing the dissipative contribution this way is simply because it reduces the number of computations to be performed by the computer code, and hence decreases the CPU-time. Instead of Eq. III.47, Mahrous [9] uses another model for the Navier-slip coefficient :

$$\beta_s = \frac{1}{u}\mu\nabla(\mathbf{v}\cdot\mathbf{t})\cdot\mathbf{n}. \tag{III.49}$$

This more advanced (but complex) model takes account of the velocity gradients which tend to influence the value of the Navier-slip coefficient and is independent of the characteristic element size. A summary of the key differences between the approach used in this work and the one described in [9] is given below :

- Expression of the Navier-slip coefficient :
  - In this work : $\beta_s = \mu/h_{\text{slip}}$;
  - In [9] : $\beta_s = (1/u)\mu\nabla(\mathbf{v}\cdot\mathbf{t})\cdot\mathbf{n}$;
- Mesh-dependency :
  - In this work : yes ;
  - In [9] : no ;
- Computed at :
  - In this work : Γ_{FS} and $\partial\Gamma$ simultaneously ;
  - In [9] : Γ_{FS} and $\partial\Gamma$ separately.

While there are some differences between the approach described in this work and the one used in [9], the physical meaning of the additional term does not change and hence the same observations should appear when β_s is changed in a given manner. For the study of the influence of this parameter, the core is to increase the value of the Navier-slip coefficient to show that the droplet oscillations are more damped due to the effects of dissipation at $\Gamma'_{\text{FS}} \equiv \Gamma_{\text{FS}} \cup \partial\Gamma$. In accordance with the work of Cremonesi [12], the following values of β_s are suggested for the coarse mesh simulations (characteristic element size $h = 1.25 \times 10^{-5}$ [m]) :

- $\beta_s = 14.25$ [Pa · s/m], *i.e.*, the slip length is the characteristic element size multiplied by a factor 5 ;
- $\beta_s = 71.2$ [Pa · s/m], *i.e.*, the slip length is equal to the characteristic element size ;
- $\beta_s = 356$ [Pa · s/m], *i.e.*, the slip length is equal to the characteristic element size divided by a factor 5,

and the following for the fine mesh simulations ($h = 5 \times 10^{-6}$ [m]) :

- $\beta_s = 35.6$ [Pa · s/m], *i.e.*, the slip length is the characteristic element size multiplied by a factor 5 ;
- $\beta_s = 178$ [Pa · s/m], *i.e.*, the slip length is equal to the characteristic element size ;
- $\beta_s = 890$ [Pa · s/m], *i.e.*, the slip length is equal to the characteristic element size divided by a factor 5.

The results for these simulations are displayed in Fig. III.16. For both the coarse and the fine meshes, an increase of the value of the Navier slip coefficient β_s comes with an increase of the damping rate, because the effects of the viscous dissipation at $\Gamma'_{\text{FS}} \equiv \Gamma_{\text{FS}} \cup \partial\Gamma$ increase. Furthermore, still for both the coarse and the fine meshes, the spreading displacement at equilibrium tends towards the same value, independently on the value of β_s and independently on the value of h. For the other values mentioned in the previous study (that of the dependency of the solution on the characteristic element size), namely the droplet oscillation frequency and the overshoot, the following values are obtained :

- Coarse mesh ($h = 1.25 \times 10^{-5}$ [m]) :
  - $\beta_s = 0$ [Pa · s/m] : $f = 1,373$ [Hz], $O = 1.80 \times 10^{-4}$ [m] ;
  - $\beta_s = 14.25$ [Pa · s/m] : $f = 1,412$ [Hz], $O = 1.75 \times 10^{-4}$ [m] ;
  - $\beta_s = 71.2$ [Pa · s/m] : $f = 1,461$ [Hz], $O = 1.60 \times 10^{-4}$ [m] ;
  - $\beta_s = 356$ [Pa · s/m] : $f = 1,453$ [Hz], $O = 1.41 \times 10^{-4}$ [m] ;
- Fine mesh ($h = 5 \times 10^{-6}$ [m]) :
  - $\beta_s = 0$ [Pa · s/m] : $f = 1,366$ [Hz], $O = 1.81 \times 10^{-4}$ [m] ;
  - $\beta_s = 35.6$ [Pa · s/m] : $f = 1,436$ [Hz], $O = 1.69 \times 10^{-4}$ [m] ;
  - $\beta_s = 178$ [Pa · s/m] : $f = 1,457$ [Hz], $O = 1.53 \times 10^{-4}$ [m] ;
  - $\beta_s = 890$ [Pa · s/m] : $f = 1,436$ [Hz], $O = 1.39 \times 10^{-4}$ [m].

As the slip length h_{slip} decreases and the value of the Navier-slip coefficient β_s subsequently increases, the droplet spreading displacement frequency tends to increase and the overshoot, in the contrary, tends to decrease. This is observed both for the coarse mesh and the fine mesh. For the frequency, this behaviour is observed until the value of β_s corresponds to the case in which the slip length h_{slip} is set equal to the characteristic element size h, leading to $f \simeq 1,460$ [Hz]. If the value of β_s is increased further, or equivalently, if the value of h_{slip} is further decreased, f tends to decrease slightly. This shift in behaviour when the « limit case » $h_{\text{slip}} = h$ is reached is most probably explained by the fact that when $h_{\text{slip}} < h$, the FE mesh might be too coarse in order to precisely model the physical behaviour at $\Gamma'_{\text{FS}} \equiv \Gamma_{\text{FS}} \cup \partial\Gamma$. Whether this leads to nonphysical behaviour or not is discussed hereafter, for which Figs. III.17 and III.18 are introduced. These figures present simulation snapshots for different values of β_s at the same value of the simulation time in order to compare the extension of the boundary layer near $\Gamma'_{\text{FS}} \equiv \Gamma_{\text{FS}} \cup \partial\Gamma$. This

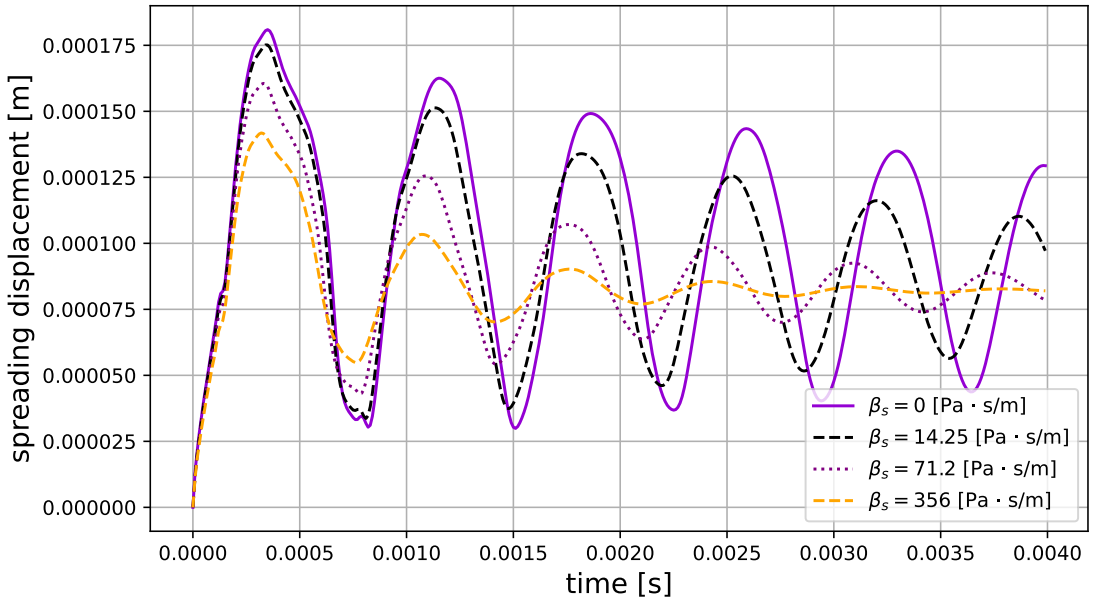

(a) $h = 1.25 \times 10^{-5}$ [m].

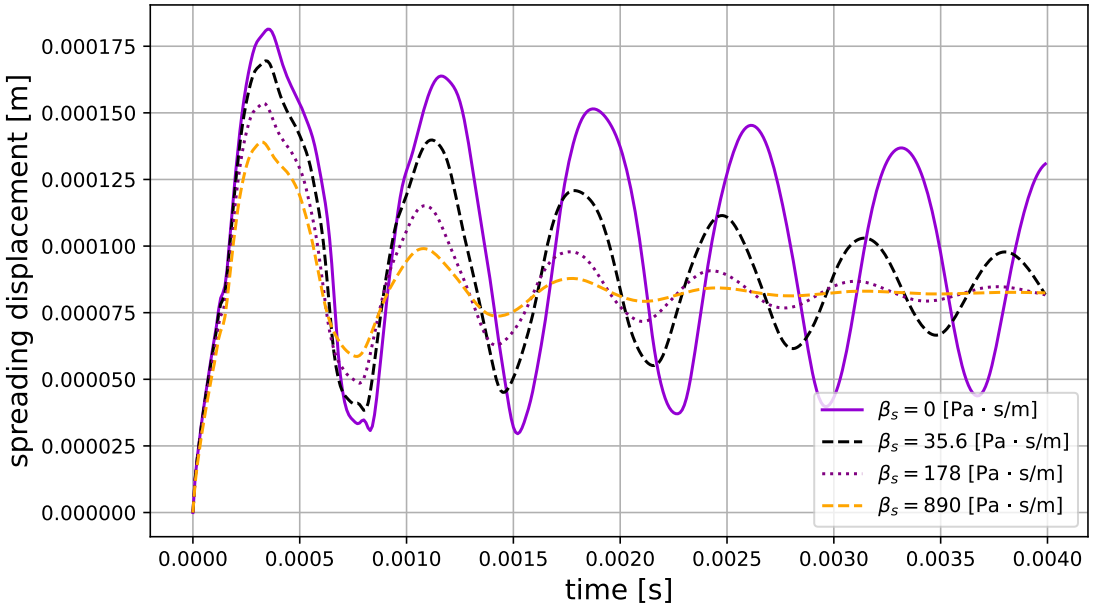

(b) $h = 5 \times 10^{-6}$ [m].

Figure III.16: Droplet spreading displacement as a function of the value of the Navier slip coefficient β_s. For both figures, the time-step Δt is set to $\Delta t = 2 \times 10^{-7}$ [s].

boundary layer appears when dissipation due to liquid-substrate friction, as well as at the contact line, is taken into account.

Both for the coarse mesh and the fine mesh simulations, increasing the value of the Navier-slip coefficient β_s results in an extension of the boundary layer near $\Gamma'_{\text{FS}} \equiv \Gamma_{\text{FS}} \cup \partial\Gamma$.

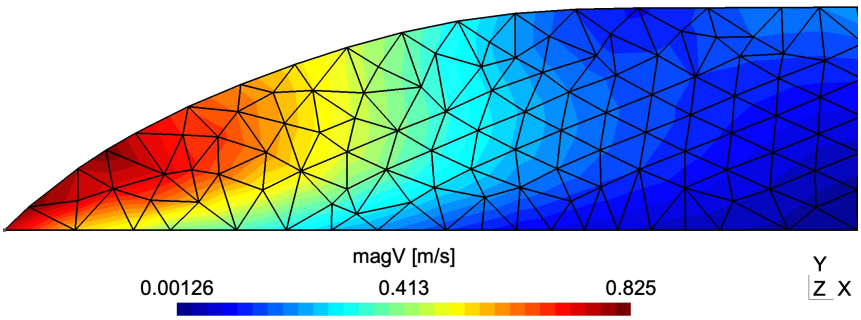

(a) $\beta_s = 71.2$ [Pa · s/m], $t = 2 \times 10^{-4}$ [s].

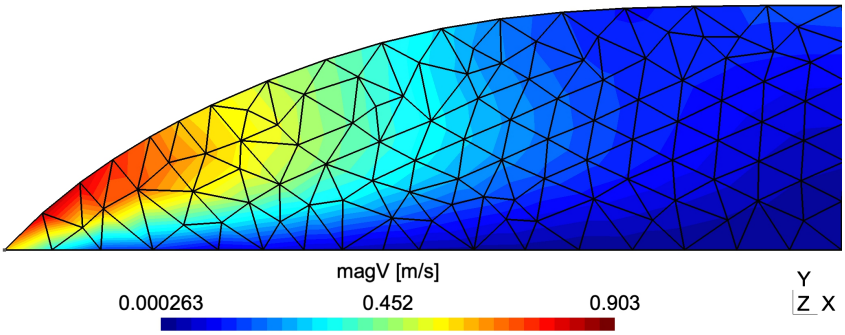

(b) $\beta_s = 356$ [Pa · s/m], $t = 2 \times 10^{-4}$ [s].

Figure III.17: Extension of the boundary layer for different values of the Navier-slip coefficient β_s. Here, a coarse mesh is used ($h = 1.25 \times 10^{-5}$ [m]) and the value of Δt remains $\Delta t = 2 \times 10^{-7}$ [s].

For the fine mesh ($h = 5 \times 10^{-6}$ [m]), this extension when $h_{\text{slip}} = h$ (Fig. III.17a) is initially more significant in comparison with the coarse mesh case which equally imposes $h_{\text{slip}} = h$ (Fig. III.18a). This indicates that when the dissipative force at $\Gamma'_{\text{FS}} \equiv \Gamma_{\text{FS}} \cup \partial\Gamma$ is considered, the numerical solution becomes mesh-dependent, in contrast with what has been observed in the previous section. This can easily be explained by reminding that the value of the Navier-slip coefficient is automatically computed as a function of h_{slip}, and thus of h, such that its value is greater for finer meshes in comparison with coarse

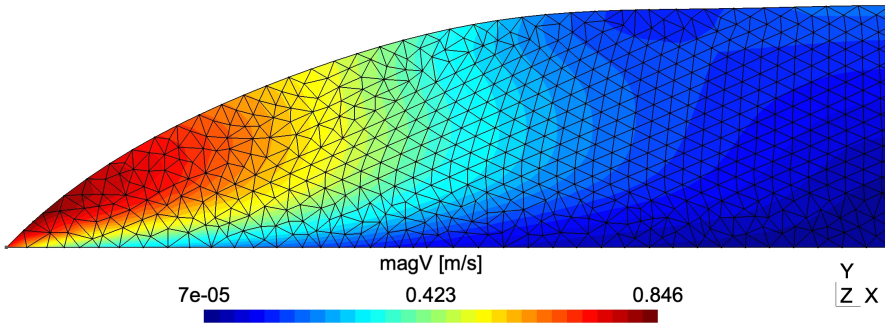

(a) $\beta_s = 178$ [Pa · s/m], $t = 2 \times 10^{-4}$ [s].

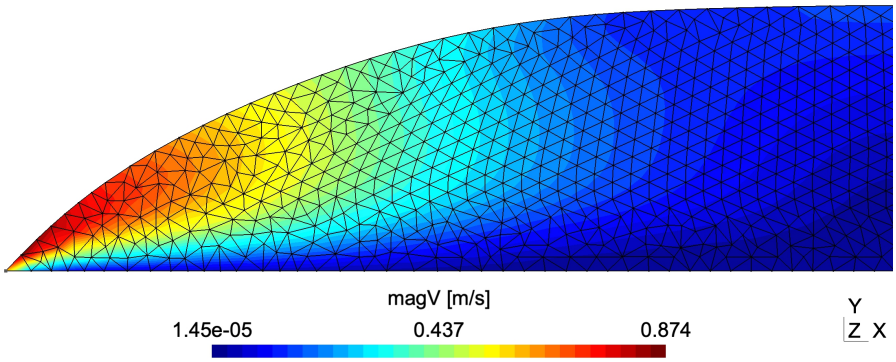

(b) $\beta_s = 890$ [Pa · s/m], $t = 2 \times 10^{-4}$ [s].

Figure III.18: Extension of the boundary layer for different values of the Navier-slip coefficient β_s. Here, a fine mesh is used ($h = 5 \times 10^{-6}$ [m]) and the value of Δt remains $\Delta t = 2 \times 10^{-7}$ [s].

meshes. Despite this mesh dependency of the numerical result in terms of the graphical data (Fig III.16) as well as the visual data (Figs. III.17, III.18), the graphical data hints towards mesh independence for increasing values of β_s (subsequently, for decreasing values of h_{slip}). To verify this claim, the fine mesh and coarse mesh results, resp. Figs. III.16a and III.16b, are put together in Fig. III.19. It can clearly be observed that as the value of the Navier-slip coefficient increases, the numerical solution becomes less dependent on the characteristic element size. This can be interpreted as some sort of asymptotic behaviour

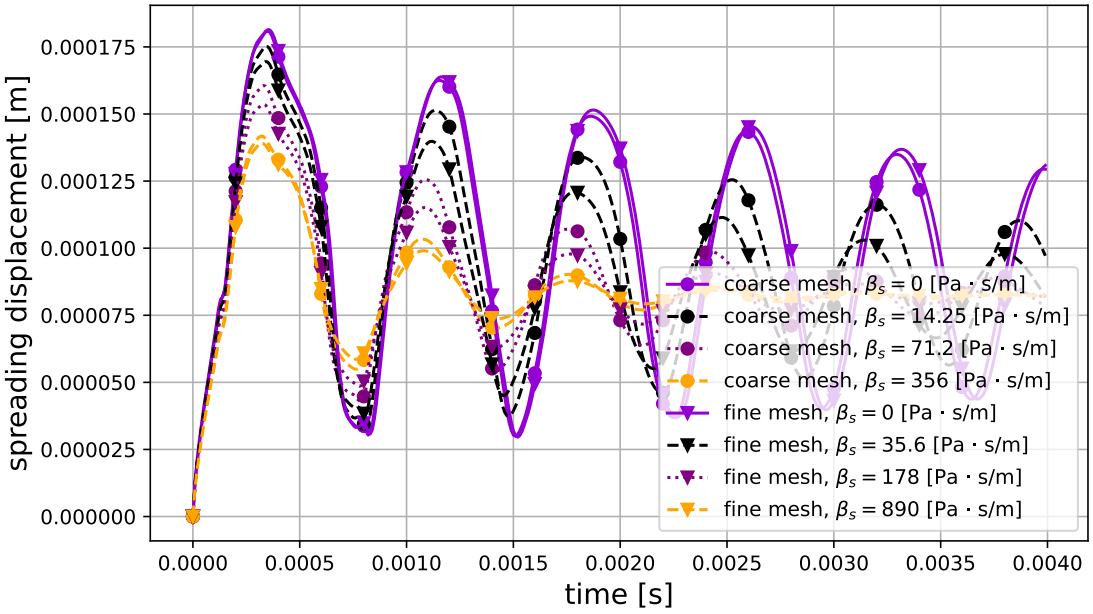

(a) View over the entirety of the simulation.

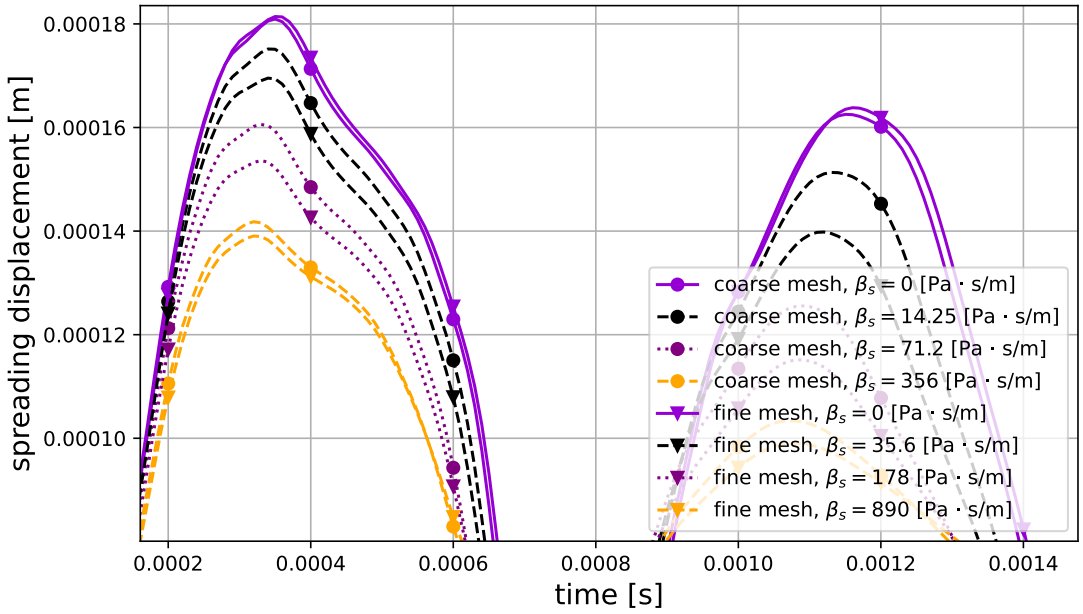

(b) Zoom on Fig. III.19a.

Figure III.19: Droplet spreading displacement for both the coarse mesh ($h = 1.25 \times 10^{-5}$ [m]) and the fine mesh ($h = 5 \times 10^{-6}$ [m]) as a function of the value of the Navier-slip coefficient. In all cases, the time-step Δt is set to $\Delta t = 2 \times 10^{-7}$ [s].

of β_s, and hence of h_{slip}, which is reported in the work of Cremonesi [12] as well.

The result obtained hereabove on mesh independence of the numerical solution for

droplet spreading displacement as a function of the Navier-slip coefficient can be summarized as follows : if the value of the slip length h_{slip} is chosen as $h_{\text{slip}} = h/5$, then by choosing the value of the Navier-slip coefficient at $\Gamma'_{\text{FS}} \equiv \Gamma_{\text{FS}} \cup \partial\Gamma$ according to :

$$\beta_s = \frac{\mu}{h_{\text{slip}}}, \tag{III.50}$$

the numerical solution is, in good approximation, independent of the choice of h. It is important to underline that this result holds in the context of this work, but is by no means a *general* result that should work for any simulation case, as mentioned by Cremonesi [12]. On the hand of this observation, the difference between the results provided between the coarse and fine meshes are quantified below :

- $\Delta_f = 1.13$ [%] ;
- $\Delta_O = 1.56$ [%],

which only enforces the statement on mesh independence of the numerical solution for droplet spreading displacement (when the correct value for β_s is chosen, of course).

Now that mesh independence as well as physical relevance of the numerical results obtained with `PFEM3D` are assessed, these results can be compared with the ones provided by Mahrous [9]. In [9], only one case study in which the same value of the Navier-slip coefficient is imposed at the liquid-substrate interface Γ_{FS} and the contact line $\partial\Gamma$ is presented. For this case, $\beta_s = 10^{-3}$ [Pa · s] (the units seem to be faulty, so the relevance of this value is questionable). The reason for this particular choice is not explicitly mentioned in the work. The main takeaway of this study is that an increase of the value of the Navier-slip coefficient results in a more rapid stabilisation of the contact line due to increased damping of the droplet displacement spreading oscillations, which is also observed in the results computed by `PFEM3D` (Figs. III.16, III.19). As observed in the previous section (no consideration for the dissipation due to friction at the liquid-substrate interface as well as at the contact line), the numerical response is, in contrast with this work, very mesh dependent. Indeed, for the coarse mesh (Fig. III.20a, *cf.* « case 3 »), the droplet oscillates ~ 3 times before reaching its equilibrium value, while for the fine mesh (Fig. III.20b, *cf.* « case 3 »), the spreading displacement tends to its equilibrium position without oscillating. These results are presented in Fig. III.20. In terms of the behaviour of the droplet spreading displacement using the coarse mesh, the result obtained from `PFEM3D` using $\beta_s = 356$ [Pa · s/m] is very similar to the graph Fig. III.20a « case 3 » obtained in [9]. Indeed, `PFEM3D` also models that the droplet oscillates ~ 3 times before reaching its equilibrium configuration. In terms of the value of the droplet spreading displacement at equilibrium, both models are once more in excellent agreement. For the fine mesh simulations, Fig. III.20b « case 3 » models a critical damping/overdamping regime for the droplet spreading displacement, while the result obtained in Fig. III.16b obeys a regime of underdamping for $\beta_s = 890$ [Pa · s/m].

Once more, the results obtained by `PFEM3D` and by [9] are different, especially for the case in which a fine mesh ($h = 5 \times 10^{-6}$ [m]) is used. Indeed, for the fine mesh, there is still no agreement on the damping regime between Figs. III.16b and III.20b. In contrast, for the coarse mesh simulations ($h = 1.25 \times 10^{-5}$ [m]), the predictions from `PFEM3D` and [9]

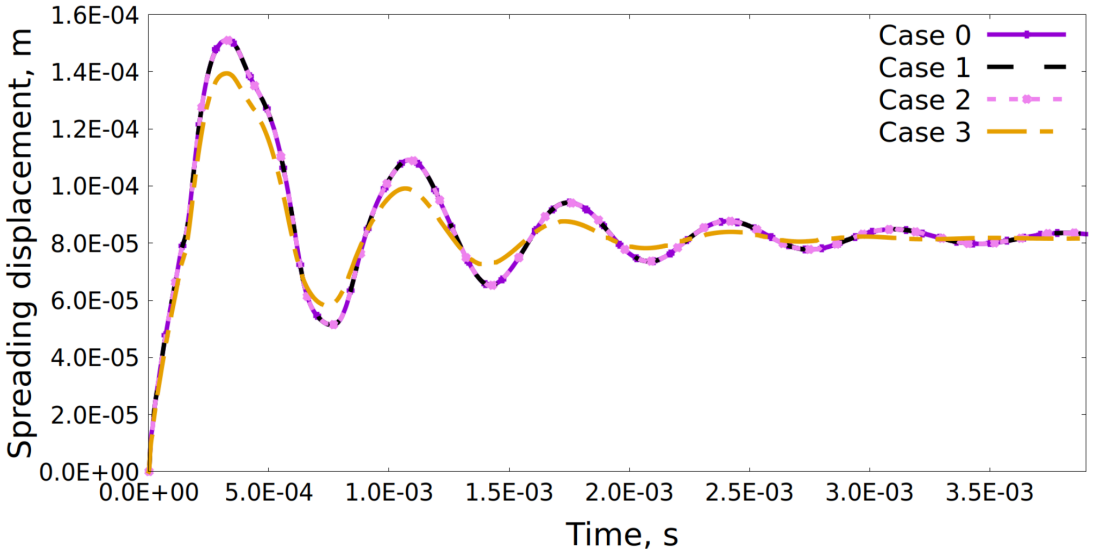

(a) Coarse mesh ($h = 1.25 \times 10^{-5}$ [m], 340 elements).

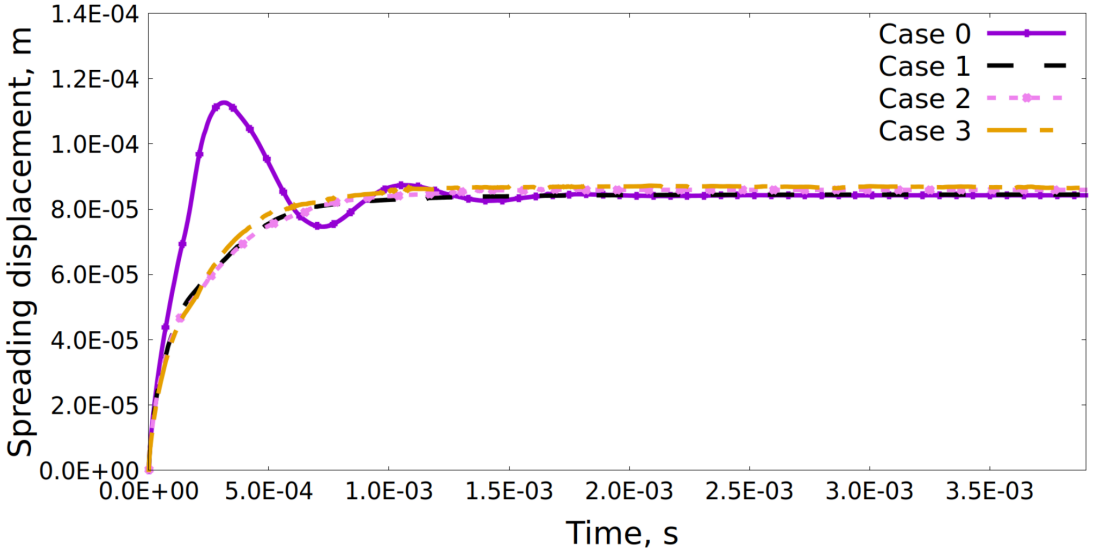

(b) Fine mesh ($h = 5 \times 10^{-6}$ [m], 2,206 elements).

Figure III.20: Droplet spreading displacement over time modelled by [9]. The curves of interest in the context of this work are called « case 0 » (no consideration of the dissipation due to friction at the liquid-substrate interface and at the contact line) and « case 3 » (same values for the Navier-slip coefficient are imposed at the liquid-substrate interface and the contact line). For both graphs, the time-step Δt is set to $\Delta t = 2 \times 10^{-7}$ [s].

are starting to look more alike, in terms of the overall shape of the curves (Figs. III.16a, III.20a) as well as the obtained values for the frequency, the overshoot and the spreading displacement at equilibrium. For the fine mesh simulations, this difference in behaviour between the two models most certainly comes from the initial difference described in the previous section, in which no additional forces were considered. It remains to be seen if this difference disappears (or not) when taking into account the lacking contributions at the contact line $\partial\Gamma$.

5.3.3 Influence of the capillary effect and the normal stress component at $\partial\Gamma$

For the final part of the validation of the numerical model, the impact of the forces related to the capillary effect and the normal stress jump, both acting at the contact line, is studied. Mahrous [9] suggests studying the impact of the capillary force term and the force term related to the normal stress jump separately, but in the context of this work, the impact of these terms will be studied simultaneously. It is reminded that these forces are expressed as Eq. III.30 :

$$\text{additional forces at contact line } \partial\Gamma = -\zeta\mathbf{v} - \beta_n\mathbf{v}, \tag{III.51}$$

where ζ is the coefficient related to the capillary force :

$$\zeta = \frac{\gamma}{u}(\cos\theta_s + 1)\tanh\left(4.96\text{Ca}^{0.702}\right), \tag{III.52}$$

with $\text{Ca} = u\mu/\gamma$ the capillary number, and β_n is the coefficient related to the normal stress jump :

$$\beta_n = \frac{1}{u}\mu\nabla(\mathbf{v}\cdot\mathbf{t})\cdot\mathbf{t}. \tag{III.53}$$

In contrast with the Navier-slip coefficient (related to the dissipation at the liquid-substrate interface as well as at the contact line), for which an alternative expression was used, Eqs. III.51, III.52 and III.53 are implemented the same way in `PFEM3D` as in [9]. At this stage of the work, both the surface tension force at the contact line as well as the dissipation at Γ'_{FS} are taken into account. For the latter, it has been determined previously that when the value of the slip length h_{slip} is equal to the characteristic element size h divided by 5, $h_{\text{slip}} = h/5$, and when β_s is computed as $\beta_s = \mu/h_{\text{slip}}$, then the numerical solution does not depend on the characteristic element size.

As suggested in [9], only the coarse mesh ($h = 1.25 \times 10^{-5}$ [m]) and the fine mesh ($h = 5 \times 10^{-6}$ [m]) are considered for this study. The simulation results using `PFEM3D` are presented in Fig. III.21. It is noted that the simulation time $\mathcal{T}$ is divided by a factor 2 with respect to the previous case studies ($\mathcal{T} = 2 \times 10^{-3}$ [s] instead of $\mathcal{T} = 4 \times 10^{-3}$ [s]) in this work for the two following reasons :

- According to the work of Mahrous [9], the spreading displacement stabilizes around $t \simeq 10^{-3}$ [s], both for the coarse and the fine meshes ;
- With PFEM3D, the computations do not converge for $\Delta t = 2 \times 10^{-7}$ [s], such that smaller time-steps need to be used. This ultimately leads to a drastic increase of the CPU-time. Indeed, while the average CPU-time for simulations without Eq. III.51 implemented in `PFEM3D` is $\simeq 780$ [s] (using the fine mesh $h = 1.25 \times 10^{-5}$ [m]), this value increases to over 5 hours when Eq. III.51 is taken into account.

Fig. III.21 shows that for both the coarse and the fine meshes, the behaviour of the spreading displacement is such that it peaks around $t = 3 \times 10^{-4}$ [s] and then decreases to its equilibrium value 8.25×10^{-5} [m], which is attained at $t \simeq 10^{-3}$ [s]. This is the exact behaviour that is also modelled in [9], for which the coarse mesh and fine mesh graphs are given in Fig. III.22.

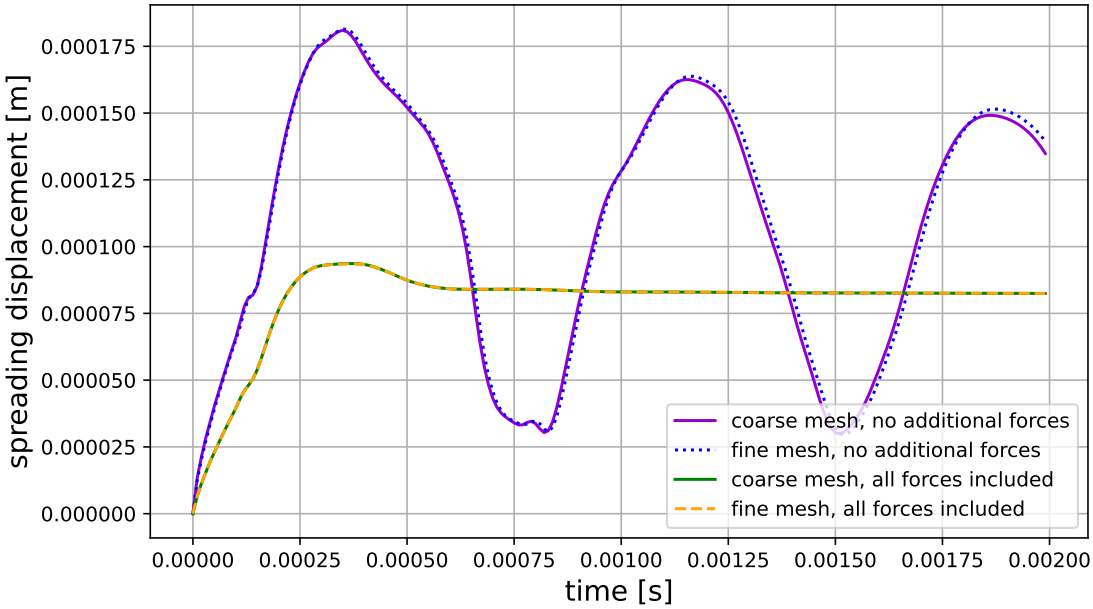

(a) View over the entirety of the simulation.

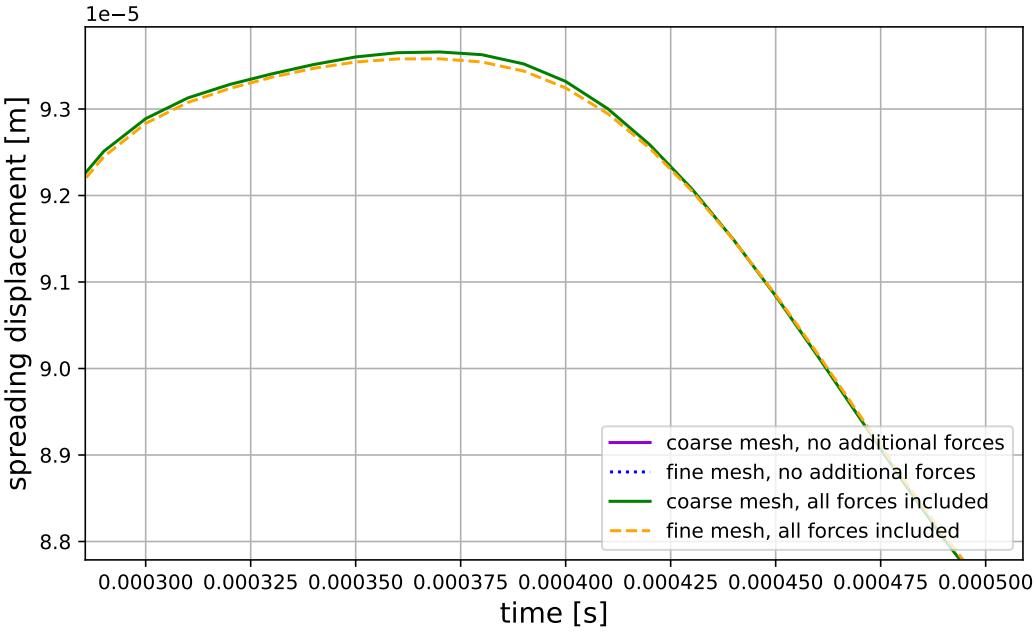

(b) Zoom on Fig. III.21a.

Figure III.21: Droplet spreading displacement using the coarse mesh ($h = 1.25 \times 10^{-5}$ [m]) and the fine mesh ($h = 5 \times 10^{-6}$ [m]), both with and without the full set of additional forces.

Qualitatively speaking, the behaviour modelled by `PFEM3D` and [9] is exactly the same, which is underlined by Figs. III.21 and III.22. To quantitatively study the difference

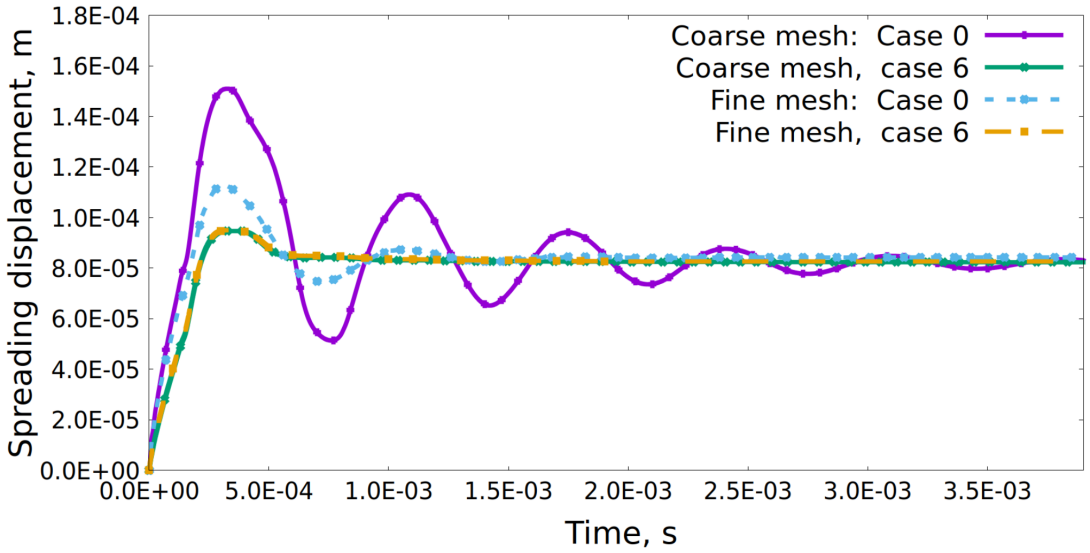

Figure III.22: Droplet spreading displacement over time modelled by [9]. A comparison between the coarse mesh and fine mesh studies, with and without the full set of forces (resp. « case 6 », « case 0 ») is performed. The time-step Δt is set to $\Delta t = 2 \times 10^{-7}$ [s].

between the two models, the following analyses are considered :

- Values for the overshoot :
  - `PFEM3D` : t-coordinate $t = 3.7 \times 10^{-4}$ [s], spreading displacement coordinate $= 9.36 \times 10^{-5}$ [m] ;
  - [9] : t-coordinate $t \simeq 3.3 \times 10^{-4}$ [s], spreading displacement coordinate $\simeq 9.52 \times 10^{-5}$ [m] ;
  - Difference on the t-coordinate $\Delta_t \simeq 12.12$ [%], difference on the spreading displacement coordinate $\Delta_{\text{spreading displacement}} \simeq 1.68$ [%] ;
- Values for the spreading displacement at equilibrium :
  - `PFEM3D` : spreading displacement at equilibrium $= 8.25 \times 10^{-5}$ [m] ;
  - [9] : spreading displacement at equilibrium $\simeq 8.13 \times 10^{-5}$ [m] ;
  - Difference on the spreading displacement at equilibrium $\Delta_{\text{spr. displ. at eq.}} \simeq 1.47$ [%] ;
- Values for the maximal contact line velocity :
  - `PFEM3D` : maximal contact line velocity $u_{\max} = 6.46 \times 10^{-1}$ [m/s] ;
  - [9] : maximal contact line velocity $u_{\max} \simeq 6.03 \times 10^{-1}$ [m/s] ;
  - Difference on the maximal contact line velocity $\Delta_{u_{\max}} \simeq 7.13$ [%].

6 Conclusion

This part of the work has been dedicated to the extension of the PFEM3D solver in order to correctly represent droplet spreading behaviour on a substrate.

In a first instance, it has been pointed out that the surface tension contribution Eq. III.21 was missing in the FE formulation of PFEM3D, whose role is to take account for the force arising from the *dynamic* contact angle at the droplet contact line. To implement this force, the approach suggested by Jarauta [10] has been followed and allowed for an *implicit* formulation of this lacking term. This approach turned out to be helpful, in the sense that *curvature* is a quantity that cannot be computed by PFEM3D. In addition, a HFS BC has been implemented.

After the addition of this force to the FE implementation of PFEM3D, the other lacking contributions allowing for a correct modelling of droplet spreading behaviour have been identified using [9] as a reference source. In his work, Mahrous [9] suggested the addition of (a) a dissipative term taking account of friction at the liquid-substrate interface as well as at the contact line, (b) a term taking account of the capillary effect at the contact line and (c) a term taking account of the normal stress jump at the contact line.

While this exact strategy has been followed for the completion of the PFEM3D computer code, some of the expressions suggested by Mahrous [9] have not been used, but rather formulated alternatively. For instance, while the setup suggested by Mahrous consisted of a droplet with an initial contact angle of 90 [deg] which evolved *naturally* to a value of 45 [deg] to attain equilibrium, this work considered also an initial contact angle of 90 [deg], but was instantaneously set, at the following time-step, to 45 [deg], *imposing* this equilibrium value rather than letting it evolve naturally. Furthermore, for the expression of the Navier-slip coefficient (related to the dissipative friction at the contact line as well as at the liquid-substrate interface), [9] suggested Eq. III.49 while in this work, Eq. III.28 has been used (based on the work of Meduri [11]) in combination with the mesh-dependent nature of the slip length (described by Cremonesi [12]).

Despite the use of these different formulations, it has been proven extensively that the results obtained by PFEM3D are in excellent agreement with the observations described by Mahrous [9] once the entire set of forces is implemented. Indeed, while initially the error on the *dynamic* values (*e.g.* oscillation frequency and overshoot) was far from being negligible, once the entire set of forces prescribed by [9] was implemented, these differences virtually vanished. In addition, while the implementation of [9] exhibited mesh-dependent behaviour of the numerical solution, PFEM3D did not show such behaviour. It is however underlined once more that in the case of the dissipation force at Γ'_{FS}, the value of the Navier-slip coefficient must be chosen is accordance with the prescriptions of Cremonesi [12] for this statement to be true.

At this stage of the work, it is safe to say that PFEM3D is able to model droplet spreading behaviour with great accuracy now that the full set of forces are implemented in its FE formulation. For this reason, PFEM3D is deemed acceptable for further extension to model even more complex phenomena. In the following and last part of this work, a simple model for *contact angle hysteresis* introduced and added to the computer model.

Wolfgang Pauli (1900 - 1958) is credited for saying « God made the bulk ; surfaces were invented by the devil ». This saying does not leave much room for worse. If there is something worse, we will nominate « contact angle phenomena » first in line.

– [16].

Part IV
Further extension of PFEM3D : modelling contact angle hysteresis

In the previous part of this work, it has been demonstrated extensively that with the implementation of the additional forces in the PFEM3D computer code, the obtained results are in excellent agreement with the work of Mahrous [9], meaning that droplet spreading behaviour is now correctly modelled. The work of Mahrous [9], however, does not take account of a common phenomenon that also impacts largely droplet spreading dynamics : this phenomenon is *contact angle hysteresis*, which mostly depends on surface roughness.

While the nomenclature might sound fancy at first impression, contact angle hysteresis is a phenomenon that can easily be observed. For instance, when driving a car on a rainy day, rain drops hit the windshield constantly. When paying attention to these drops, it is observed that sometimes they move from bottom to top due to the effects of friction of the incoming wind on their free surface, sometimes they do not ; this is solely the effect of contact angle hysteresis. Another example is when after pouring a glass of water from a bottle, some water drops are suspended near the neck. If their mass is small enough, they will not bet dragged down under the effect of gravity : this is also an effect from contact angle hysteresis (this is represented in Fig. IV.1).

Figure IV.1: Near the neck of a water bottle, some droplets remain at their position without moving, despite gravity trying to drag them down. This is an effect of contact angle hysteresis.

For this final part of the work, the following structure is suggested. First, the physics of contact angle hysteresis will be explained in order to get a general understanding of the topic. Then, the work of Jarauta [10] is re-considered for the numerical implementation of a basic model taking account of this phenomenon in `PFEM3D`. Next, some first results with contact angle hysteresis are presented and discussed. Finally, general conclusions are drawn and discussed as well.

1 The physics of contact angle hysteresis

To understand the physics behind contact angle hysteresis, it might be interesting to take a step back on the notion of *contact angle*. This quantity has been introduced in the previous part of this work in the context of the surface tension force acting at the contact line of the droplet. The contact line has been defined as the point at which the liquid (water in the context of this work), the substrate and the surrounding gas phase (air in the context of this work) meet.

From a thermodynamics standpoint, the contact angle is the slope at the liquid-surrounding gas interface in the near surroundings of the contact line [16]. The value of this slope is such that it minimizes the free energy of a liquid in contact with a flat, inert, homogeneous and smooth solid interface in accordance with the well-known *Young equation* [16] :

$$\gamma_{\mathrm{L}} \cos\theta_s = \gamma_{\mathrm{S}} - \gamma_{\mathrm{SL}}, \tag{IV.1}$$

where γ_{L} [J/m^2] is the *liquid-gas interface free energy*, θ_s [deg] is the *static contact angle*, γ_{S} [J/m^2] is the *solid-gas interface free energy* and γ_{SL} [J/m^2] is the *solid-liquid interface free energy*. In the previous part of this work, the satisfaction of Young's equation is obeyed by imposing equilibrium between the horizontal components of the interface forces.

In theory, the value of the *static contact angle* θ_s is said to depend on the values of these different interfacial energies in accordance with Young's equation. In practice, however, the reality is quite different. Indeed, not only does the value of the static contact angle depend on these surface energies, but also on the surface structure, the pretreatment of these surfaces as well as their contamination level. Even worse, the notion itself of static contact angle seems to be insufficient in terms of describing a specific surface.

This is where the notion of *contact angle hysteresis* comes into play. Indeed, in any real-life context, Young's equation Eq. IV.1 is a condition that cannot be realised practically [16]. Hence, instead of describing a surface with the value of a static contact angle θ_s, the notions of *receding contact angle* θ_r [deg] and *advancing contact angle* θ_a are introduced. The *contact angle hysteresis* $\Delta\theta$ [deg] is then defined by the difference of these angles as follows :

$$\Delta\theta = \theta_a - \theta_r. \tag{IV.2}$$

Typically, the values of both the advancing contact angle and the receding contact angle depend on their respective contact line velocity, denoted u [m/s] in order to remain consistent with the notations introduced in the previous part of this work.

In practice, it is observed that the value of the static contact angle θ_s is included in the interval $[\theta_r^0, \theta_a^0]$, where θ_r^0 [deg] is the *static receding contact angle* and θ_a^0 [deg] is the *static advancing contact angle*. To understand the physical meaning of these contact angles, consider the case in which a droplet deposited on a substrate is increased in mass, for example by injecting mass through its base (by which is meant the solid-liquid interface, previously denoted Γ_{FS}). When mass is injected in the droplet, the *dynamic contact angle* will increase because of gravity as well as the contact line being *pinned*, *i.e.*, unable to move. The value for the contact angle at which the contact line is allowed to advance is then referred to as the *static advancing contact angle*. Equivalently, consider the case in which the mass of a droplet deposited on a substrate is decreased. Then the value of the contact angle at which the contact line is allowed to recede is referred to as the *static receding contact angle*. This explanation is represented in Fig. IV.2 for the static advancing contact angle.

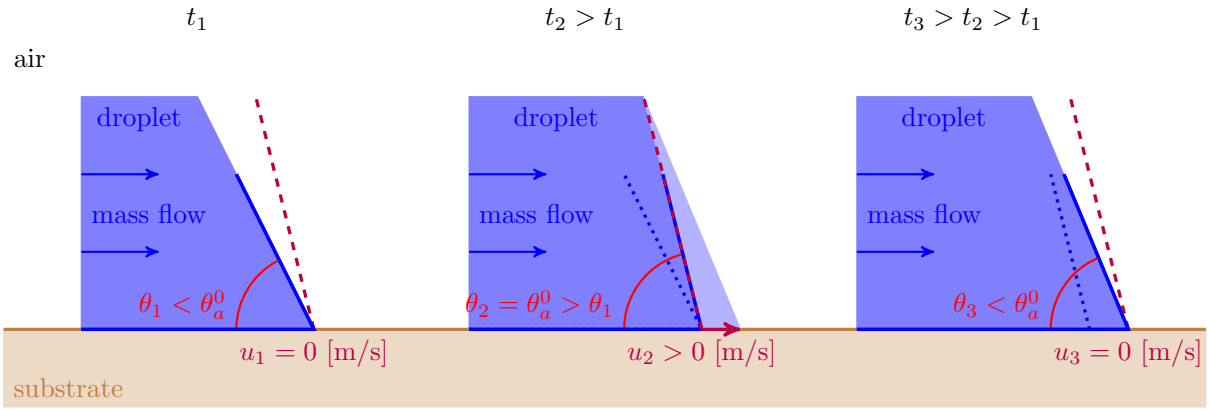

Figure IV.2: Schematic for the definition of the static advancing contact angle. At time t_1, the dynamic contact angle θ_1 is smaller than the static advancing contact angle (dashed purple line) such that the contact line is pinned. At $t_2 > t_1$, the value of the dynamic contact angle $\theta_2 > \theta_1$ is equal to θ_a^0 and thus the contact line is allowed to move (this is represented by the lighter blue surface). Finally, at $t_3 > t_2 > t_1$, $\theta_3 < \theta_a^0$ again such that the contact line is pinned once more. In this figure, the dotted blue line represents each time the previous state of the droplet free surface.

For water, which is the nature of the liquid considered in this work, the value for *static contact hysteresis* $\Delta\theta^0$ [deg], defined as :

$$\Delta\theta^0 = \theta_a^0 - \theta_r^0, \tag{IV.3}$$

is typically of the order of 10 [deg].

While what is explained hereabove is just the tip of the iceberg on the discussion of contact angle hysteresis, going any further from this stage would surpass the scope of this work. Indeed, the main concepts has been presented and can be summarized as follows :

- The *static contact angle* θ_s is included in the interval $[\theta_r^0, \theta_a^0]$, where θ_r^0 is the *static receding contact angle* and θ_a^0 is the *static advancing contact angle*. These values are what describe the nature of a substrate ;

- When the *dynamic contact angle* θ is in the interval $[\theta_r^0, \theta_a^0]$, the contact line is said to be *pinned*, *i.e.*, the contact line is not allowed to move ;
- When the *dynamic contact angle* θ is greater than the *static advancing contact angle* θ_a^0, the contact line is allowed to move. When the contact line moves, the *dynamic contact angle* becomes once more smaller than the *static advancing contact angle*, at which point the contact line is *pinned* again ;
- When the *dynamic contact angle* θ is smaller than the *static receding contact angle* θ_r^0, the contact line is allowed to move. When the contact line moves, the *dynamic contact angle* becomes once more greater than the *static receding contact angle*, at which point the contact line is *pinned* again.

2 Implementation of contact angle hysteresis in the numerical model

With a general understanding of contact angle hysteresis in mind, a way of implementing this phenomenon in `PFEM3D` can be discussed. For this implementation, the approach suggested by Jarauta [10] is followed.

Before explaining the approach suggested by Jarauta [10], a step must be taken back on the implementation of the contact angle in `PFEM3D`. In the previous part of this work (Part III), the contact angle was introduced during the discussion of the implementation of the surface tension force at the contact line $\partial\Gamma$. As a reminder, the expression for the surface tension force in the Galerkin formulation is described by Eq. III.21, namely :

$$\text{surface tension force at } \partial\Gamma = -\int_{\partial\Gamma} \gamma \mathbf{m} \cdot \mathbf{w} \, \mathrm{d}\partial\Gamma, \tag{IV.4}$$

where γ is the liquid surface tension (water in the context of this work), $\mathbf{m}$ is the vector that is tangent to the droplet free surface Γ_L at $\partial\Gamma$ and $\mathbf{w}$ is an arbitrary KA test function. Considering the 2D framework and introducing linear isoparametric elements (Eq. III.10), it has been demonstrated that Eq. IV.4 can be reduced to :

$$-\gamma \mathbf{m}. \tag{IV.5}$$

A visual interpretation of the vector $\mathbf{m}$ is reminded in Fig. IV.3. During the discussion of the verification of the numerical model `PFEM3D` without considering the effect any additional forces on droplet spreading displacement behaviour except for the surface tension force (which was initially lacking in the FE formulation of `PFEM3D`), it has been pointed out that the value of the contact angle can be imposed through the components (m_1, m_2) of $\mathbf{m}$. While Fig. III.12 was used in the context of *imposing* the value of the contact angle, it can also be used to explain how to *measure*. This representation is reminded in Fig. IV.4.

While Jarauta [10] does not mention that it is not possible to model contact angle hysteresis for equilibrium angles that differ from 90 [deg] using the implicit treatment for the surface tension term, the way `PFEM3D` is implemented, as well as the method for imposing equilibrium contact angles, does prevent this at the moment. Indeed, [10]

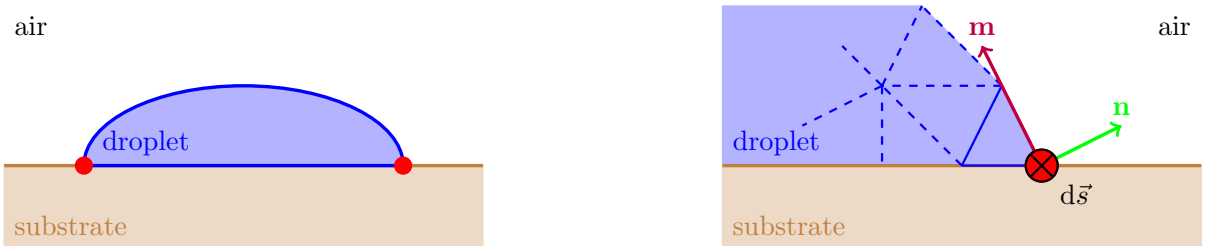

Figure IV.3: Visual interpretation of the vector **m**, which is tangent to the droplet free surface Γ_L at the contact line $\partial\Gamma$. The vector **m** denotes the outward normal vector to the droplet free surface and the vector d**s**, written $d\vec{s}$ in this figure, gives the direction of the contact line.

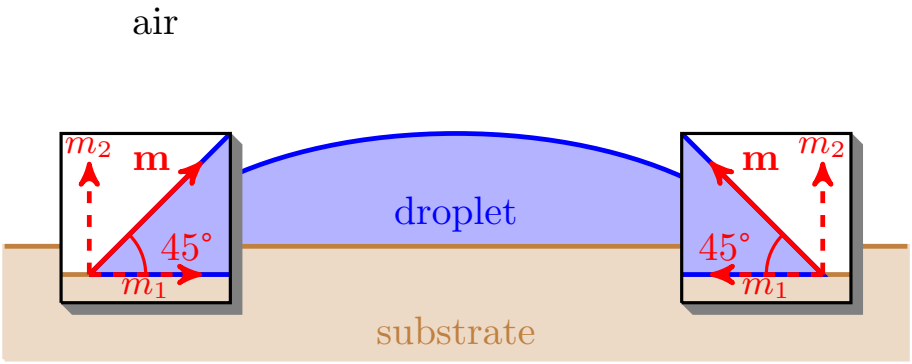

Figure IV.4: Measuring of the value of the contact angle through the components of the vector **m**.

imposes, near the contact line, the value of the *curvature* such that the contact angle evolves around this imposed value. In `PFEM3D`, it is not possible to calculate curvatures, such that this approach cannot be used. This is the reason why, for the validation step of the numerical model discussed in the previous part of this work, the equilibrium contact angle has been « hard-coded » by setting the value of the components (m_1, m_2) of the tangent vector **m**. However, for an equilibrium value of 90 [deg], the implicit treatment of the surface tension force at the contact line does allow « natural » variation of the contact angle, such that the phenomenon of contact angle hysteresis can be modelled for this particular value.

In other words, the contact angle at the contact line can evolve as a *dynamic* variable if the value of θ_s is set to 90 [deg]. For this reason, for the remainder of this work, it is considered, per default, that $\theta_s = 90$ [deg].

With this important remark in mind, the strategy for implementing contact angle hysteresis suggested by Jarauta [10] can be explained. In accordance with the theory related to contact angle hysteresis, the values of the static advancing contact angle θ_a^0 as well as that of the static receding contact angle θ_r^0 are imposed in `PFEM3D`. Given it has been pointed out hereabove that the value for the static contact angle hysteresis $\Delta\theta^0$ for water is typically of the order of 10 [deg], a reasonable choice for the interval $[\theta_r^0, \theta_a^0]$ is :

$$[\theta_r^0, \theta_a^0] = [85, 95] \text{ [deg, deg]}, \tag{IV.6}$$

where θ denotes the value of the *dynamic* contact angle. The following condition for the pinning of the contact line is then implemented :

$$\begin{cases} \text{if } \theta \text{ is such that : } \theta_r^0 < \theta < \theta_a^0, \text{ then the contact line is pinned ;} \\ \\ \text{else, the contact line is allowed to move and its velocity is calculated} \\ \text{in accordance with Eq. III.45.} \end{cases} \tag{IV.7}$$

3 Initial test

3.1 Problem suggestion

In order to check if the phenomenon of contact angle hysteresis is implemented correctly in the `PFEM3D` computer code, consider the following simple case study. Initially, a water droplet ($\rho = 10^3$ [kg/m^3], $\mu = 10^{-3}$ [Pa $\cdot$ s], $\gamma = 72.8 \times 10^{-3}$ [N/m]) of radius R is deposited on a substrate characterised by a static contact angle $\theta_s = 90$ [deg], a static advancing contact angle $\theta_a^0 = 95$ [deg] and a static receding contact angle $\theta_r^0 = 85$ [deg]. By suggesting these values, the static contact angle hysteresis is $\Delta\theta^0 = \theta_a^0 - \theta_r^0 = 10$ [deg] and is in agreement with the theoretical discussion hereabove. Furthermore, the condition $\theta_r^0 < \theta_s < \theta_a^0$ is also satisfied. The only body force to which the droplet is subjected is considered to be gravity. If the value of the dynamic contact angle is initially considered such that $\theta_r^0 < \theta < \theta_a^0$, and if the droplet mass is great enough, the effect of gravity is to flatten its shape, subsequently increasing the dynamic contact angle in order to satisfy volume conservation. This is schematically represented in Fig. IV.5.

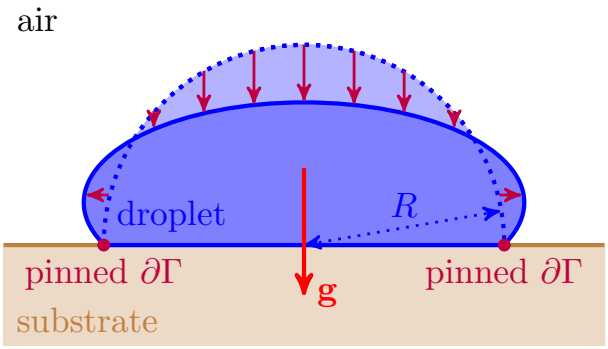

Figure IV.5: Under the effects of gravity, if the droplet mass is great enough, the droplet (initially shaped as a semi-circle, represented in the blue dotted lines) will flatten into an ellipse-like shape (whole blue line) as mass is displaced from top to bottom (purple vectors), which leads to an increase of the contact angle. If this contact angle θ is $< \theta_a^0$, the contact line $\partial\Gamma$ is pinned.

When this value of the dynamic contact angle reaches that of the static advancing contact angle, the contact line is allowed to move and the droplet will spread on the substrate.

3.2 Choice of the initial geometry

A relevant dimensionless number which characterises the competition between the gravitational pull and the capillary force is the *Bond number* (also called the *Eötvös number*), denoted Bo [-] and defined as :

$$\text{Bo} = \frac{\rho g L^2}{\gamma}, \tag{IV.8}$$

where L is the characteristic length of the water droplet. It is said that the gravitational pull dominates over the capillary force if $\text{Bo} > 1$, in which case the droplet mass should be great enough to flatten the droplet. The « critical » value for L is then obtained as :

$$\text{Bo} > 1 \quad \Longrightarrow \quad L > \sqrt{\frac{\gamma}{\rho g}} = 2.7 \text{ [mm]}. \tag{IV.9}$$

In other words, if the characteristic length of the water droplet is greater than this value, its mass should be great enough for the gravitational force to dominate over the capillary force and the contact line should be able to move. Indeed, the deformation of the water droplet should lead to the dynamic contact angle being able to take values greater than the static advancing contact angle, *i.e.*, $\theta > \theta_a^0$. Hence, a relevant choice for the droplet initial radius is $R = 1.5$ [mm], such that the initial base length (the length of the liquid-substrate interface) is equal to 3 [mm]. The value of the Bond number is then $\text{Bo} = 1.21 > 1$ [-].

3.3 Choice of the numerical parameters

In the previous part of this work, it has been demonstrated that the numerical solution is independent of the characteristic element size if the complete set of surface forces is implemented in the FE formulation. This statement has been validated for a coarse mesh with characteristic element size h equal to a tenth of the characteristic drop length. Thus, given $R = 1.5$ [mm] in the framework of the current study, $h = 0.15$ [mm] seems a relevant choice for a coarse mesh (223 nodes, 446 elements). A fine mesh characteristic element size is chosen as 0.05 [mm], in which case 1,770 nodes and 3,540 elements constitute the FE mesh. A representation of these meshes is provided in Fig. IV.6.

The value of the time-step Δt is set as $\Delta t = 10^{-5}$ [s] for this first case study. Other simulation parameters are the simulation time $\mathcal{T} = 0.1$ [s] and the alpha-parameter $\alpha = 1.2$.

In the previous part of this work, it has been pointed out that the numerical results do not depend on the characteristic element size h if the prescribed condition on the value of the Navier-slip coefficient β_s is satisfied. It is reminded that this condition is :

$$h_{\text{slip}} = \frac{h}{5} \, ; \quad \beta_s = \frac{\mu}{h_{\text{slip}}}, \tag{IV.10}$$

Hence, the values β_s^{coarse} and β_s^{fine} are obtained as :

$$\beta_s^{\text{coarse}} = 33.3 \text{ [Pa} \cdot \text{s/m]} \, ; \quad \beta_s^{\text{fine}} = 100 \text{ [Pa} \cdot \text{s/m]}. \tag{IV.11}$$

It remains to be studied if this mesh independence on the numerical results is also observed.

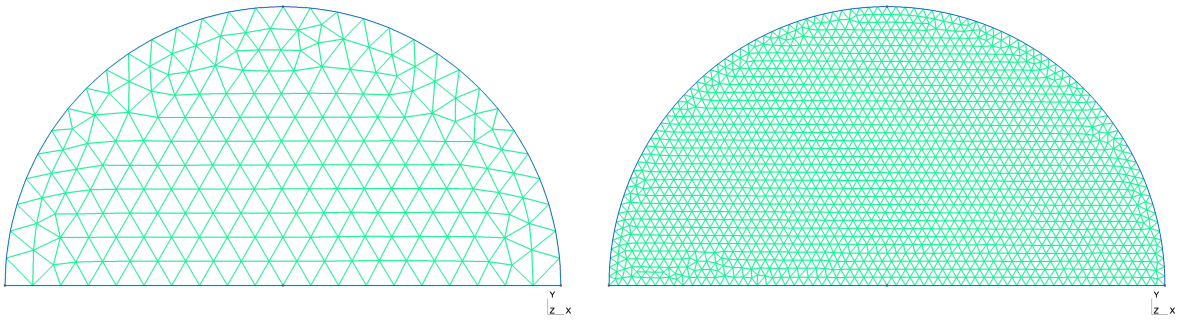

(a) Coarse mesh, $h = 0.15$ [mm] (223 nodes, 446 elements).

(b) Fine mesh, $h = 0.05$ [mm] (1,770 nodes, 3,540 elements).

Figure IV.6: Representation of the coarse and fine meshes used for the case study under investigation.

3.4 Initial results

The graphs obtained for this case study are represented in Fig. IV.7. Both the spreading displacement, used in the previous part of this work (*cf.* Fig. III.11), as well as the dynamic contact angle are measured over time.

It is revealed, in the graph measuring the evolution of the spreading displacement over time (Fig. IV.7a), that in contrast with the result obtained in the previous part of this work, the numerical solution is not independent of the FE mesh. Indeed, while the contact line remains pinned during the entire simulation using the coarse mesh, this is not the case for the fine mesh simulation. It is shown in the latter solution that the evolution of the spreading displacement is rather erratic.

This behaviour is understood better when the graphs for the evolution of the contact angle (Figs. IV.7b, IV.7c) are taken into consideration. Indeed, these graphs show that while the dynamic contact angle for the coarse mesh simulation oscillates smoothly in between the range $[\theta_r^0, \theta_a^0] = [85, 95]$ [deg, deg], the value of the dynamic contact angle for the fine mesh simulation oscillates extremely rapidly between the upper and lower values of these bounds. This unstable and rapid evolution of the contact angle over time leads to droplet oscillations that increase over time. This result is non-physical, because it suggests that the energy of the system increases, which is in violation with the second law of thermodynamics.

Disregarding this nonphysical result, the implementation on the contact angle hysteresis itself seems to perform as expected. Indeed, when the value of the dynamic angle reaches either the upper or the lower bound, its value is drawn back into the contact angle hysteresis interval due to the contact line being set in motion.

3.5 Discussion

While the evolution of the value of the dynamic contact angle over time is smooth for coarse mesh simulations, this is not observed when a fine mesh is used. Indeed, in the latter case, the oscillations of the dynamic contact angle are highly unstable and result

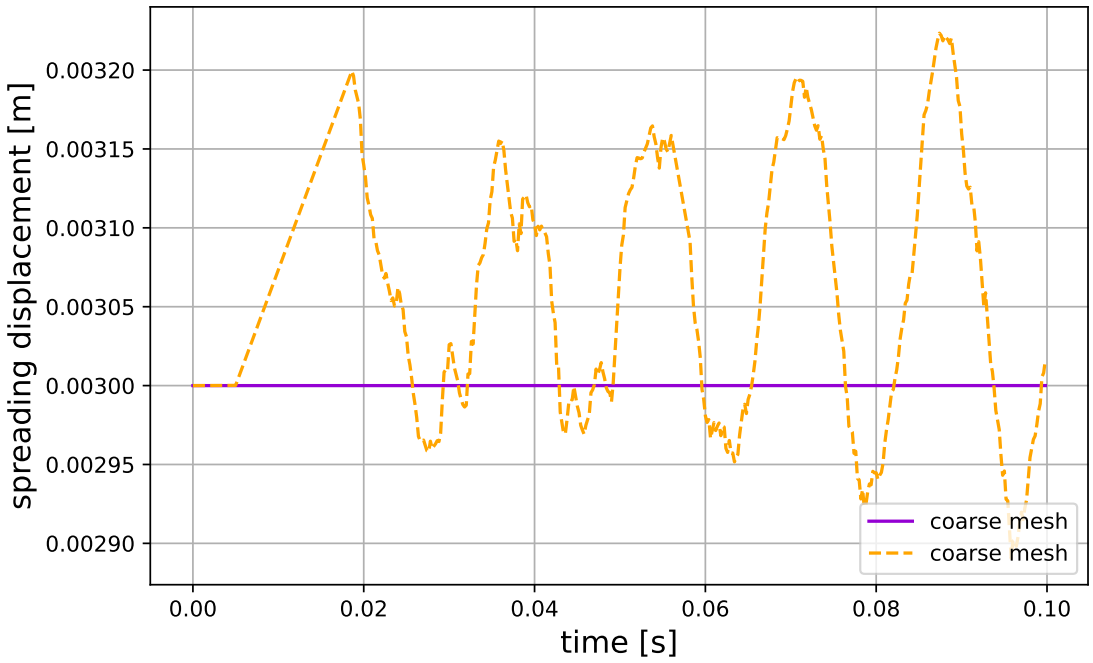

(a) Spreading displacement.

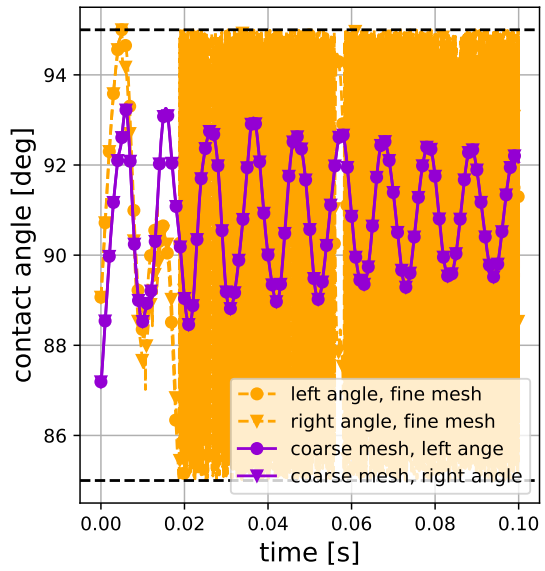

(b) Dynamic contact angle.

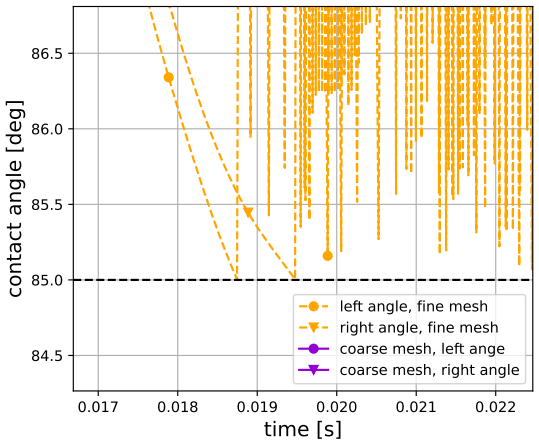

(c) Zoom on Fig. IV.7b.

Figure IV.7: Representation of the spreading displacement and the dynamic contact angle over time for coarse ($h = 0.15$ [mm]) and fine ($h = 0..5$ [mm]) meshes.

in nonphysical behaviour of the spreading displacement, namely its oscillation amplitude increases over time. It might at this stage be interesting to check if this behaviour is observed only for fine mesh simulations, or if this is inherent to the simplicity of the

model that is chosen to implement contact angle hysteresis. To perform this study, the problem suggested in the following section studies the motion of a droplet on an incline of which the angle of inclination is increased incrementally. It should be observed that if the angle of the incline is below a certain threshold value, the droplet is not allowed to slide. When this threshold value is surpassed, however, the contact line should be allowed to slide down the incline.

4 Droplet on an inclined plane

For further study of the implementation of contact angle hysteresis, the following problem is considered. A droplet is deposited on a plane which can be inclined in various manners, characterised by the angle of inclination ξ [deg]. The droplet is submitted to the gravitational pull $\mathbf{g}$. This case study is represented in Fig. IV.8.

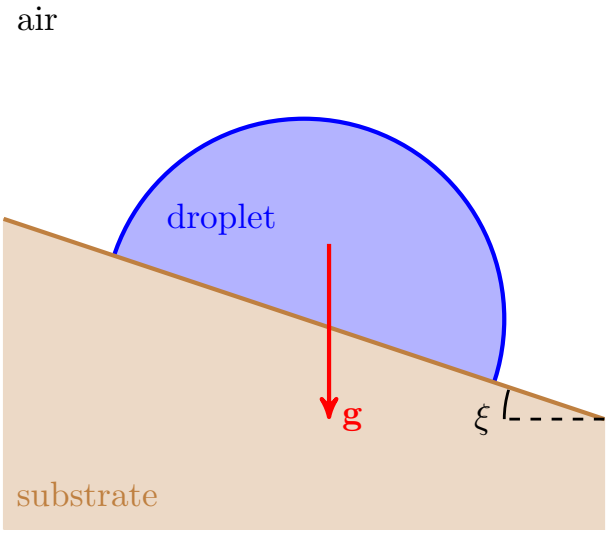

Figure IV.8: Representation of the droplet deposited on an inclined plane.

Depending on the value of the inclination angle ξ, the droplet should be allowed to slip down the incline or not. This is another way of qualitatively verifying if the baseline of the phenomenon of contact angle hysteresis is correctly represented by the numerical model. The following suggestions for ξ are suggested :

- $\xi = 0$ [deg] ;
- $\xi = 5$ [deg] ;
- $\xi = 10$ [deg] ;
- $\xi = 15$ [deg].

For this case study, the same geometry for the water droplet is chosen, being that its initial radius is 1.5 [mm]. Furthermore, the values for the static advancing and static receding contact angles are also maintained, *i.e.*, $\theta_a^0 = 95$ [deg] and $\theta_r^0 = 85$ [deg]. The

characteristic element size h is once more set to $h = 0.15$ [mm] and the value of the time-step Δt is maintained at $\Delta t = 10^{-5}$ [s] as well. For this simulation setup, the obtained graphs are presented in Figs. IV.9, IV.10.

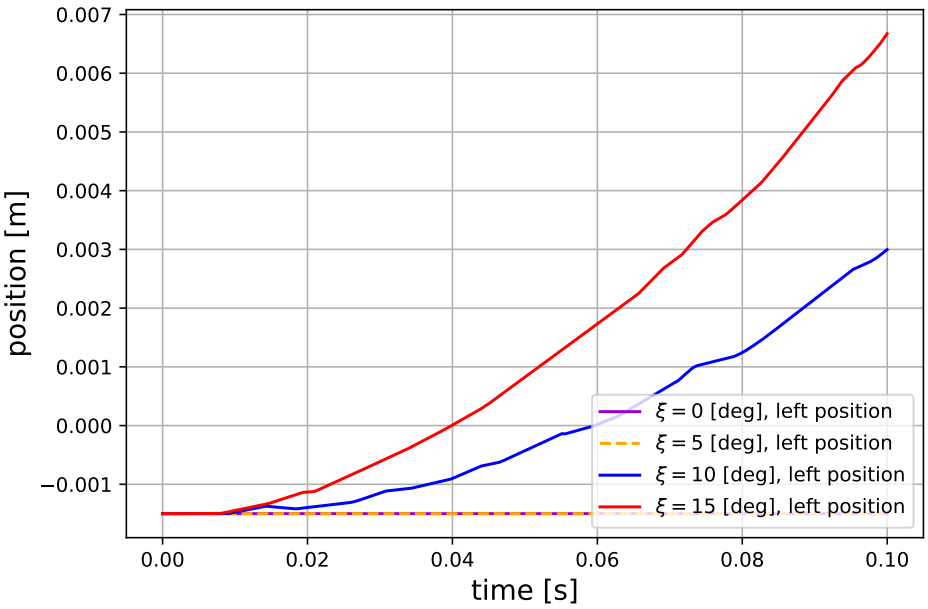

(a) Position of the left contact line.

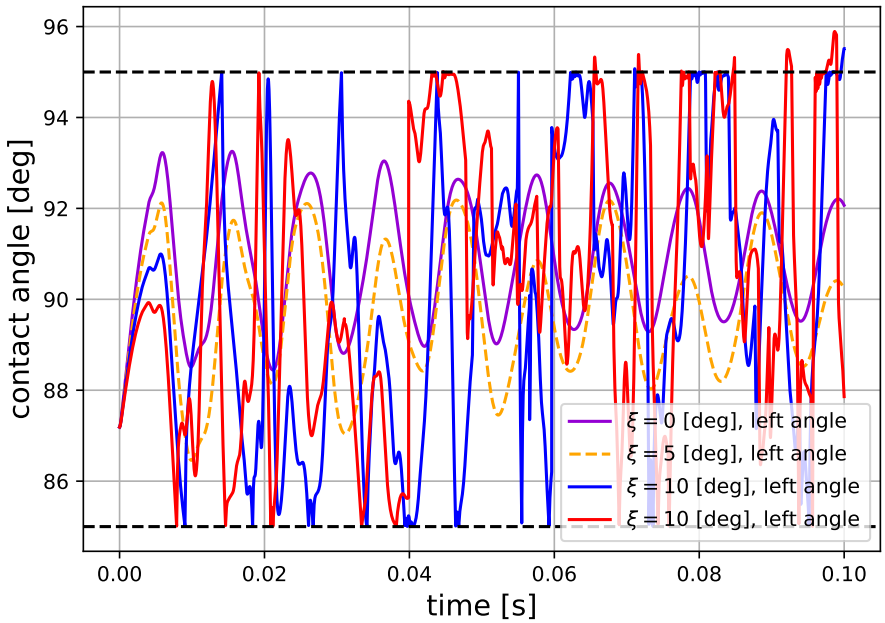

(b) Dynamic contact angle at the left contact line.

Figure IV.9: Evolution of the position and the dynamic contact angle at the left contact line.

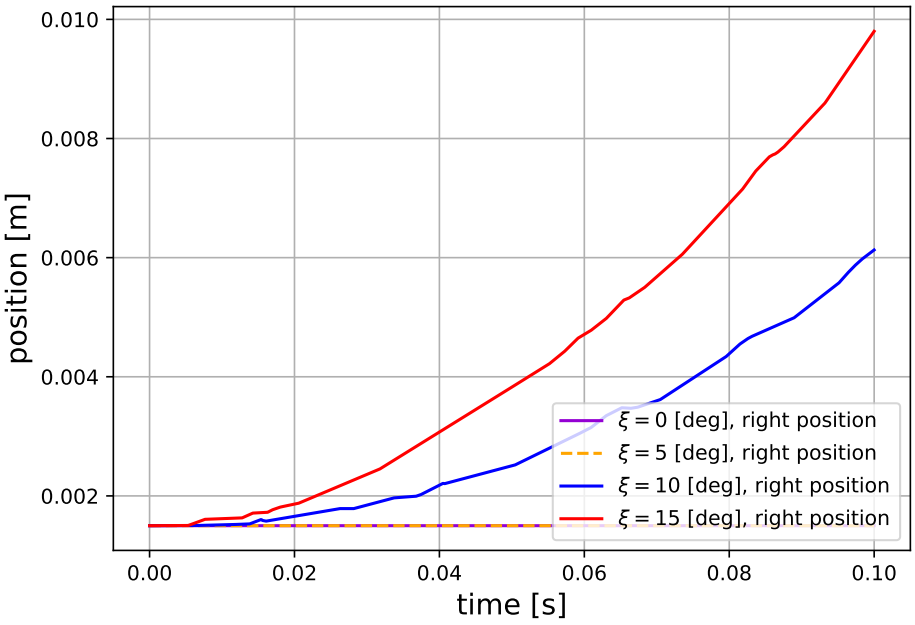

(a) Position of the right contact line.

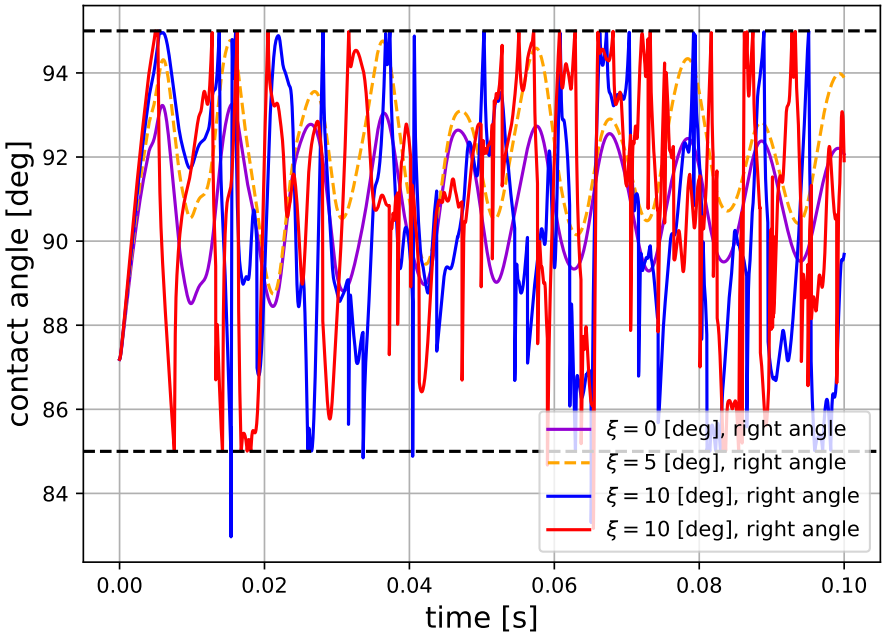

(b) Dynamic contact angle at the right contact line.

Figure IV.10: Evolution of the position and the dynamic contact angle at the right contact line.

The quantities that are measured over time if Figs. IV.9 and IV.10 are the values of the contact line position (resp. on the left side of the droplet and on the right side of the

droplet) and the value of the dynamic contact angle (resp. on the left side of the droplet and on the right side of the droplet). In terms of the evolution of the dynamic contact angle, once the value of either the static advancing angle of that of the receding angle is attained, it starts to oscillate erratically, just as studied for the fine mesh simulations (*cf.* Fig. IV.7). Hence, the unstable behaviour of the contact angle is a problem that is most certainly related to the simplicity of the implemented numerical model.

To obtain somewhat of a physical interpretation of these results, the coordinate of the contact line, both on the left side and on the right side of the droplet, is tracked over time. This position over time is measured as represented in Fig. IV.11.

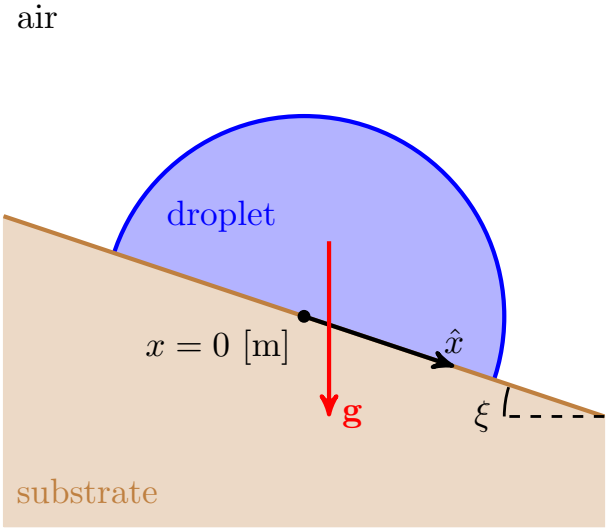

Figure IV.11: Representation of how the position of the contact lines are measured.

As should be expected, the evolution of the contact line coordinate follows a quadratic law because the droplet accelerates from the left side of Fig. IV.11 to the right side under the influence of gravity. While this result does not add much value to the discussion, it is interesting to notice that the unstable behaviour of the dynamic contact angle does not seem to have that much of an impact on the behaviour of the droplet displacement over time. Furthermore, another observation that adds to the qualitative validation of the implemented model for contact angle hysteresis is that when the inclination angle ξ is increased, the contact line starts to move sooner. This is observed when comparing the blue and red curves if Figs. IV.9a and IV.10a, respectively for $\xi = 10$ [deg] and $\xi = 15$ [deg]. These figures also allow to conclude that the threshold value for the droplet to start sliding under the effect of gravity is anywhere in between $\xi = 5$ [deg] and $\xi = 10$ [deg]. In Fig. IV.12, some simulation snapshots of the sliding droplet are presented ($\xi = 15$ [deg]). Note that the inclination does not appear here, because the effect of gravity is taken account of by setting the body force $\mathbf{b}$ to $\mathbf{b} = 9.81(\sin\xi, -\cos\xi)$.

5 Conclusion

In this part of the work, following the theoretical discussion on the phenomenon, a simple model for contact angle hysteresis was suggested. A first case study was suggested and

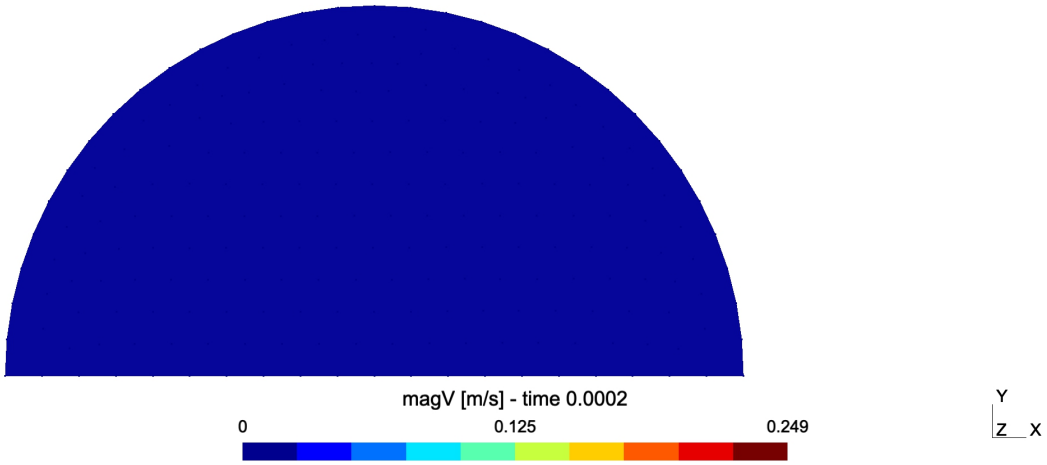

(a) Initial shape of the droplet.

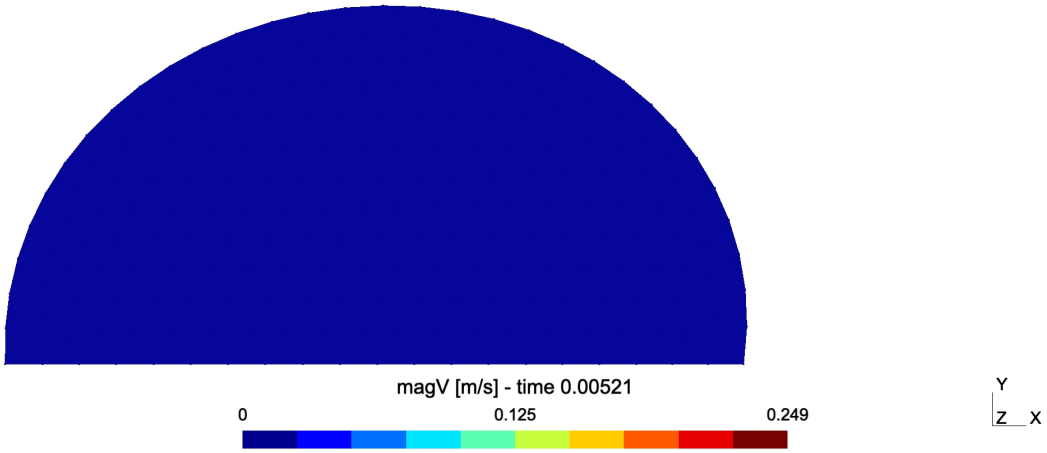

(b) Shape of the droplet the instant before its right contact line is allowed to mode.

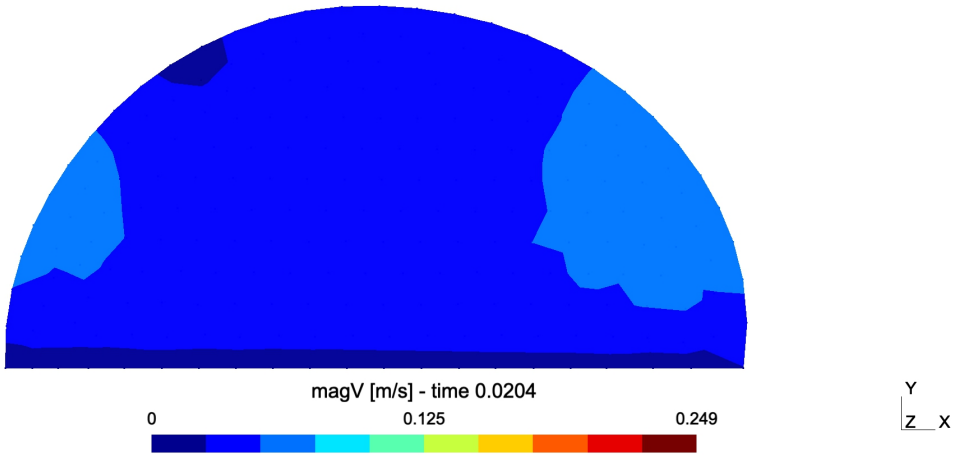

(c) Motion of the droplet on the incline.

Figure IV.12: Some simulation snapshots of the droplet on an incline problem.

pointed out the mesh-dependent nature of the numerical solution. Indeed, the evolution of the dynamic contact angle was pointed out to be very erratic and unstable. However, during the qualitative study that followed, it was pointed out that despite this unstable evolution of the contact angle, this did not seem to impact the physical relevancy of the solution in terms of the motion of the contact line. This has been pointed during the examination of the droplet on a slide case study.

As is pointed out in the theoretical discussion of this part of the work, contact angle hysteresis is a very complex phenomenon, which shows in the obtained numerical results. More search on this topic for further progress of the `PFEM3D` computer code is required. However, a baseline for verification has been qualitatively established here and seems to indicate that, ignoring the questionable behaviour of the dynamic contact angle over time, contact angle hysteresis is accounted for in the computer model.

Part V
Conclusion and prospects for future work

In this work, the PFEM3D computer code has been extended in order to model liquid-substrate contact phenomena at millimeter scales using the particle finite element method. This particular finite element method was deemed particularly useful for problems of such nature, because its inherent Lagrangian nature allows for free surface tracking over time. Concretely, this extension consisted in adding a set of additional forces at the liquid-substrate contact region.

In a first instance, a case study for the PFEM3D computer code without any additional forces has been considered. In this case, the 2D Rayleigh model [6] was used as a reference. The nature of this theory was to model droplet oscillations in zero-gravity, *i.e.*, without the application of body forces, neither considering contact with a substrate. The results obtained by PFEM3D were proven to be in excellent agreement with the theoretical predictions, most notably for the case in which small oscillations of the droplet free surface were considered. The small oscillations hypothesis was imposed by the theoretical model, and not by a limitation of PFEM3D. This case study was introduced as a first application of the PFEM3D computer code to millimeter-scale fluid dynamics, and more specifically to the modelling of the competition between surface tension and viscosity, crucial for small-scale problems.

Then, the work of Mahrous [9] was considered for the implementation of the set of lacking forces. The forces to add to the FE model suggested by [9] were (a) a force resulting from friction at the liquid-substrate contact, (b) a force resulting from the capillary effect at the contact line and (c) a force resulting from the normal stress component at the contact line. Before the implementation of these forces, it was pointed out that the force resulting from surface tension at the contact line was lacking, as well as a horizontal free slip boundary condition. For the implementation of the surface tension force at the contact line, the approach from Jarauta [10] was followed, who suggested in his work an *implicit* expression for this term. The set of lacking forces were then added to the PFEM3D computer code. For the force related to friction at the liquid-substrate contact, the work of Cremonesi [12] was considered for an alternative implementation for the value of the Navier-slip coefficient, while the remaining forces were implemented as prescribed by [9]. Once more, the results from PFEM3D were proven to be in excellent agreement with respect to the work of Mahrous [9], despite the use of different approaches sometimes (namely for the implementation of the contact angle as well as for the determination of the Navier-slip coefficient).

In the final part of this work, with a completed PFEM3D computer code, the problem regarding contact angle hysteresis was tackled. Indeed, it has been pointed out that contact angle hysteresis is a phenomenon that is particularly important for the modelling of small-scale fluid dynamics. The implementation of this phenomenon followed the work

of Jarauta [10], which suggested pinning of the contact line when the dynamic contact angle was within a given interval. Preliminary results computed by the `PFEM3D` computer model were proven to be encouraging, in the sense that they coincide with the prescribed theoretical phenomenology. It is underlined once more however that the evolution of the dynamic contact angle over time seems faulty, but does not lead to nonphysical behaviour of *e.g.* the droplet on a slide problem.

The combination of these results lead to the conclusion that `PFEM3D` is now a computer model, based on the particle finite element method, that could potentially prove useful for the modelling of more complex millimeter-scale fluid dynamics problems, such as lab-on-chips, spoken about in the introduction of this work. However, tackling this range of problems would, in a first instance, require further work on the value of the static contact angle. Indeed, it has been pointed out in this work that for the time being, the value of the equilibrium contact angle could either be imposed to an exact value (in which case no contact angle variations are possible) or to 90 [deg] only (in which case contact angle variation is possible). In addition, further verification of the computer model validity in terms of the representation of contact angle hysteresis should be performed.

Appendices

Appendix 1. (*Proof of approximation* $n\beta_n R_0^{n-2} \simeq \dot{\varepsilon}_n$.) Start from the velocity potential of the n-th mode (Eq. II.12) :

$$\varphi(r,\theta,t) = \beta_n(t) r^n \cos(n\theta), \tag{A.1}$$

as well as the kinematic boundary condition (Eq. II.13) :

$$v_r(r=R) = \left.\frac{\partial \varphi}{\partial r}\right|_{r=R} = \frac{\partial R}{\partial t}. \tag{A.2}$$

Per substitution of Eq. A.1 in Eq. A.2, the following arises :

$$\begin{aligned} v_r(r=R) &= \left.\frac{\partial \varphi}{\partial r}\right|_{r=R} = \frac{\partial}{\partial r}\left[\beta_n(t) r^n \cos(n\theta)\right]_{r=R} \\ &= \beta_n(t) n r^{n-1} \cos(n\theta)\Big|_{r=R} = \frac{\partial R}{\partial t}. \end{aligned} \tag{A.3}$$

In Eq. A.3, R can be substituted by its expression Eq. II.11 to get, for any $n \geq 2$:

$$\begin{aligned} \frac{\partial R}{\partial t} &= \frac{\partial}{\partial t}\left[R_0\left(1 - \frac{1}{4}\varepsilon_n^2 + \varepsilon_n \cos(n\theta)\right)\right] \\ &= R_0\left(-\frac{1}{4}\dot{\varepsilon}_n^2 + \dot{\varepsilon}_n \cos(n\theta)\right) \\ &\simeq R_0 \dot{\varepsilon}_n \cos(n\theta), \end{aligned} \tag{A.4}$$

where the passage from the second to the third line is backed by the fact that $\varepsilon_n = \alpha_n / R_0 \ll$, such that $\dot{\varepsilon}_n^2 \ll \dot{\varepsilon}_n$. Hence, by substitution of Eq. A.4 in Eq. A.3 (note $\beta_n(t) \equiv \beta_n$ to alleviate notations) :

$$\begin{aligned} \beta_n n r^{n-1} \cos(n\theta)\Big|_{r=R} \simeq R_0 \dot{\varepsilon}_n \cos(n\theta) \quad &\Longleftrightarrow \quad \beta_n n R^{n-1} \cos(n\theta) \simeq R_0 \dot{\varepsilon}_n \cos(n\theta) \\ &\Longleftrightarrow \quad \beta_n n R^{n-1} \simeq R_0 \dot{\varepsilon}_n. \end{aligned} \tag{A.5}$$

However, given $\varepsilon_n \ll$ such that $R \simeq R_0$, Eq. A.5 can finally be approximated as :

$$\dot{\varepsilon}_n \simeq n \beta_n R_0^{n-2}, \tag{A.6}$$

which concludes the proof.

Appendix 2. (*Proof that the second integral of the RHS is Eq. II.15 is equal to zero due to incompressibility.*) Recall that the incompressibility condition translates mathematically to :

$$\nabla \cdot \mathbf{v} = 0, \tag{A.7}$$

which can be re-written as follows in terms of the velocity potential φ :

$$\nabla \cdot (\nabla \varphi) = \nabla^2 \varphi = 0. \tag{A.8}$$

Hence, by substitution of Eq. A.8 in Eq. II.15, the proof is immediate :

$$-\int_{\Omega(t)} \frac{1}{2} \rho \varphi \underbrace{\nabla^2 \varphi}_{=0} \, \mathrm{d}\Omega(t) = 0. \tag{A.9}$$

Appendix 3. (*Is simulation quality degraded by setting larger characteristic element sizes in the liquid bulk ?*) To prove the point that the characteristic element size $h(d)$ can be set to larger values in the liquid bulk, it suffices to compare the simulation results with and without local mesh refinement[11] allowed. Hence, for the case in which local mesh refinement is allowed, the characteristic element size is a function of the distance d from the droplet free surface $\partial\Omega(t)$ and is set to the following value :

$$h(d) = 10^{-4} + 0.2 \times d \text{ [m]}, \tag{A.10}$$

which is determined to be the « optimal »[12] value in Section 3.4.1. For the case in which no local mesh refinement is allowed, the value of the characteristic element size is uniform over the entirety of the mesh and set to a value of 10^{-4} [m]. For these cases, the graph displaying the comparison between the resulting curves and the theoretical predictions is given in Fig. A.1.

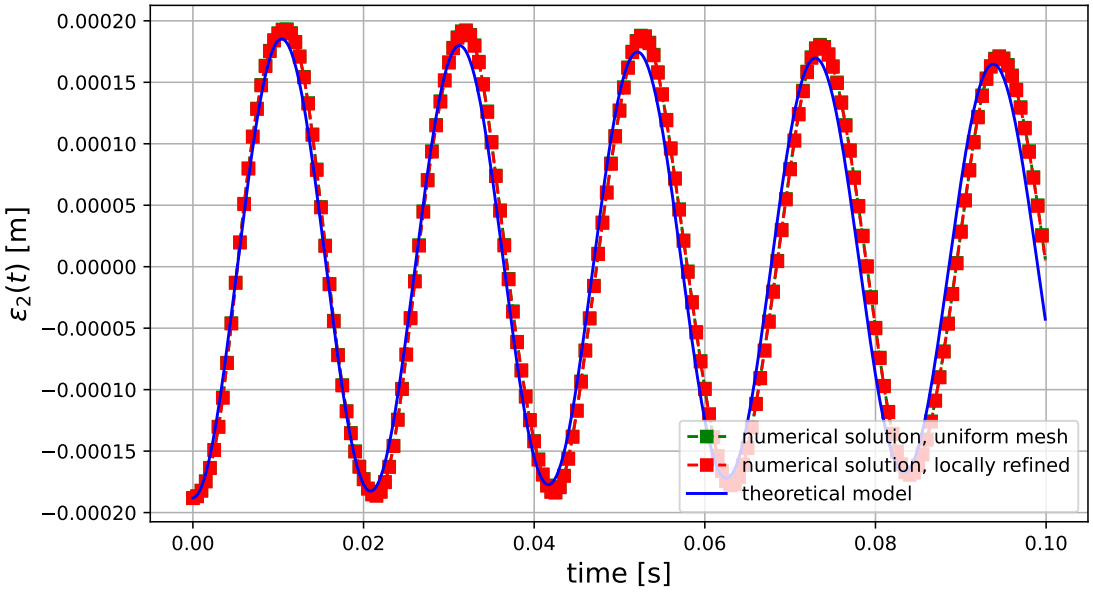

Figure A.1: Comparison between the theoretical model Eq. II.33 and the numerical solution considering the possibility for mesh refinement and no possibility for mesh refinement.

This figure showcases that the numerical results considering local mesh refinement and no local mesh refinement are virtually indistinguishable, meaning they lead to virtually identical results. The reason for preferring the implementation with local mesh refinement is that the latter accomplishes the simulation in considerably less CPU-time. Indeed, the simulation using no local mesh refinement exhibits a CPU-time of $\sim 3,200$ [s], while the one with local mesh refinement only needs ~ 500 [s] to finish the computations.

[11] When speaking about « local mesh refinement » here, it is meant that the mesh is finer along the droplet free surface, while it is coarser in the bulk of the droplet.

[12] The usage of the term « optimal » here means that this value of $h(d)$ maximizes result quality while minimizing CPU-time.

Appendix 4. *(A discussion on performance in terms of mass conservation/element quality.)* As explained in Part I, the main difference between `CGAL` re-meshing and `CGALConstrainedChew` re-meshing is that the former allows for both element addition and suppression, while the latter only allows for element addition. In terms of mass conservation, this might mean that `CGAL` re-meshing performs better in conserving mass over the time of the simulation[13], so why is `CGALConstrainedChew` preferred over it ? The reason for this preference is simply that `CGALConstrainedChew` performs better generally speaking, for example : element suppression at the free surface (of the droplet, in terms of the current framework) is a quite prominent problem with `CGAL` re-meshing, but is minimized with `CGALConstrainedChew` re-meshing. More important even is that the overall mesh quality is optimized, which ultimately allows for better result interpolation and hence better overall result quality. Consider for example the set of figures below, Fig. A.2, which are snapshots from a simulation in which large droplet deformations are modelled[14].

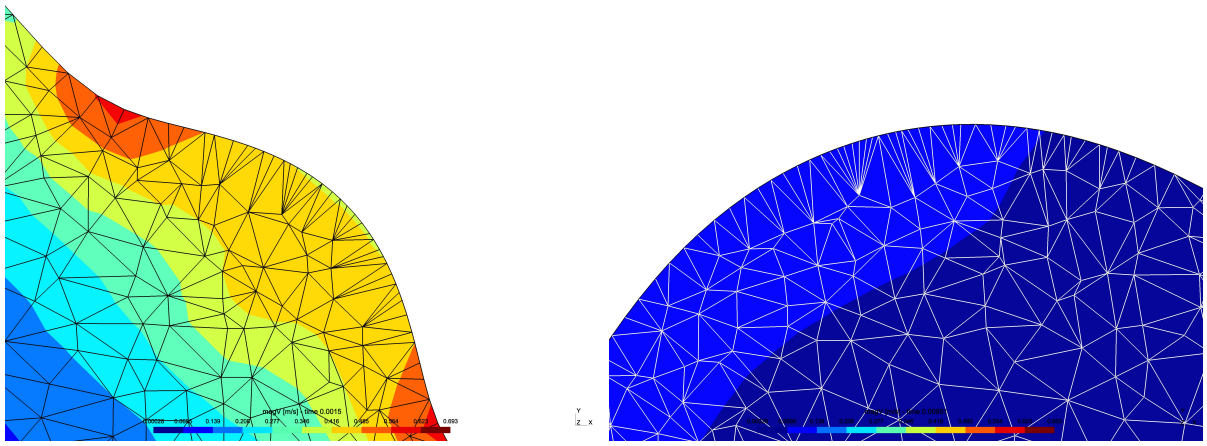

(a) Snapshot one. (b) Snapshot two.

Figure A.2: Snapshots from a simulation rendered in the `Gmsh API` using `CGAL` re-meshing.

The nodes in which numerous elements from the free surface converge are called *thorns*, and lead to poor interpolation quality of the simulation results. Indeed, for numerical solutions in which *e.g.* large velocity gradients appear, the interpolation of the results for each element at one same node might be difficult and lead to poor solution representation. Of course, this problem can be countered by refining the characteristic element size at points where these velocity gradients are large, but this would increase the CPU-time, which is something that the user would rather avoid.

The question on how mass is conserved over time by both re-meshing algorithms still remains, and is a primordial one to be considered, given if droplet mass is not conserved over time, the simulation results, even if mesh quality is optimal, are inherently false. In Fig. A.3, a comparison on mass conservation is performed using both `CGAL` and

[13] As elements that are added/removed can be removed/added by the algorithm to compensate element excess/loss.

[14] More information on the nature of the problem that is modelled, such as geometrical, numerical and physical parameters is omitted here, because it adds nothing interesting to the current topic of discussion.

`CGALConstrainedChew` re-meshing. The full set of parameters is (*cf.* Section 4)[15] :

- Geometry parameters (initial droplet configuration : ellipse) :
  - Major axis $a = 1.75$ [mm], minor axis $b = 1.629$ [mm] ;
  - Equilibrium geometry/configuration : equilibrium radius $R_0 = 1.688$ [mm] ;
- Numerical parameters :
  - Characteristic element size $h(d) = 10^{-4} + 0.2 \times d$ [m] ;
  - Time-step $\Delta t = 10^{-5}$ [s] ;
  - Simulation time $\mathcal{T} = 0.1$ [s] ;
  - Alpha-parameter $\alpha = 1.2$ [-] ;
  - `CGAL/CGALConstrainedChew` re-meshing.

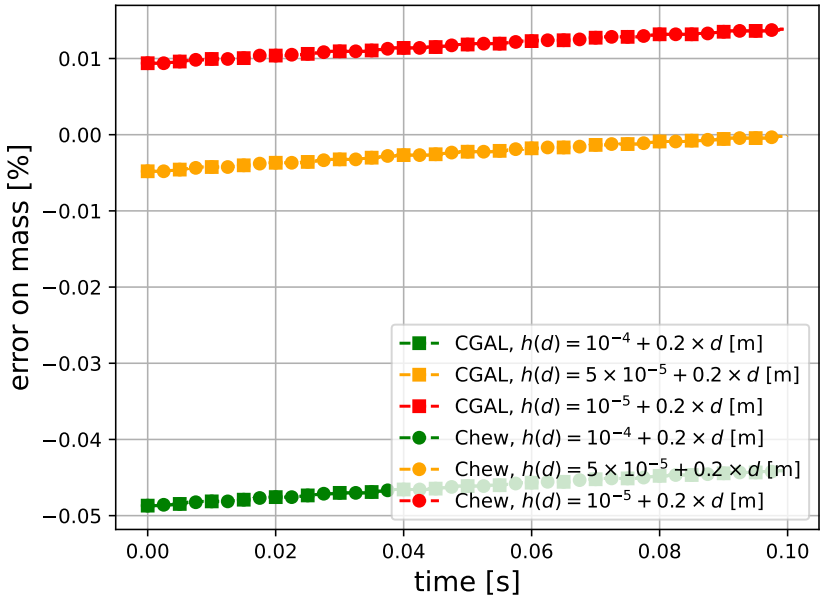

Figure A.3: Comparison of the error on mass using both `CGAL` and `CGALConstrainedChew` re-meshing for the case study presented in Section 4.

The error on mass appearing in this figure is defined along :

$$\text{error on mass} \equiv \Delta_m = \frac{m^{\text{theoretical}} - m^{\text{numerical}}}{m^{\text{theoretical}}} \times 100, \tag{A.11}$$

and expressed in [%]. From the figure above, it turns out the error on mass committed by the `CGAL` re-meshing algorithm and the `CGALConstrainedChew` re-meshing algorithm is the same over time, leading to the conclusion that the latter is a preferable choice. Furthermore, this error is of the order of 10^{-2} [%], meaning that mass is almost perfectly conserved during the simulation.

[15] This set of parameters is used because later in this work it will be proven that these lead to numerical convergence for the case study presented in Section 4.

Appendix 5. *(Some simulation snapshots and supplementary remarks.)* For the case study in which the initial deviation from equilibrium is large, it is interesting to display some simulation snapshots on the oscillation pattern of the droplet free surface $\partial\Omega(t)$. These snapshots are presented in Fig. A.4 for different values of the simulation time and obtained using the set of parameters described in Section 5.

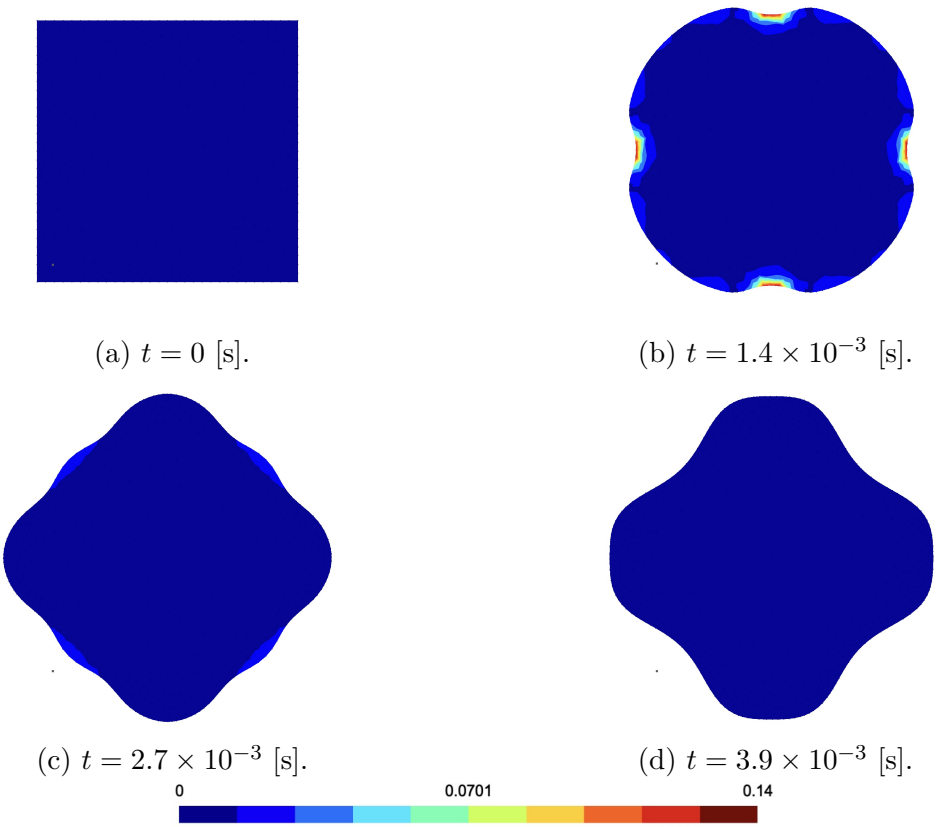

(a) $t = 0$ [s]. (b) $t = 1.4 \times 10^{-3}$ [s].

(c) $t = 2.7 \times 10^{-3}$ [s]. (d) $t = 3.9 \times 10^{-3}$ [s].

Figure A.4: Snapshots from the simulation case described in Section 5 rendered in the `Gmsh API` at different times t. The color profile represents the droplet kinetic energy k_e.

These figures show the apparition of so-called *standing capillary waves*, which manifest because of the large initial deviation from equilibrium. Indeed, these result from the large pressure gradient that is initially imposed by the definition of the reference configuration geometry. Mathematically speaking, standing capillary waves represent the oscillation mode $n = 4$ described in Section 5. The graph for the numerical solution Fig. II.13 also shows these standing capillary waves ; this is presented in Fig. A.5. The way these standing capillary waves appear in the graph for $\varepsilon_2(t)$ over time is by the addition of an oscillation mode, and more precisely by the increasing/damping of the elementary oscillation mode $n = 2$ (clearly visible near the maxima/minima of the curve in Fig. A.5). Over time, these standing capillary waves fade out and the oscillation pattern reaches that of a case in which a small initial deviation from equilibrium is imposed (due to viscous energy dissipation).

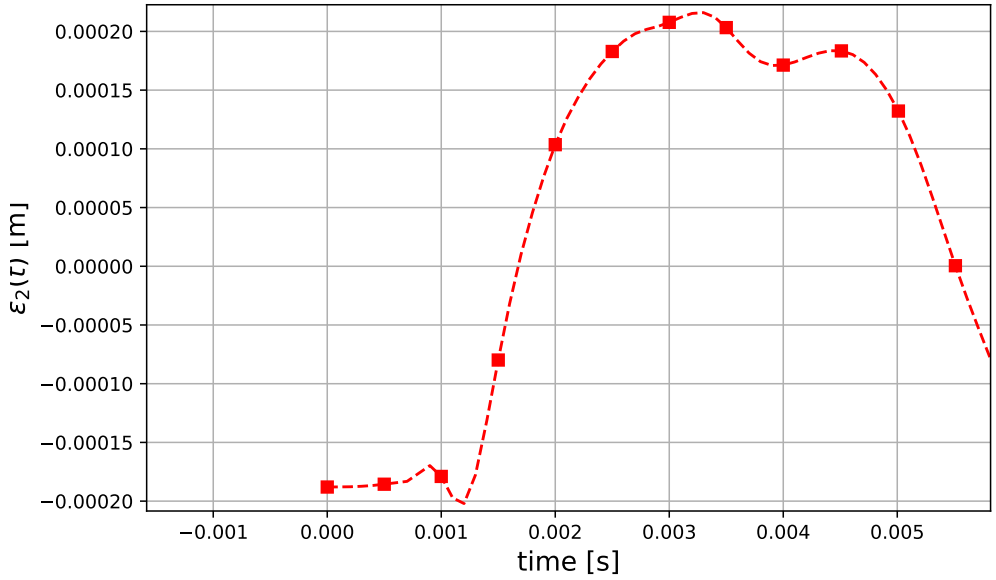

Figure A.5: Evolution of the droplet free surface over time for a large initial deviation from equilibrium (*cf.* Section 5).

References

[1] A. Pradeep, J. Raveendran, T.G. S. Babu, *Chapter Five - Design, fabrication and assembly of lab-on-a-chip and its uses*, Progress in Molecular Biology and Translational Science, Academic Press, Volume 187, Issue 1, 2022, Pages 121-162, ISSN 1877-1173, ISBN 9780323853033 (https://doi.org/10.1016/bs.pmbts.2021.07.021).

[2] T. Gilet, *Microfluidics (MECA0008-1)*, course notes, University of Liège, Chapter 0, Spring 2022.

[3] Precedence research, *Lab-on-chip market size, share, and trends 2024 to 2034* (https://www.precedenceresearch.com/lab-on-chip-market#:~:text=The%20global%20lab%20on%20chip%20market%20size%20was%20reached%20at,US%24%2017.42%20billion%20by%202032., consulted August 19th, last updated October 2023).

[4] S. Février, *Development of a 3D compressible flow solver for PFEM fluid simulations*, master thesis, academic year 2019-2020.

[5] M. Cremonesi, A. Franci, S. Idelsohn, E. Oñate, *A state of tthe art review of the particle finite element method (PFEM)*, Archives of computational methods in engineering, 2020, 27 : 1709 - 1735 (https://doi.org/10.1007/s11831-020-09468-4).

[6] A. Aalilija, Ch.-A. Gandin, E. Hachem, *On the analytical and numerical simulation of an oscillating drop in zero-gravity*, Computers & Fluids, Volume 197, 2020, 104362, ISSN 0045-7930 (https://www.sciencedirect.com/science/article/pii/S0045793019303214).

[7] H. Lamb (1881), *On the oscillations of a viscous spheroid*, Proceedings of the London Mathematical Society, s1-13 : 51-70 (https://doi.org/10.1112/plms/s1-13.1.51).

[8] A. Prosperetti, *Viscous effects on perturbed spherical flows*, Quarterly of Applied Mathematics 34, no. 4 (1977) : 339–52 (http://www.jstor.org/stable/43636836).

[9] E. Mahrous, A. Jarauta, T. Chan, P. Ryzhakov, A. Z. Weber, R. V. Roy, M. Secanell, *A particle finite element-based model for droplet spreading analysis*, Physics of Fluids 1 April 2020 : 32 (4) 042106 (https://doi.org/10.1063/5.0006033).

[10] A. Jarauta, P. Ryzhakov, J. Pons-Prats, M. Secanell, *An implicit surface tension model for the analysis of droplet dynamics*, Journal of Computational Physics, Volume 374, 2018, pages 1196-1218, ISSN 0021-9991 (https://doi.org/10.1016/j.jcp.2018.08.001).

[11] S. Meduri, *A fully explicit Lagrangian finite element method for highly non-linear fluid-structure interaction problems*, PhD Thesis, 2019, Politecnico di Milano.

[12] Cremonesi, Massimiliano & Ferri, Francesco & Perego, Umberto, *A basal slip model for Lagrangian finite element simulations of 3D landslides*, International Journal for Numerical and Analytical Methods in Geomechanics, 2016, 41. 10.1002/nag.2544.

[13] J. Venkatesan and S. Ganesan, *On the Navier slip boundary condition for computations of impinging droplets*, 2015 IEEE 22nd International Conference on High Performance Computing Workshops (IEEE, 2015), pp.2–11.

[14] T.-S. Jiang, O. Soo-Gun, and J. C. Slattery, *Correlation for dynamic contact angle*, Journal of Colloid and Interface Science 69, 74–77 (1979).

[15] PORBITAL, *PlotDigitizer*, `https://plotdigitizer.com`.

[16] H.-J. Butt, J. Liu, K. Koynov, B. Straub, C. Hinduja, I. Roismann, R. Berger, X. Li, D. Vollmer, W Steffen, M Kappl, *Contact angle hysteresis*, Current Opinion in Colloid & Interface Science, Volume 59, 2022, 101574, ISSN 1359-0294 (`https://doi.org/10.1016/j.cocis.2022.101574`).